UNIVERSITA' VITA-SALUTE SAN RAFFAELE

CORSO DI DOTTORATO DI RICERCA INTERNAZIONALE IN MEDICINA MOLECOLARE

CURRICULUM IN NEUROSCIENZE E NEUROLOGIA SPERIMENTALE

Identification and validation of novel measurable outcomes for Rett syndrome through MRI and preclinical studies

DoS: Prof.ssa Nicoletta Landsberger

Second Supervisor: Prof. Jean-Christophe Roux

Tesi di DOTTORATO di RICERCA di Sara Carli

matr. 014324

Ciclo di dottorato XXXIV

Area05 BIO/11

Anno Accademico 2020/2021

CONSULTAZIONE TESI DI DOTTORATO DI RICERCA

Il/la sottoscritto/*I*	SARA CARLI
Matricola / *registration number*	014324
nata a/ *born at*	PORTOMAGGIORE
il/*on*	09/09/1991

autore della tesi di Dottorato di ricerca dal titolo / *author of the PhD Thesis titled*

Identification and validation of novel measurable outcomes for Rett syndrome through MRI and preclinical studies

□ AUTORIZZA la Consultazione della tesi / AUTHORIZES *the public release of the thesis*

X NON AUTORIZZA la Consultazione della tesi per 6 mesi /DOES NOT AUTHORIZE *the public release of the thesis for …… months*

a partire dalla data di conseguimento del titolo e precisamente */ from the PhD thesis date, specifically*

Dal / *from* ……/……/…… Al / *to* ……/……/……

Poiché /*because*:

□ l'intera ricerca o parti di essa sono potenzialmente soggette a brevettabilità/ *The whole project or part of it might be subject to patentability;*

X ci sono parti di tesi che sono già state sottoposte a un editore o sono in attesa di pubblicazione/ *Parts of the thesis have been or are being submitted to a publisher or are in press;*

□ la tesi è finanziata da enti esterni che vantano dei diritti su di esse e sulla loro pubblicazione/ *the thesis project is financed by external bodies that have rights over it and on its publication.*

Data /Date 26/02/2022 Firma /Signature

DECLARATION

This thesis has been composed by myself and has not been used in any previous application for a degree. Throughout the text I use both 'I' and 'We' interchangeably.

All the results presented here were obtained by myself, except for:

1) ***High Resolution Respirometry assay***, *which was performed in collaboration with Dr. Clara De Palma, Dept of Medical Biotechnology and Translational Medicine (BioMeTra), University of Milan, Milan, Italy.*

2) ***Magnetic Resonance Imaging***, *which was technically carried out by Dr. Linda Chaabane, Institute of Experimental Neurology (INSPE) and Experimental Imaging Center (CIS), IRCCS San Raffaele Scientific Institute, Milan, Italy and analysed by myself.*

Part of the present work (chapters *6.1.1, 6.1.2, 6.1.3, 6.2.1, 7.1* and related Material and Methods) was performed and been published by Sara Carli (Carli *et al*, 2021) in partial fulfillment of the requirements for obtaining the PhD degree at Vita-Salute San Raffaele University, Milano, Italy.

All sources of information are acknowledged by means of reference

Abstract

Mutations in the X-linked *Mecp2* gene are responsible for the typical form of Rett syndrome (RTT), a devastating neurodevelopmental disorder that affects almost 1 out of 10,000 females born alive. Although mutations in the *Cdkl5* gene have initially been associated with an atypical form of RTT, *Cdkl5* Deficiency Disorder is now an independent disease (CDD). Nonetheless, both pathologies share a plethora of symptoms and they are primarily identified by neurodevelopmental delay. To date, no effective cure is available for RTT and CDD, even though it was demonstrated that reactivation of gene-causing disease in animal models leads to the reversal of neurological symptoms. Both diseases lack solid biomarkers capable of quantitatively measuring structural, functional or metabolic changes, permitting the assessment of disease progression and the actual benefits of therapeutic approaches. To fulfil this gap of knowledge, my thesis principally aimed at identifying sensitive measurable outcomes for both diseases. We exploited multiple approaches of *ex vivo* and *in vivo* Magnetic Resonance Imaging (MRI) to investigate anatomical and neurochemical properties of different cerebral regions in preclinical models of RTT and CDD. No difference in brain morphology was found in the *Cdkl5* KO mouse, whereas a strong deregulation of metabolites related to mitochondrial homeostasis led us to unveil altered ATP and activated AMP-protein kinase (AMPK) levels. To validate those results, we started a pharmacological treatment acting on AMPK, that significantly ameliorated behavioural phenotypes of the *Cdkl5* mouse. On the other hand, we longitudinally compared a full *Mecp2* knockout mouse to a knock-in mouse harbouring a pathogenic missense mutation (*Mecp2*-Y120D). *In vivo* MRI on both genders revealed how developmental trajectory of the brain evolves in a comparable but not overlapping way, thus highlighting relevant gender and genotype discrepancies. Concomitantly, magnetic spectroscopy unveiled dysregulation of metabolites mainly related to energy homeostasis and neurotransmission. Collectively, we revealed the great potential of MRI in monitoring the disease progression in specific models of RTT and CDD and in identifying relevant pathways to pursue ad hoc pharmacological approaches. Further, they have highlighted that *Mecp2* deficiency diversely affect the disease progression depending on the genetic lesion, gender and region of the brain.

1. Table of contents

2. Acronyms and Abbreviations

5hmC: 5-hydroxymethylcytosine

AMPK: AMP-activated Protein Kinase

ASD: Autism Spectrum Disorder

BDNF: Brain-Derived Neurotrophic Factor

CDD: *Cdkl5* Deficiency Disorder

CDKL5: Cyclin-Dependent Kinase-Like 5

Cr: Creatine

CREB1: Cyclic AMP-responsive Element-Binding Protein 1

CTD: C-terminal domain

CVI: Cortical Visual Impairment

DNMT1: DNA Methyl Transferase 1

DTI: Diffusion Tensor Imaging

E/I: Excitation/Inhibition

EEG: Encephalogram

EP: Entorhinal-perirhinal cortex

EPs: Evoked Potentials

ETC: Electron Transport Chain

fMRI: Functional MRI

FOXG1: Forkhead Box G1

Glu: Glutamate

Gln: Glutamine

GPC: Glycerophosphocholine

GSK3β: Glycogen Synthase Kinase 3β

Fis1: Mitochondrial Fission Protein 1

H: Hippocampus;

H^1-MRS: Proton Magnetic Resonance Spectroscopy

HDAC4: Histone Deacetylase 4

HET: Heterozygous

HET-KI: Heterozygous females from the Y120D line

HRR: High Resolution Respirometer

ID: Intervening Domain

KI: Knockin

KO: Knockout

Lac: Lactate

MBD: Methyl DNA Binding Domain

MECP2: Methyl-CpG Binding Protein 2

MEMRI: Manganese Enhanced Magnetic Resonance Imaging

$MnCl_2$: Manganese Cloride

MRI: Magnetic Resonance Imaging

NAA: N-acetyl-aspartate;

NAAG: N-acetyl-aspartyl-glutamate.

NES: Nuclear Export Signal

NLS: Nuclear Localization Signal

NOR: Novel Object Recognition

NTD: N-terminal Domain

Opt: Optic tract

OPA1: Optic Atrophy gene 1

OXPHOS: Oxidative Phosphorylation

PCh: Phosphocholine

PCr: Phosphocreatine

PF: Parafascicular nucleus of the thalamus

PFA: Paraformaldehyde

PGC-1α: Peroxisome Proliferator-activated Receptor-γ Coactivator-1α

PLS-DA: Partial Least Squares Discriminant Analysis

PTMs: Post-Translation Modifications

RTT: Rett syndrome

SC: Superior colliculus

SNR: Signal-to-Noise Ratio

SS: Somatosensory cortex

STK9: Serine Threonine Kinase 9

TRD: Transcriptional Repression Domain

VC: Visual cortex

VIP: Variable's Importance in the Projection

VEP: Visual Evoked Potential

VP: Ventral posterior nucleus of the thalamus

WT: Wild-type

XCI: X-Chromosome Inactivation

3. List of Figure and Tables

4. Introduction

4.1 Rett syndrome and *CDKL5* Deficiency Disorder

Rett syndrome (RTT, OMIM #312750) is a devastating X-linked neurodevelopmental disorder that affects roughly 1 in 10,000 live female births. RTT was originally defined in 1966 by Andreas Rett, but it was internationally recognized only twenty-years later, when 35 cases of RTT were described in English language (Hagberg *et al*, 1983).

RTT patients appear to develop normally and to achieve common neurodevelopmental milestones up to 6 to 18 months of age; afterward, they gradually manifest a regression phase followed by the onset of several symptoms such as hand stereotypies, intellectual disability, respiratory abnormalities and spontaneous seizures.

To address some of the confusion due to the constellation of clinical and molecular information regarding the diagnosis of RTT, in 2010 Neul and colleagues refined the diagnostic criteria, stating the presence of a period of regression as the essential condition. In addition, patients must exhibit the loss of acquired purposeful hand skills and spoken language, gait abnormalities and hand stereotypies. The post-natal deceleration in head growth was eliminated from necessary criteria, since it is not a consistent feature in all individuals affected by RTT (Neul *et al*, 2010).

RTT girls also manifest autistic characteristics comprising lack of eye-to-eye contact, expressionless face, sound hypersensitivity, unresponsiveness to the environment and insensitivity to social cues. Also, they develop severe motor impairment, including ataxia and gait apraxia (Nomura, 2005).

Supportive diagnostic criteria include autonomic dysfunction. Hyperventilation during wakefulness was described as the initial autonomic perturbation, however breathing anomalies comprising breath-holding, apnea, aerophagia, forced expulsion of air and saliva are common. Literature also reports EEG abnormalities, gastrointestinal disorders, peripheral vasomotor disturbance, spasticity, scoliosis and growth retardation (Neul, 2010). Eventually, one of the most arduous symptoms is epilepsy, which ranges from easily controlled to intractable seizures (Jian *et al*, 2006).

Of relevance, there are still poor longevity studies, mostly because several RTT patients currently live into middle age (Percy & Lane, 2005)(Figure 1). However, it was observed that many patients survive until 60 or 70 years of life with reduced mobility. Nevertheless, a higher occurrence rate of unexpected death is reported, probably connected to autonomic dysfunctions such as the augmented rate of long Q-T intervals (Hagberg, 2005; Weng *et al*, 2011).

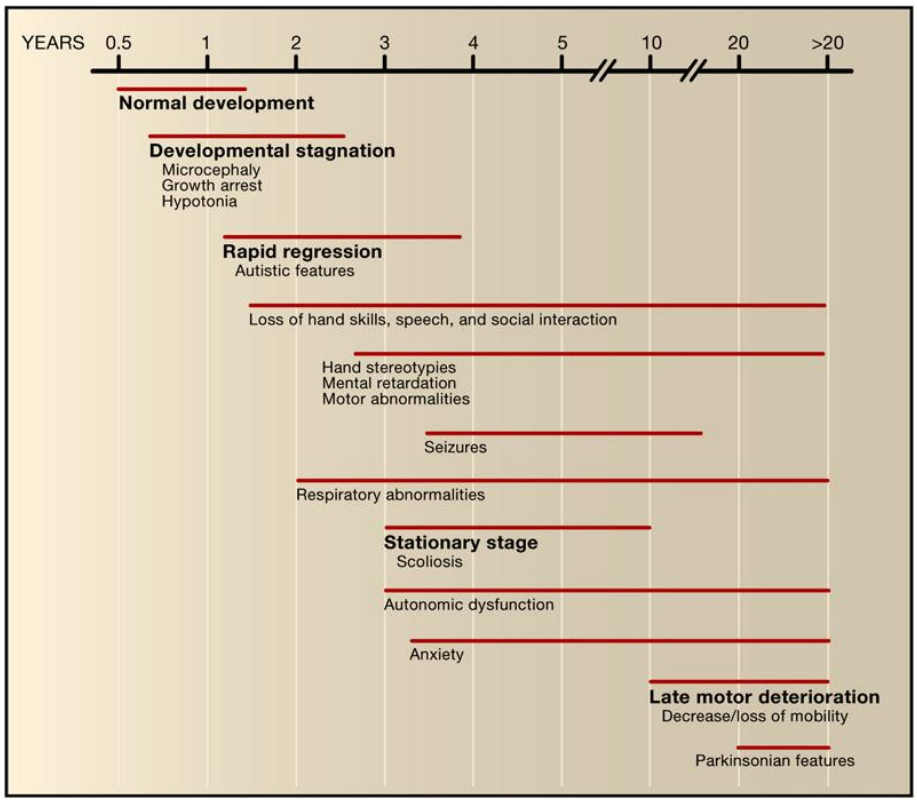

Figure 1. **Onset and development of clinical symptoms in Rett patients.** RTT girls show an apparent normal development, followed by developmental stagnation and a consequent rapid regression phase in which patients experience loss of acquired speech, hand purposeful use and social interaction. After a period of stationary stagnation, in which autonomic dysfunctions occur, the clinical condition worsens with a profound deterioration of motor ability (Chahrour & Zoghbi, 2007)(Open Access).

Using a systematic gene screening approach, in 1999 Amir and colleagues recognized mutations in the X-linked Methyl-CpG-binding protein 2 (*MECP2*) gene, that encodes for the methyl-CpG-binding protein 2 (MeCP2), as the cause of the majority of Rett syndrome cases. Mutations in *MECP2* account for 90–95% of "typical" RTT. A fundamental trait in the etiology of the disease is that *MECP2* is sited on the X chromosome, precisely in the Xq28 locus (Amir *et al*, 1999). Accordingly, in hemizygous

males, the complete lack of functional MeCP2 generally leads to encephalopathy and death within the first years of life (Schüle *et al*, 2008). In contrast, in heterozygous females, because of a generally random X chromosome inactivation, roughly 50% of the cells expresses the mutant *MECP2* allele while the remaining half expresses the functional one, therefore leading to RTT. However, few female patients, that feature a skewed X chromosome inactivation favouring the expression of the wild type allele, can be slightly affected or even asymptomatic carriers of *MECP2* mutations (Chahrour & Zoghbi, 2007).

It is important to point out that some patients do not perfectly match all the necessary criteria of the typical disorder. Accordingly, "variant" or "atypical" forms of RTT have also been characterized. Atypical RTT can be clustered in divergent clinical groups such as preserved speech variant, early seizure variant and congenital variant (Hagberg & Skjeldal, 1994; Hagberg, 1995). The preserved speech variant, also known as Zappella variant, is the milder form of Rett syndrome and patients generally harbouring either missense mutations (primarily the R133C mutation) or late truncating ones (mostly C-terminal deletions of 17–44 bp) in the *MECP2* gene (Renieri *et al*, 2009). The congenital variant is often caused by mutations in the Forkhead Box G1 (*FOXG1*) gene, that encodes for a brain-specific transcriptional repressor crucial for early development of the telencephalon (Ariani *et al*, 2008). Eventually, the early seizure variant has been linked to mutations in the X-linked gene Cyclin-dependent kinase-like 5 (*CDKL5*) and leads to early refractory epilepsy (Scala *et al*, 2005; Goutieres & Aicardi, 1986; Olson *et al*, 2019).

Nonetheless, in 2013 Fehr and colleagues defined the CDKL5 Deficiency Disorder (CDD) as an independent entity that should not be considered part of the RTT spectrum. In fact, it was shown that 25% of the reported patients do not overlap with clinical criteria of RTT (Fehr *et al*, 2013). CDD has an approximated incidence between 1 in 40.000 to 60.000 live births. It is principally characterized by an early drug resistant epilepsy beginning in the first months of life. Patients typically experience several seizure types such as epileptic spasms, tonic seizures, and generalized tonic-clonic seizures. As alluded, CDD epilepsy is severe and refractory. Indeed, even when treated with antiepileptic drugs, the seizure-free period ("free honeymoon period") that often follows a new treatment usually results in relapses in *CDKL5* patients. Unfortunately, despite the

brutality of the seizures, the interictal EEG pattern of CDD patients appears normal in infancy, hampering to identify any specific seizure semiology (Fehr *et al*, 2013; Bahi-Buisson *et al*, 2008; Melani *et al*, 2011).

Of note, the regression phase is less common in CDD with respect to RTT (Fehr *et al*, 2013). Furthermore, CDD patients manifest only occasionally autonomic symptoms such as breathing irregularities, GI disturbances and cold extremities (Neul *et al*, 2010). On the contrary, overlapping features include a severe developmental delay and intellectual disability, hypotonia and visual defects, with most of the patients remaining unable to achieve independent walking or speech (Fehr *et al*, 2013, 2016; Olson *et al*, 2015; Artuso *et al*, 2010; Stalpers *et al*, 2012; Bahi-Buisson *et al*, 2008)(Figure 2).

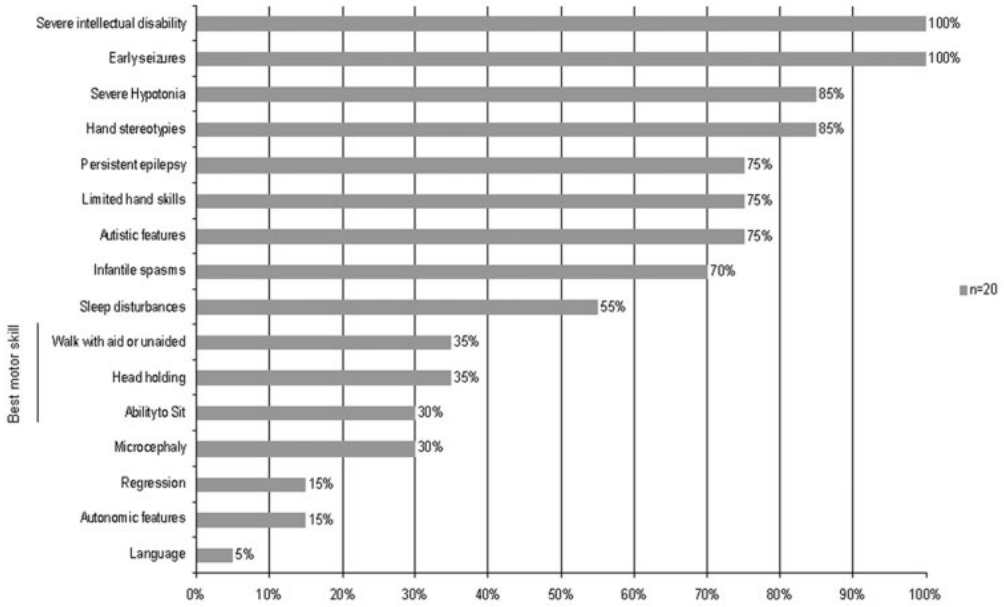

Figure 2: **Clinical features of *CDKL5* Deficiency Disorder.** Principal clinical features observed in 20 *CDKL5* patients. All patients experienced early seizures and severe intellectual disability (Bahi-Buisson *et al*, 2008)(Open Access).

Diversely to RTT, in which *MECP2* mutations are infrequently found in males, a comprehensive analysis in patients with epileptic encephalopathy reported that *CDKL5* mutations has an estimated incidence of female to male ratio of 4:1 (Liang *et al*, 2011; Kilstrup-Nielsen *et al*, 2012; Chahrour & Zoghbi, 2007). However, although *CDKL5* loss was reported to be not lethal in males (Castrén *et al*, 2011), different studies stated that male patients present a more severe clinical picture than females (Elia *et al*, 2008; Lilles *et al*, 2016). In detail, males carrying a *CDKL5* mutation manifest intractable and more

frequent seizures together with severe-to-profound mental and motor retardations, whereas females reach motor milestones that allow them to sit or stand (Liang *et al*, 2019).

4.2 MeCP2 and CDKL5

4.2.1 MeCP2: gene and protein

Well before the discovery of *MECP2* involvement in Rett syndrome, Lewis and colleagues purified and described the protein as a nuclear factor able to bind, through its methyl-CpG-binding domain (MBD), DNA sequences containing at least one symmetrically methylated cytosine in the dinucleotide 5'CpG (Lewis *et al*, 1992). Consistently, in mouse cells the protein accumulates at the highly methylated pericentromeric heterochromatin (Lewis *et al*, 1992; Nan *et al*, 1993).

The gene encompasses four exons which are alternatively spliced, giving rise to two different isoforms that share most of the protein domains but diverge in the N-terminal region (Figure 3). MeCP2-e1 is the longer isoform, containing 21 N-terminal residues (498 amino acids) and its translation initiates in exon 1; instead, MeCP2-e2, that is ten times less abundant than the e1 in the postnatal brain, is slightly shorter (486 amino acids) and it is produced from translation initiation at exon 2. It is still controversial if the two isoforms are functionally equivalent (Itoh *et al*, 2012; Mnatzakanian *et al*, 2004; Kriaucionis & Bird, 2004). Indeed, a very recent report describes some dissimilarities, as lower DNA-binding affinity for the e1 isoform with respect to the e2; on the other hand, ChIP-Seq analysis revealed a major involvement of MeCP2-e2 in the control of ribosomal gene transcription (Martínez De Paz *et al*, 2019).

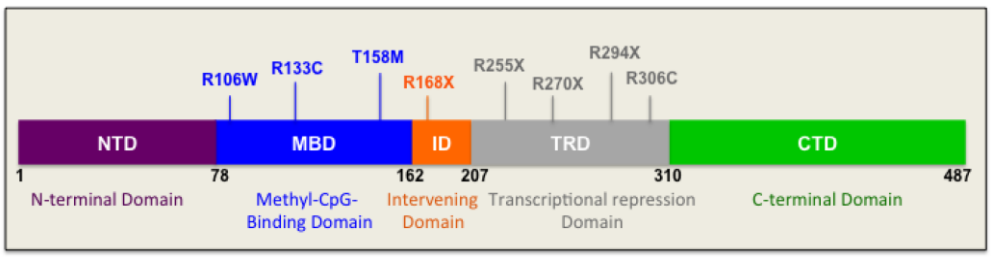

Figure 3: **MeCP2 protein structure**: MeCP2 consists of five domains: the N-terminal domain (NTD), the methyl-CpG binding domain (MBD), the intervening domain (ID), the transcriptional repression domain (TRD) and the C-terminal domain (Pejhan & Rastegar, 2021)(Open Access).

MeCP2 is ubiquitously expressed in mammals, reaching maximal amounts in the brain. Here, the protein levels are seven times higher in neurons with respect to glia, emphasising its relevance for neuronal function (Meehan *et al*, 1989; Shahbazian *et al*, 2002). However, increasing evidence highlight that also glial cells (i.e., astrocytes, oligodendrocytes and microglia) have a role in the pathogenesis of RTT (Ballas *et al*, 2009; Maezawa & Jin, 2010; Okabe *et al*, 2012; Nguyen *et al*, 2013). Indeed, it has been proved that *Mecp2*-null microglia and astrocytes affect the physiological maturation and the well-being of WT neurons, probably through different non-cell autonomous mechanisms, including an abnormal glutamate clearance and impaired levels of glutaminase and connexin 32 (Okabe *et al*, 2012; Maezawa & Jin, 2010; Maezawa *et al*, 2009).

In mice, Mecp2 levels in neurons are relatively low at birth, raise throughout developmental phases and reach a plateau during adulthood (Kishi & Macklis, 2004; Skene *et al*, 2010). It is well established that the ablation of *Mecp2* in different periods of the mouse life, from the perinatal period to adulthood, results in defective neuronal functions mirroring those exhibited by the *Mecp2* full knockout mouse (Gemelli *et al*, 2006; Fyffe *et al*, 2008; McGraw *et al*, 2011; Cheval *et al*, 2012; Nguyen *et al*, 2012). Furthermore, the pivotal function of Mecp2 during cerebral cortex maturation is acknowledged (Picker *et al*, 2006; Santos *et al*, 2007; Chao *et al*, 2007); accordingly, our group demonstrated its importance also during embryonic development. In fact, by using an overall gene expression analysis in the embryonic neocortex, we revealed a dysregulation of numerous molecular pathways that probably impact on *Mecp2* null cortex maturation; neuronal dysfunctions persist at early post-natal ages, therefore well before the onset of RTT symptoms (Bedogni *et al*, 2016). All in all, these data indicate that MeCP2 functions are continuously required for proper brain functions, starting from early development up to adulthood.

4.2.2 MECP2: a multi-talented protein

Despite over 20 years of investigations into the molecular mechanisms of MeCP2, its full activities have still to be unravelled. MeCP2 belongs to a family of heterogeneous

methyl binding proteins and it is organized into five main domains (Figure 3). Among these, the methyl DNA binding domain (MBD; residues 78–163) is necessary to selectively recognize methylated DNA (Nan *et al*, 1993); its importance is suggested by the evidence that most cases of RTT causing missense mutations occur in the MBD as indicated in Figure 4. Another relevant domain is the transcriptional repression domain (TRD) that silences gene transcription mainly through the interaction with co-repressor complexes, such as NCoR and mSin3A, containing histone deacetylase activities (Nan *et al*, 1997; Kruusvee *et al*, 2017; Kokura *et al*, 2001; Stancheva *et al*, 2003). Recently, Lyst and colleagues have mapped within the TRD the NCoR/SMRT interaction domain (NID), highlighting the critical role of NID-mediated interactions in MeCP2 functions. In fact, a single amino-acid change in this domain (i.e. R306C mutation) might contribute to RTT phenotypes (Lyst *et al*, 2013).

Other principal domains of MeCP2 are the N-terminal domain (NTD), the intervening domain (ID), and the C-terminal domain alpha and beta (CTD-α and CTD-β). The main function attributed to the CTD so far is its capacity to mediate the interaction with proteins implicated in the regulation of chromatin structure. Furthermore, MeCP2 contains a nuclear localization signal (NLS), that is highly conserved and relevant for its nuclear localization (Nan *et al*, 1996). Nonetheless, by using different MeCP2 derivatives lacking either the MBD or the NLS (or both), Lyst and colleagues have recently demonstrated that an intact MBD is sufficient for MeCP2 nuclear localization (Lyst *et al*, 2018).

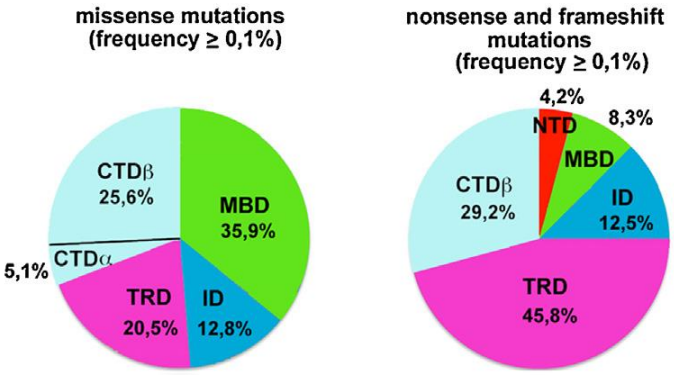

Figure 4: Rate of recurrence of different Rett-causing mutations. The frequency of missense mutations is indicated on the left, while that of truncating mutations is illustrated on the right (Bedogni *et al*, 2014)(License number 5222490663051).

Intriguingly, it has been disclosed that MeCP2 is able to bind methylated CpG (mCG) or CpA (mCA) dinucleotides with similar affinity; further, it has been proved that mCAs are highly enriched within the body of genes normally repressed by MeCP2 (Kinde *et al*, 2015; Gabel *et al*, 2015; Guo *et al*, 2014; Chen *et al*, 2015; Lagger *et al*, 2017). In good accordance, Tillotson and colleagues have recently proposed that the capability of MeCP2 to bind mCG is inadequate to explain its role in RTT. Briefly, they generated a knockin mouse line in which the MeCP2 MBD was substituted with the equivalent domain from MBD2, able to selectively bind mCG, but not mCA. The knockin mouse carrying the chimeric protein displays severe Rett-like syndrome phenotypes, indicating that developing RTT requires MeCP2 binding with CH methylation. Importantly, the authors demonstrated that in this line the chimeric protein represses transcription only from mCG sites, leading to one-third of dysregulated genes with respect to those of the *Mecp2* null mice. Interestingly, these genes have high levels of methylation and they are connected with developmental disorders (Tillotson *et al*, 2021).

Although MeCP2 was primarily described as a transcriptional repressor, increasing evidence proposed novel functions for the protein. Among them, it was suggested the role of MeCP2 in regulating chromatin structure. Indeed, by neuronal ChIP-seq analysis, Skene and colleagues showed that MeCP2 does not regulate specific target genes, but instead it is globally bound to chromatin tracking methylated DNA. The authors proposed that due to its abundance in mature neurons, MeCP2 might act as an alternative linker histone leading to a specialized, more compact and transcriptionally inert chromatin structure. In possible good accordance with this model, the authors proved that WT neurons express lower levels of histone H1 than other cell types containing 10-30 times less Mecp2. Furthermore, they showed that, in *Mecp2*-null brain, H1 returns to its conventional stoichiometry, thus compensating in part for *MeCP2*-deficiency (Skene *et al*, 2010).

A possible role for MeCP2 in the activation of transcription has also been reported, probably occurring through the recruitment of cyclic AMP-responsive element-binding protein 1 (CREB1) to target gene promoters (Chahrour *et al*, 2008). On the same line, it has been proposed that MeCP2 binds 5-hydroxymethylcytosine (5hmC), an epigenetic

signal highly present in the body of neuronal active genes (Mellén *et al*, 2012). These results appear concordant with several studies profiling transcription in different *Mecp2* null brain regions and disclosing that most differential expressed genes are downregulated in the KO mice with respect to WT control (Tudor *et al*, 2002; Ben-Shachar *et al*, 2009; Chen *et al*, 2015). However, a recent publication from our laboratory provided a different explanation. Indeed, we compared the global chromatin structure of a *Mecp2* null brain with that of a KI model (*Mecp2*-Y120D) harbouring a mutation that impairs but not abolishes Mecp2 binding to chromatin. Surprisingly, we found that in the KI brain the chromatin appeared less condensed, while the complete lack of Mecp2 leads to a more packed and transcriptionally inert chromatin structure, probably due to the already mentioned compensatory mechanisms (Gandaglia *et al*, 2019). In concert with our findings, RNA sequencing performed on motor cortex and cerebellar autopsy samples from RTT patients identified more than 1500 significantly affected genes. Between these, a trend toward upregulation was found (Gogliotti *et al*, 2018).

Among the additional functions assigned to the protein, a direct or indirect role in protein synthesis has also been proposed. In fact, *Mecp2* mutant brain exhibits a down-regulation of the mTOR–AKT signalling pathway that is crucial for synaptic organization (Ricciardi *et al*, 2011). Moreover, since MeCP2 interacts with the splicing factor YB1, its involvement in alternative splicing has also been suggested (Young *et al*, 2005). In addition, a role for Mecp2 in the biogenesis of miRNAs was recently proposed, after having proved its capacity to interact with DGCR8, therefore hindering the assembly of the protein with the Drosha complex (Cheng *et al*, 2014).

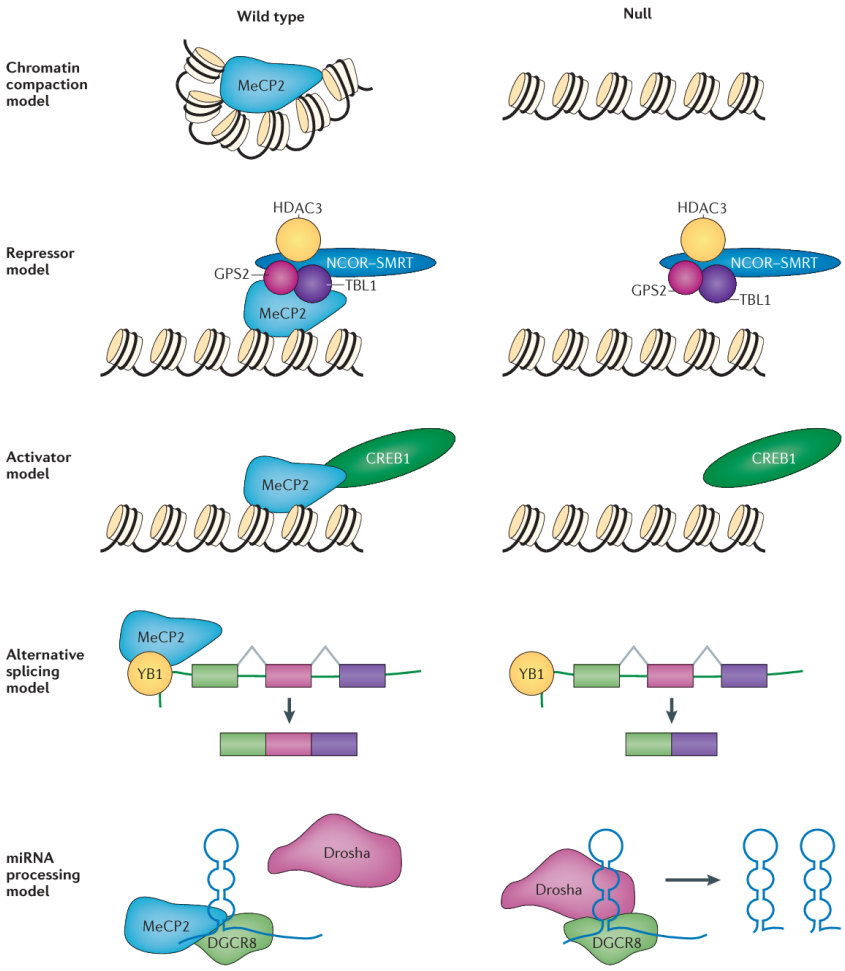

Figure 5. MeCP2 as a multifunctional protein. The cartoon represents several functions attributed to Mecp2 and the possible molecular consequences of its deficiency in *Mecp2* null samples (Lyst and Bird, 2015, License Number 5232140386360).

It is important to point out that MeCP2 versatility could be due to activity-dependent phosphorylation. The importance of post-translation modifications (PTMs) for RTT was established by using phospho-defective mice. For instance, a defective phosphorylation on MeCP2-S80 leads to RTT-like symptoms, such as motor impairment and the loss of body weight (Tao *et al*, 2009). Similarly, when MeCP2-S421 phosphorylation is disrupted, defects in dendritic and synaptic development and less proficiency in behavioural tests was observed (Cohen *et al*, 2011). Over the years, it has been discovered that several phosphorylation sites are differently modified in response to neuronal inputs, as membrane depolarization or stimulation with brain-derived neurotrophic factor (BDNF) (Tao *et al*, 2009; Ebert *et al*, 2013). This implies that an intricate pattern of PTMs

influences the aptitude of MeCP2 to interact with chromatin and protein partners (Bellini *et al*, 2014; Zhou *et al*, 2006; Tao *et al*, 2009).

Our group has contributed to these studies by characterizing two novel sites of MeCP2 phosphorylation: S164 and Tyr120. In particular, we found that cerebral phosphorylation of S164 is tightly regulated during neuronal maturation, affecting the affinity of Mecp2 for chromatin. Functional analysis revealed that temporal regulation of S164 phosphorylation influences the ability of MeCP2 to control neuronal morphology (Stefanelli *et al*, 2016). By characterizing MeCP2 phosphorylation at Tyr120, we found that this phospho-isoform is enriched at the centrosome both in dividing and postmitotic cells, affecting spindle geometry, mitosis, and microtubule nucleation, thus suggesting a novel function for MeCP2 in cell growth and cytoskeleton stability (Bergo *et al*, 2015). These studies have been further extended very recently proving a direct or indirect role for Mecp2 also in primary cilium formation and functioning (Frasca *et al*, 2020).

4.2.3 CDKL5: gene and protein

In 1988, during a transcriptional mapping project of the human X chromosome, Cyclin-Dependent Kinase-Like 5 (*CDKL5*) was recognised for the first time. Montini and colleagues isolated and sequenced a full-length transcript whose signature was homologous to several serine-threonine kinase genes, thus initially naming the protein Serine Threonine Kinase 9 (STK9)(Montini *et al*, 1998). Further studies disclosed that *STK9* gene disruption causes neurodevelopmental disorders assimilable to X-linked infantile spasms (ISSX). In fact, molecular investigation from Gècz laboratory reported that two unrelated female patients manifested early-onset severe infantile epilepsy, developmental delay and a dramatic mental retardation linked to the partial or total absence of *STK9* (Kalscheuer *et al*, 2003). Then, according to the high degree of sequence shared with cyclin-dependent kinases family, *STK9* was renamed *CDKL5* (Manning *et al*, 2002).

Human *CDKL5* gene occupies 228 kb of the Xp22 region and it comprises 27 exons (Hector *et al*, 2016), whose coding sequences encompass between exons 2-21.

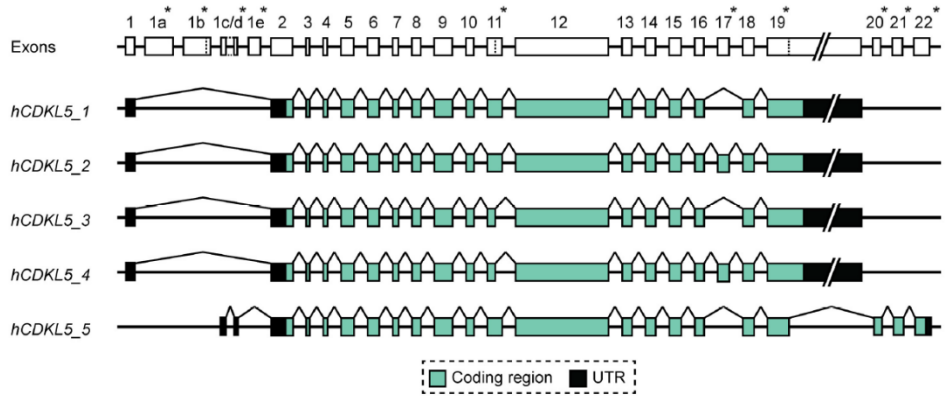

Figure 6. *CDKL5* gene and isoforms in human. Schematic representation of the five coding isoforms (*hCDKL5_1*, _2, _3, _4, _5). They diverge for exons indicated by asterisks (Hector *et al*, 2016)(Open Access).

As a result of alternative splicing, different *CDKL5* isoforms are present. In 2016, by analysing human tissue-specific RNA-seq datasets, Hector and colleagues described five main human isoforms and their principal differences (Figure 6). *hCDKL5_1* to *hCDKL5_4* isoforms are commonly expressed in the brain; however, *hCDKL5_1* is the most predominant in the CNS. *hCDKL5_1*, which corresponds to the previously named $CDKL5_{107}$ transcript (Williamson *et al*, 2012), could be found also in kidney, testis, prostate gland, thymus and thyroid gland. *hCDKL5_2* differs from *hCDKL5_1* for the inclusion of exon 17 that makes this isoform larger than the previous one. *hCDKL5_3* and *hCDKL5_4* diverge from *hCDKL5_1* and *hCDKL5_2* in the 3' end of exon 11 which lacks of 51 bases of the coding sequence. Isoform *hCDKL5_5* (previously identified as $CDKL5_{115}$) diverges from other transcripts at the 3' end. Initially the *hCDKL5_5* was supposed to be the main *CDKL5* isoform, however further investigation unveiled its great expression in testis, but a low presence in the CNS (Kalscheuer *et al*, 2003; Hector *et al*, 2016; Williamson *et al*, 2012). Of note, all the isoforms are present in the foetal brain.

Interestingly, most of the CDKL5 coding regions are well-conserved across species and in particular between human and mouse. Besides, Hector and colleagues performed an extended analysis of the mouse tissue-specific RNA-seq datasets and 23 coding exons were characterized. With respect to previous studies (Fichou *et al*, 2011; Williamson *et al*, 2012) they disclosed exon 1a, 20 and 21, which were formerly uncharacterised.

In the study five transcript isoforms were distinguished (Figure 7). Between these, both *mCdkl5_1* and *mCdkl5_2* can be found in the brain, although *mCdkl5_1* was prominent. In addition, *mCdkl5_1* is present in lung, thymus, kidney, colon, intestine, skeletal muscle and thyroid (Williamson *et al*, 2012; Hector *et al*, 2016). Importantly, *mCdkl5_1* and *mCdkl5_2* are homologous to human isoforms *_1* and *_2*. Since the remaining mouse isoforms do not show orthology to the human ones, they were named *mCdkl5_6*, *_7* and *_8* and they all share an alternative splice donor site in exon 19. *mCdkl5_6* and *mCdkl5_7* are expressed in the testis of the adult mouse, while *mCdkl5_8* appear mostly in the spleen although little amounts of transcript were also found in brain, heart, liver and lung and in testis (Hector *et al*, 2016).

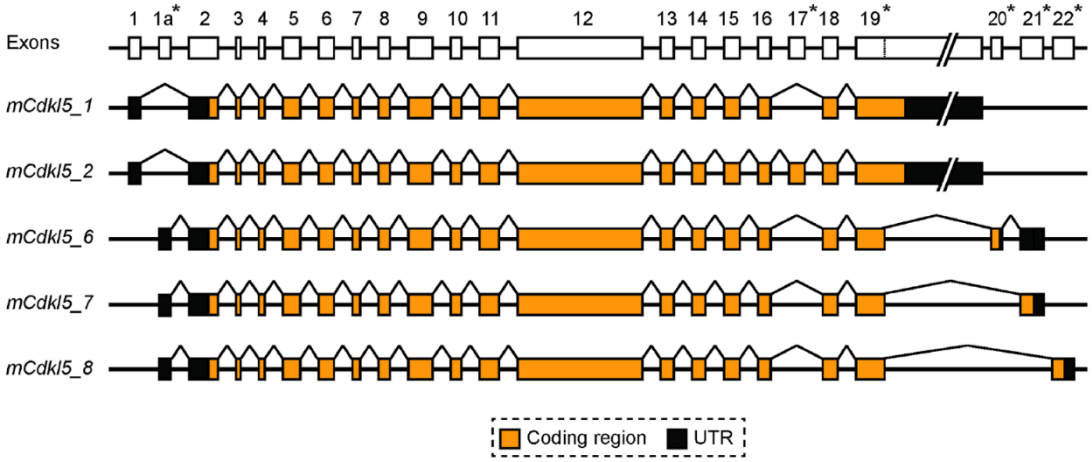

Figure 7. *Cdkl5* gene and isoforms in mouse. Schematic representation of the five coding isoforms in mouse (*mCDKL5*_1, _2, _6, _7, _8). They diverge for exons indicated by asterisks (Hector *et al*, 2016)(Open Access).

CDKL5_1 is the most abundant isoform in human and mouse (Hector *et al*, 2016) and it is composed of 960 residues (Figure 8). In the N-terminal portion of the protein the ATP binding region (amino acids 19–43) and the serine/threonine protein kinase active site (amino acids 131–143) are present and these domains are shared by all CDKL5 isoforms. Moreover, there is an activation loop that comprises the TEY (Thr-Glu-Tyr) motif sequence between catalytic subdomains VII and VIII, identical to those observed in MAPK and CDK kinase families (amino acids 169–171)(Roux & Blenis, 2004). Mutations in the TEY motif abolish CDKL5 autophosphorylation (Bertani *et al*, 2006).

CDKL5 also contains two putative nuclear import signals (NLS1 and NLS2) and an export NES signal in the regulatory C-terminus of the protein. Rusconi and colleagues

related these sequences to CDKL5 cellular localization and its shuttling from the nucleus to the cytoplasm and vice versa (Rusconi *et al*, 2008).

Figure 8. Schematic representation of the human isoform hCDKL5-1. The catalytic domain of the protein is depicted in green, while the C-terminus domain is displayed in red. The ATP binding site (ATP), the Ser/Thr kinase active site (S/T) and the TEY motif are presented in grey. The nuclear localization signals (NLS 1 and NLS 2) and nuclear export signal (NES) are depicted in blue (Balestra *et al*, 2019)(Open Access).

The most of the pathogenic missense mutations lies in the catalytic domain and generally lead to loss-of-function mutations, highlighting the importance of the kinase activity of the protein. Truncating mutations, instead, can be found along the whole gene (Figure 9). Fehr and colleagues investigated the possible existence of a genotype-phenotype correlation, reporting that mutations in the N-terminal kinase domain led to more severe clinical symptoms with respect to mutations in the C terminus. Further, patients carrying a truncating mutation often experience low frequency of epileptic seizures compared to those with no functional protein (Fehr *et al*, 2015, 2016). However, as it was shown for Rett syndrome, patients allocated in the same variant group (for example: no functional protein, missense or truncating mutation) often experience dissimilar symptoms severity. In accordance, MacKay and co-workers recently proposed to stratify patients based on their specific genetic mutation rather than on the historic variant groupings (MacKay *et al*, 2021).

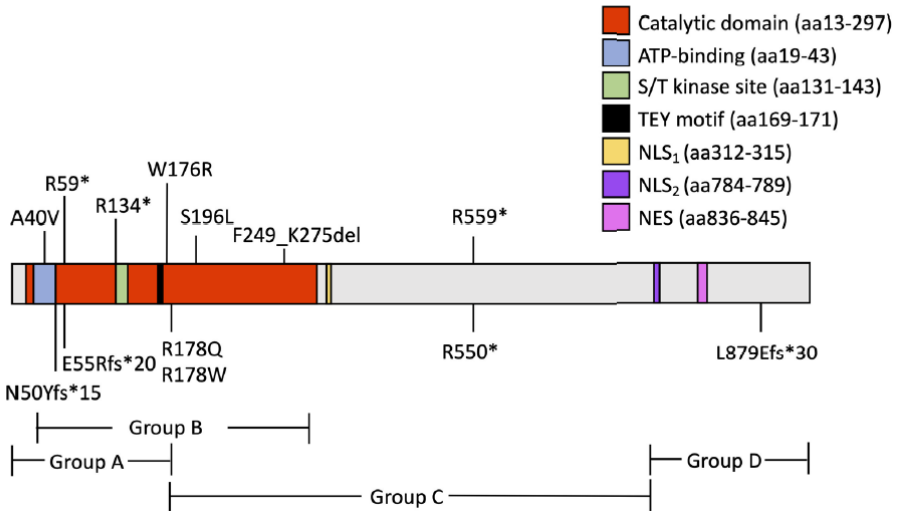

Figure 9. Location of recurrent pathogenic mutations in the CDKL5 protein. Mutations are grouped as: A. No functional protein. B. Missense mutations within the catalytic domain. C. Truncations between aa 172 and aa 781. D. Truncations after aa 781 (MacKay *et al*, 2021)(License Number 5232131228988).

CDKL5 expression is abundant in the brain and it is finely regulated during development, thus suggesting a relevant role of the kinase in brain maturation. Based on the findings that CDKL5 and MeCP2 belong to the same molecular pathway at least *in vitro* (Mari *et al*, 2005), their levels of expression were compared by immunohistochemistry and western blots, revealing a highly similar expression profile. In fact, Cdkl5 is slightly detectable in embryonic brains, while its expression is considerably upregulated after the first weeks of the mouse life, with maximum levels registered at P14. Then, the kinase persists at high levels in the adult brain (Rusconi *et al*, 2008; Chen *et al*, 2010; Nawaz *et al*, 2016; Schroeder *et al*, 2019). In the adult mouse brain, Cdkl5 is detectable in the cerebral cortex, hippocampus, cerebellum, olfactory bulb and brain stem, although its amount varies among different brain regions. Human adult cerebral tissues revealed an overall pattern of CDKL5 expression mainly overlapping with that one described in the adult mouse brain (Rusconi *et al*, 2008)(Figure 10A-B).

Further studies unveiled that CDKL5 is widely expressed in neurons while it appears almost undetectable in astrocytes. It is noteworthy that the specific distribution of Cdkl5 in neurons changes across brain regions and development. Rusconi and colleagues

analysed cytoplasmic and nuclear extracts obtained from different adult cerebral regions, disclosing that in the hippocampus, cortex, hypothalamus, and thalamus roughly 40% of the protein is nuclear. Nevertheless, the cytoplasmic fraction is almost 80% in the striatum and cerebellum (Figure 10C). In addition, the nuclear amount of Cdkl5 rises upon neuronal maturation, while it is largely cytoplasmic in young brains. Within neurons a relevant part of Cdkl5 is confined in the dendrites, highlighting its involvement in delivering signals to the cell nucleus or *vice versa*. Importantly, the ability of Cdkl5 to accumulate in the nuclear compartment is probably due to the C-terminal region of the protein and it is controlled through active import and export mechanisms. An elegant investigation explored CDKL5 subcellular accumulation through a hCDKL5 protein fused to GFP (GFP-CDKL5) in human HeLa cells. The protein appeared both in the nucleus and cytoplasm, whereas the accumulation of a truncated protein in the C-terminal (GFP-Δ831) is restrained into the cell nucleus, probably due to the lack of a signal for nuclear export (Rusconi *et al*, 2008). However, the same group demonstrated that the kinase localization is also dependent on neuronal stimulation. In fact, in hippocampal neurons glutamate treatment stimulated the rapid translocation from the nucleus to cytoplasm through the CRM1 receptor (Rusconi *et al*, 2011).

Eventually, CDKL5 can also be found at centrosomes of dividing cells and post-mitotic neurons. Investigation in SH-SY5Y neuroblastoma cells already suggested that CDKL5 expression causes a block of the cell cycle in the G(0)/G(1) phases and prompts cellular differentiation (Valli *et al*, 2012). Accordingly, *Cdkl5* deficiency in P40 KO mice leads to an increase of BrdU and Ki67 positive cells, therefore indicating an augment of actively proliferating cells (Fuchs *et al*, 2014a).

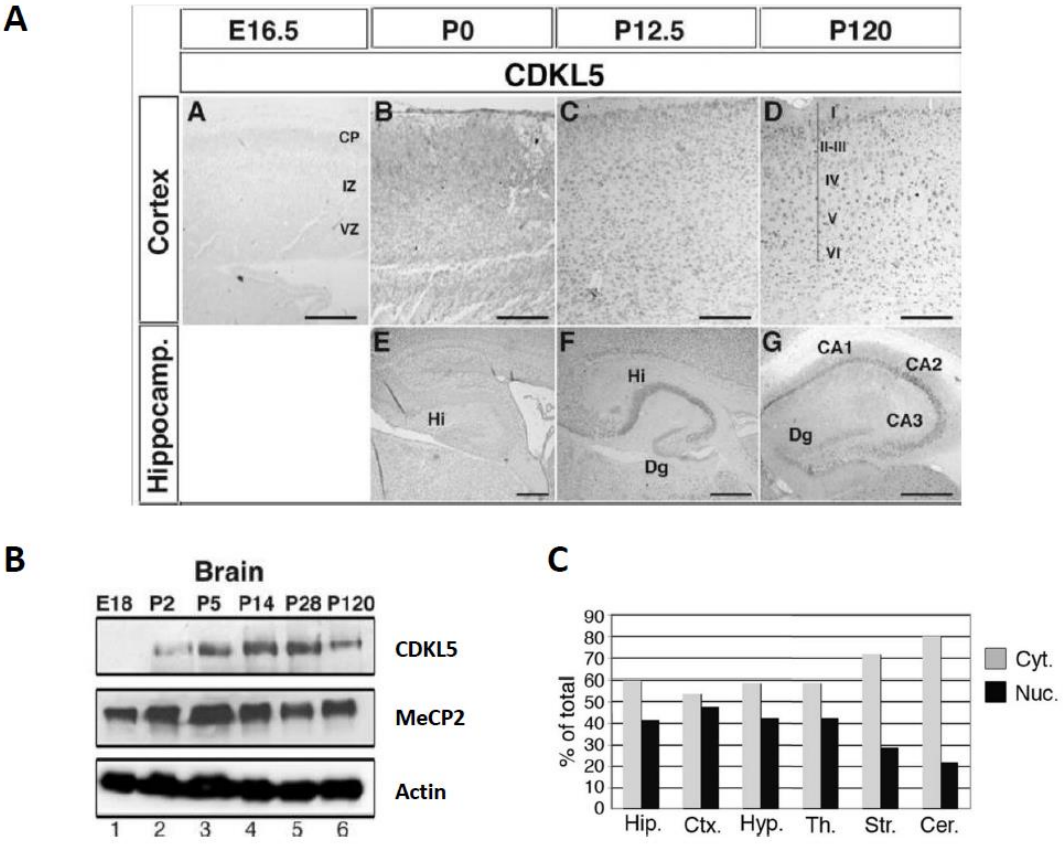

Figure 10. Cdkl5 expression is finely regulated in distinct brain regions and it changes during development A. Immunohistochemistry representing Cdkl5 abundance in the cerebral cortex and hippocampus at different time points. Dg, dentate gyrus; H, hilus; GL, granule cell layer; PL, Purkinje cell layer; MC, molecular cell layer. **B.** Western blot reporting Cdkl5 and Mecp2 amount in mouse total brain along neuronal maturation. Actin was used as internal standard. **C.** Graphic representation of the relative levels of cytoplasmic and nuclear Cdkl5 fraction in distinct brain areas. Hip., hippocampus; Ctx, cortex; Hyp., hypothalamus; Th., thalamus; Str., striatum; Cer., cerebellum (Rusconi *et al*, 2008)(Open Access).

4.2.4 CDKL5 functions in the cytoplasm

In accordance with its subcellular distribution, CDKL5 appears to exercise independent functions in the nucleus and cytoplasm. Concerning its roles in the cytosol, a recent quantitative phosphoproteomic screening aimed at identifying direct targets of CDKL5 activity permitted to isolate proteins involved in microtubule and centrosome functions, such as MAP1S and CEP131 (Muñoz *et al*, 2018). Interestingly, CDKL5 phosphorylation of MAP1S should block its ability to stabilize microtubules, and of relevance for my work, MAP1S also represents a bridge between microtubules and mitochondria. In fact, it was demonstrated that when *CDKL5* is mutated a dysregulation

in the trafficking of mitochondria occurs (Xie *et al*, 2011; Van Bergen *et al*, 2021). CEP131, instead, is a centrosomal protein having a role in the formation and functionality of primary cilia. When its levels drop defects in cilial morphogenesis occur (Graser *et al*, 2007). Accordingly, it has recently been reported that *Cdkl5*-knockdown neurons have elongated cilia although without significant alterations in the most relevant components of the Wnt or Sonic Hedgehog signaling pathways (Di Nardo *et al*, 2021). Of possible interest, ciliopathies and CDD share a pattern of symptoms such as developmental, cognitive delay and epileptic seizures. Eventually, Barbiero and colleagues recognised IQGAP1 as a novel interactor of CDKL5, a crucial protein for microtubules and actin interaction through the formation of a ternary complex with Rac1 and CLIP170. In the absence of CDKL5 the ternary complex is abolished, and microtubule dynamics are impaired (Barbiero *et al*, 2017).

CDKL5 also exploits an important function in neuronal morphogenesis. In particular, Chen et al. proved its interaction with Rac1, a member of the Rho GTPase family implicated in the formation and maturation of spines (Figure 11). Authors confirmed that *Cdkl5* knock-down impairs dendritic arborization, a phenotype that was reverted by Cdkl5 overexpression (Chen *et al*, 2010). Similarly, it was found a decrease in overall length of apical dendritic arbors in the granule cells and hippocampal neurons of homozygous female and hemizygous male *Cdkl5* null animals (Fuchs *et al*, 2014b; Tang *et al*, 2017a; Amendola *et al*, 2014). On the same line, Ricciardi and colleagues observed a decrease in spine density and impaired morphology in *Cdkl5* silenced hippocampal neurons. In particular, they noticed a significant increase in the number of filopodia-like and thin headed spines with respect to the stubby and mushroom-shaped spines. A possible molecular explanation might be found in the reported amplified activity of the glycogen synthase kinase 3β (GSK3β), an inhibitory modulator of neurite outgrowth, synapse formation and neurogenesis (Fuchs *et al*, 2015).

Further, the synaptic localization of CDKL5 speculates its involvement in synapse development and activity. In fact, CDKL5-PSD95 interaction targets CDKL5 to excitatory synapses and when the interaction is ablated, a drastic inhibition of spine formation and growth appears (Zhu *et al*, 2013; Pizzo *et al*, 2016). Thus, authors searched

for the molecular pathway involved in synapse formation and maturation proving that the netrin-G1 receptor (NGL-1) phosphorylation by CDKL5 intensifies NGL-1-PSD95 interaction (Ricciardi *et al*, 2012). In addition, recent evidence proved that *Cdkl5* silencing in hippocampal neurons radically influences GluA2 but not Glua1 levels. Of relevance, GluA2 Serine 880 (S880) phosphorylation allows the internalization of GluA2 containing AMPA-Rs and their consequent ubiquitination and degradation. Tramarin et al. unveiled a significant increase of S880 phosphorylation in *Cdkl5* KO neurons with respect to controls (Tramarin *et al*, 2018).

In 2016, Nawaz and colleagues unveiled Cdkl5 involvement in axon growth probably due to its interaction with Shootin1, an essential protein for axon formation. In fact, Cdkl5 overexpression leads to supernumerary axons, while its silencing impairs neuronal polarization, a phenotype that partially overlaps with neurons having altered Shootin1 levels. Nonetheless, it remains to be elucidated whether Cdkl5 directly phosphorylates Shootin1 or mediates its phosphorylation (Chen *et al*, 2010; Nawaz *et al*, 2016).

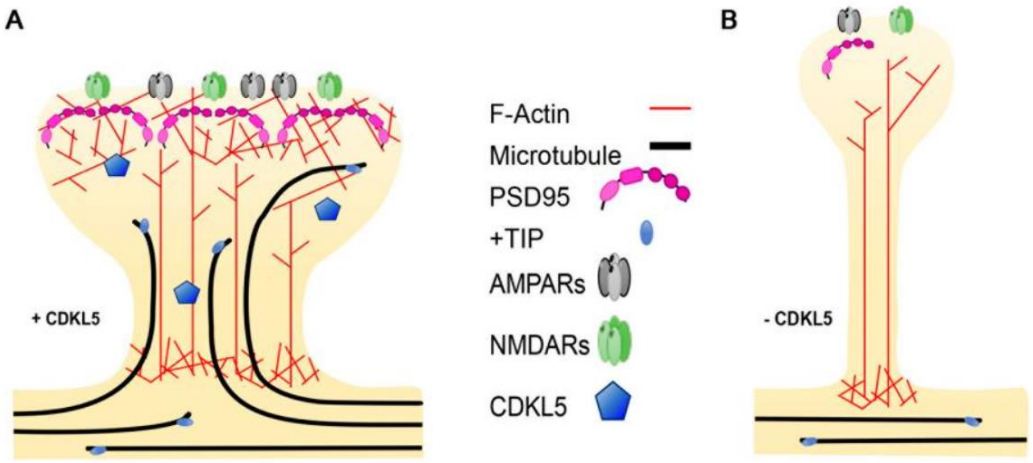

Figure 11. ***Cdkl5* deficiency affects dendritic spine morphology**. **(A)** Neuronal activation triggers the invasion of microtubules (MTs) in dendritic spines. The plus-end tracking proteins (+TIP) cooperate with actin-binding proteins enabling the process. **(B)** When *CDKL5* is lost, MTs are less dynamic and fail to invade the spines, thus preventing the formation of mushroom-shaped spines. (Barbiero *et al*, 2019)(Open Access).

4.2.5 CDKL5 role in the nucleus

Focusing on the nuclear compartment, CDKL5 was proposed to interact with the transcriptional repressor MeCP2 (Mari *et al*, 2005), the DNA methyl transferase DNMT1

(Kameshita *et al*, 2008) and histone deacetylase 4 HDAC4 (Trazzi *et al*, 2016), thus regulating gene expression (Figure 12).

Indeed, CDKL5, MeCP2 and Dnmt1 transcripts and proteins have comparable expression patterns in primary rat cortical neurons. Further, the capacity of CDKL5 to interact and phosphorylate MeCP2 or Dnmt1 was proved *in vitro* (Mari *et al*, 2005; Kameshita *et al*, 2008). However, it is noteworthy that the phosphorylation sites of interaction of Cdkl5 with MeCP2 and Dnmt1 have not been determined and, importantly, these interactions have never been proved *in vivo*.

In 2016, by using a phospho-proteomic-based study Trazzi and colleagues proposed HDAC4 as *in vitro* target of CDKL5 activity. Of relevance for CDD, HDAC4 localization between the nucleus and the cytoplasm is controlled by phosphorylation and in the *Cdkl5* knockout mouse brain exists a hypo-phosphorylated isoform of HDAC4 that is retained in the nucleus. However, and in line with HDAC4 role in memory formation (Chen *et al*, 2014; Chawla *et al*, 2003; Sando *et al*, 2012; Kim *et al*, 2012), when CDKL5 was re-expressed there is a restoration of HDAC4 subcellular localization to control levels and hippocampus-dependent memory of mutant mice were improved (Trazzi *et al*, 2016).

Lastly, it was proposed that the interaction of DYRK1A and CDKL5 regulates the subcellular distribution of CDKL5. In fact, DYRK1A is a constitutively active kinase that phosphorylates CDKL5 on serine 308, therefore enhancing in Neuro2a cells CDKL5 cytoplasmic retention (Oi *et al*, 2017).

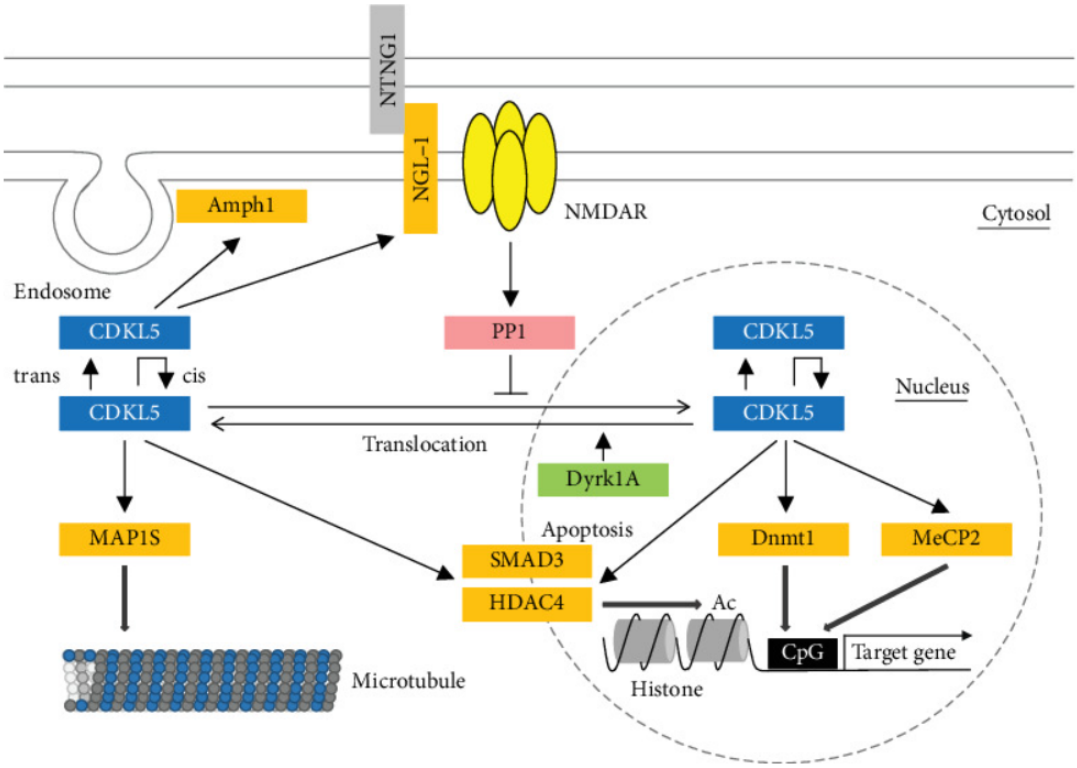

Figure 12. **CDKL5 and its interactors**. CDKL5 can be found both in the nucleus and in the cytoplasm and it exploits different roles according to its subcellular localization. In the nuclear compartment an interaction with MeCP2, Dnmt1, and HDAC4 was proposed. In the cytoplasmic compartment the phosphorylation of Amph1 and NGL-1 influences synapse formation and neurotransmission, while phosphorylation of MAP1S plays a role in microtubules stability (Katayama *et al*, 2020)(Open Access).

4.3 Animal Models

4.3.1 Mecp2 mouse models

To date numerous mouse models of Rett syndrome and CDD have been generated and they still embody a valuable tool for a mechanistic understanding of these diseases.

In 2001, two *Mecp2*-null mouse models were engendered to study Rett syndrome. The first one, the *Mecp2*$^{tm1.1Bird}$ line, was developed by deleting exons 3 and 4 in order to completely eliminate the protein (Guy *et al*, 2001). In the same year, Chen and colleagues generated a similar mouse line, *Mecp2*$^{tm1.1Jae}$, characterized by the deletion of exon 3 that led to the knockout of *Mecp2*, although preserving a tiny portion of the protein (Chen *et al*, 2001). The first mouse was developed in a C57Bl/6 background, while the second one in a mixed genetic background (129, C57BL/6 and BALB/c). In both models, hemizygous

Mecp2 male mice started to develop a behavioural phenotype at 3-5 weeks of age, with the onset of uncoordinated gait, hindlimb clasping, reduced spontaneous movement and irregular breathing (Figure 13). Heterozygous *Mecp2* females, that express the mutated allele only in almost half of neurons, exhibit a postponed onset of clinical symptoms between 3 and 9 months of age and display similar but less severe phenotypes. Of relevance, both *Mecp2*$^{tm1.1Bird}$ and *Mecp2*$^{tm1.1Jae}$ mutant mice present microcephaly and reduced neuronal cell size, although without neurodegeneration. The lifespan in both lines is around 7-10 weeks for males and 10 months for females (Guy *et al*, 2001; Chen *et al*, 2001).

Importantly, in 2007 the demonstration that the reactivation of *Mecp2* could reverse neurological symptoms and normalize lifespan of the *Mecp2*$^{tm1.1Bird}$ null mouse reached one of the most important milestones in RTT studies. These key findings suggested that *Mecp2* deficiency does not permanently damage neurons and symptom reversal may be possible also in RTT patients (Guy *et al*, 2007).

Figure 13. **Hindlimb clasping of *Mecp2*$^{tm1.1Bird}$ male mice**. Panels show normal spreading of hindlimbs in a 7 weeks WT mouse (left) compared to hindlimbs clasping in a littermate KO male (right) (Guy *et al*, 2001)(License Number 5232140262324).

Although null mice represent the main used model in RTT studies, it is noteworthy that most RTT patients carry point mutations and deletions, thus expressing a hypomorphic Mecp2 protein rather than harbouring a complete loss of it. To circumvent this caveat, different knockin mouse models were generated in order to assess the

functional and behavioural consequences associated with a genetic condition that better resembles the human one (Vashi & Justice, 2019). It was generally noticed that different mutations lead to similar, although sometimes less severe, behavioural phenotypes, while the molecular consequences of Mecp2 disruption change between mice models.

A first example is represented by the *Mecp2*^{308} mouse, which harbours a premature stop codon after codon 308, therefore lacking almost one third of the protein C-terminus. *Mecp2*$^{308/y}$ displays a less severe phenotype compared to the full knockout. It exhibits body tremors and motor abnormalities, together with spontaneous partial seizures from 2 months of age, and generally survives for at least 1 year. At the molecular level it was observed to have H3 hyperacetylation. Authors speculated that although the *Mecp2*^{308} truncated derivative preserves the TRD domain, it is unable to recruit histone deacetylase complexes (Shahbazian *et al*, 2002). This molecular phenotype could lead to a severe modification in chromatin structure and might enhance the accessibility of DNA to transcriptional regulators. In line with this, the presence of H3 hyperacetylation in *Mecp2* mutant mice was already described in other works, thus confirming that DNA methylation and MeCP2 binding are associated with deacetylation of histone H3 (Shahbazian *et al*, 2002; Thatcher & LaSalle, 2006; Nguyen *et al*, 2001).

Other knockin animals were developed and compared over the years. In 2016, Brown and colleagues demonstrated that mouse models of the RTT hotspots T158M, R306C and R133C well mimic the significantly divergent symptoms of patients, that generally feature a severe, intermediate and milder clinical condition (Brown *et al*, 2016). At the molecular level, the authors unveiled that in the two transgenic lines carrying mutations in the MBD domain (*Mecp2*^{T158M} and *Mecp2*^{R133C}), Mecp2 shows compromised stability and weaker DNA binding. On the other hand, the R306C mutation, that occurs in the NID of MeCP2, does not affect protein stability, but slightly impacts on chromatin binding.

In the previous chapter, I briefly discussed the *Mecp2*-Y120D mouse line developed in our laboratory, that mimics a pathogenic mutation found in a patient affected by classical Rett syndrome (Inui *et al*, 2001). The molecular comparison between the Y120D knockin line and the *Mecp2*$^{tm1.1Bird}$ strengthen the differences that arise from different pathogenic mutations, especially with respect to mice having a complete deletion of the gene. Indeed, in the knockin line, Mecp2 manifested the incapability to recruit NCoR and ATRX on heterochromatin, concurrently with a more accessible and transcriptionally

active chromatin structure compared to what observed in WT mouse brains. Of great interest, the null mouse unveiled an opposite behaviour; in fact, the *Mecp2*$^{tm1.1Bird}$ brain showed a less accessible chromatin structure, measured by reduced MNase accessibility, in particular on heterochromatic DNA. Concordantly, minor levels of active RNA polymerase II were measured on the *Mecp2* null chromatin (Gandaglia *et al*, 2019)(Figure 14).

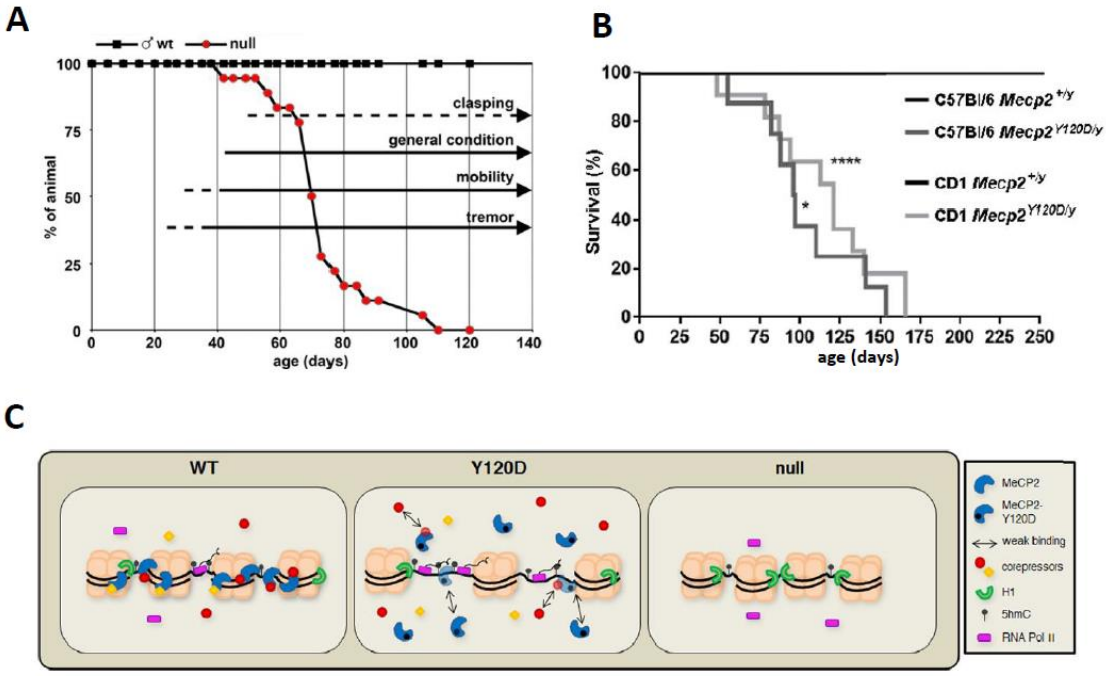

Figure 14. **Molecular and behavioural characteristics of *Mecp2*-Y120D mouse compared to the null line**. **A-B.** Graphs show a comparison between *Mecp2*-null (A) and *Mecp2*-Y120D (B) life span. C. Schematic representation of the differences in chromatin structure in WT, *Mecp2*$^{Y120D/y}$ and *Mecp2*-null brains (Gandaglia *et al*, 2019; Gigli *et al*, 2016)(License Number 5232140123770).

To map the neuronal origins of pathogenic behaviour, several conditional *Mecp2* mouse lines have been generated permitting to investigate the consequences of *Mecp2* deficiency in specific neuronal cell types or brain regions. The specific ablation of *Mecp2* in forebrain excitatory neurons (through a CamkII-Cre recombinase) causes RTT symptoms without affecting lifespan (Chen *et al*, 2001; Gemelli *et al*, 2006). On the other hand, mice with *Mecp2* deficiency in GABAergic neurons firstly exhibit normal behaviour and then develop typical RTT phenotypes, atypical EEG hyperexcitability, robust respiratory dysrhythmias and premature death (Chao *et al*, 2007). When *Mecp2* is conditionally deleted in the hypothalamus using a Sim1-cre, abnormal physiological

stress response was noticed together with aggressive and hyperphagic behaviour (Fyffe *et al*, 2008). Eventually, deleting *Mecp2* from either TH-positive dopaminergic and noradrenergic neurons in mice lead to a significant reduction of the neurotransmitter concentrations (Samaco *et al*, 2009).

4.3.2 Cdkl5 mouse models

As for *Mecp2*, several *Cdkl5* mice were generated to deeper comprehend the pathophysiology of the disease. In 2012, the first knockout animal was obtained through the deletion of exon 6, simulating a splice site mutation of a *CDKL5* patient. The deletion runs to a premature termination codon, producing an early truncation of CDKL5 in its N-terminal kinase domain that abolishes the kinase activity. Obtained *Cdkl5*$^{-/y}$ mice phenocopy several symptoms observed in human patients, such as motor and anxiety impairments and hyperactivity (Wang *et al*, 2012a).

Few years later, Amendola and colleagues engendered a *Cdkl5* knockout mouse through the deletion of exon 4. Similarly to the Wang model, hemizygous animals experience hindlimb clasping, impaired learning and memory, autistic features, hypoactivity and defective head tracking since two months of age (Amendola *et al*, 2014).

It is noteworthy that both mouse models do not display overt epilepsy, the main symptom of human patients. Authors hypothesized the presence of different molecular mechanisms that trigger spontaneous epileptic seizures between mice and humans. However, an atypical EEG response to convulsant following kainic acid treatment was found in the Amendola knockout mouse. Conversely, the occurrence of spontaneous seizures was explored also in the Wang line and it revealed a similar EEG pattern between mutant and WT mice. Nevertheless, authors examined neural circuit deficits, unveiling attenuated and delayed evoked-related potential peaks, that were hypothesised to be a secondary effect of an epileptic neuronal network (Wang *et al*, 2012a; Amendola *et al*, 2014).

To get deeper on the epileptic predisposition and synaptic dysfunctions of mouse models of CDD, Okuda and colleagues investigated this phenotype with a different knockout model harbouring the deletion of *Cdkl5* exon 2. Authors demonstrated that intraperitoneal injection of NMDA to *Cdkl5*$^{-/y}$ mice of 4 weeks prompted generalized tonic-clonic seizures, whereas only slight myoclonic seizures were observed in WT controls. Moreover, a great postsynaptic upregulation of NMDA receptors encompassing

GluN2B subunit was found, and it was abolished with the administration of the GluN2B-selective antagonist Ifenprodil. As a consequence, it was speculated the role of *CDKL5* in regulating seizure susceptibility through GluN2B-containing NMDARs (Okuda *et al*, 2017). Very recently, recurrent epileptic spasms were reported in two aged female mouse lines, *Cdkl5*$^{R59X/+}$ and *Cdkl5*$^{-/+}$, of CDD. Although with a different entity, both models show distinct features of background EEG and different frequency patterns (Mulcahey *et al*, 2020). It is noteworthy that the majority of the study focused on males because the utilisation of heterozygous females requires experimental challenges due to the delayed and more variable phenotypic progression; however, it is still controversial which gender better mirrors the disease. Interestingly, Fuchs and colleagues published an extended study of the female model of the disease, thus reporting memory impairment, affected motor coordination, decreased interest toward the environment and hyperactivity in the open field (Fuchs *et al*, 2018).

At the molecular level, the knockout line displays impaired phosphorylation of rpS6 in cortical neurons and a significant decrease of Akt, which is an up-stream modulator of rpS6 (Wang *et al*, 2012a). Further, a drastic decrease of the total length of apical dendritic arbors was found in *Cdkl5* null homozygous females and hemizygous males. Conversely, in heterozygous females there was a diffuse and bimodal distribution of the values, probably related to the random pattern of X inactivation (Amendola *et al*, 2014)(Figure 15). In addition, dendritic hypotrophy and defects in spine maturation and deregulation in phosphorylation levels of Akt and ERK1/2 were found in female mutant animals (Fuchs *et al*, 2018).

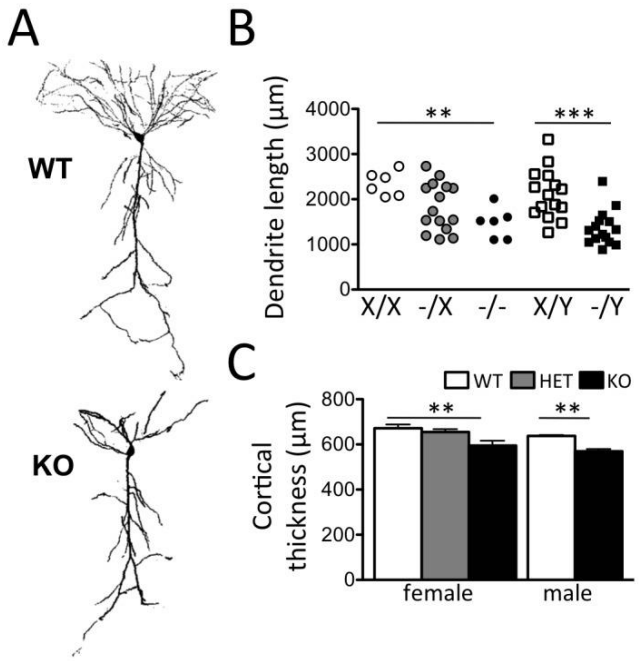

Figure 15. **Atypical dendritic branching in *Cdkl5* KO mice**. **A.** Representative images of reconstructed neurons from WT and *Cdkl5* KO mice. **B.** Total dendrite length was considerably diminished in female and male *Cdkl5* KO mice, while heterozygous females displayed a bimodal distribution. **C.** Graphs show a marked reduction of cortical thickness in mutant mice compared to WT (Amendola *et al*, 2014)(Open Access).

Similar features were observed also in the knockin *Cdkl5*^{R59X} model of the disease, that was developed to investigate the functional consequences of changes in synaptic glutamate receptor subunits (Yennawar *et al*, 2019). In fact, it was demonstrated that GluA2-lacking AMPAR dysregulation is involved in various disorders of excitatory-inhibitory disequilibrium and the R59X mutation is based on a human mutation associated with seizure and intellectual disability (Castrén *et al*, 2011). *Cdkl5*^{R59X} mice show hyperactivity, increased anxiety-like behavior, motor dysfunctions and poor social interactions, that were reverted through the administration of a GluA2-lacking AMPAR blocker (Yennawar *et al*, 2019).

As for Mecp2, conditional knockout mice were used to investigate *Cdkl5* function in different subtypes of neurons. Tang and colleagues disclosed that the selective ablation of *Cdkl5* from glutamatergic neurons (Nex-cKO) spoils enhanced spontaneous synaptic activity and modifies neuronal morphology (Tang *et al*, 2017a). A few years later the same group of researchers removed *Cdkl5* expression only from forebrain GABAergic

neurons (Dlx-cKO) and the mouse displayed an augment of excitatory synaptic transmission. Behaviourally, Nex-cKO shows compromised learning and memory, while in Dlx-cKO the hippocampal circuit hyperexcitability is connected with autistic-like phenotype (Tang *et al*, 2017a, 2019). Moreover, by removing *Cdkl5* in pre- or post-synaptic parts of dopaminergic neurons, it was proved that Cdkl5 is essential to control locomotor behaviour (Jhang *et al*, 2020).

To conclude, a very recent study shed light on the possibility of disease reversal. In fact, a genetic strategy was employed to gradually restore *Cdkl5* expression after the first stages of brain development (P40) and the resulted mouse model showed great amelioration of CDD-related behavioural defect and atypical NMDA receptor signalling, together with mitigated vulnerability to NMDA-induced epilepsy (Terzic *et al*, 2021).

4.4 The lack of translatable biomarkers in RTT and CDD

The *Biomarkers Definitions Working Group* described a biomarker as "a characteristic that is objectively measured and evaluated as an indicator of normal biological and pathogenic processes, or pharmacologic responses to a therapeutic intervention" (Biomarkers Definitions Working Group, 2001).

Since Rett syndrome and *Cdkl5* Deficiency Disorder were first described, only few implementable biomarkers have been defined, and none of them has a strong translatable value. As a possible consequence, many clinical trials failed and no cure for these disorders is available. An important limit of RTT and CDD is the intrinsic heterogeneity of the diseases. As a matter of fact, given the drastic variation in phenotype presentation, different patients respond diversely to the same treatment, also according to the wide role of *MECP2* and *CDKL5* and to degree of X chromosome inactivation (Emerson *et al*, 2017)(Figure 16). For this reason, the requirement of precision medicine has taken hold, and biomarkers might be fundamental to match the right treatment with the right patient.

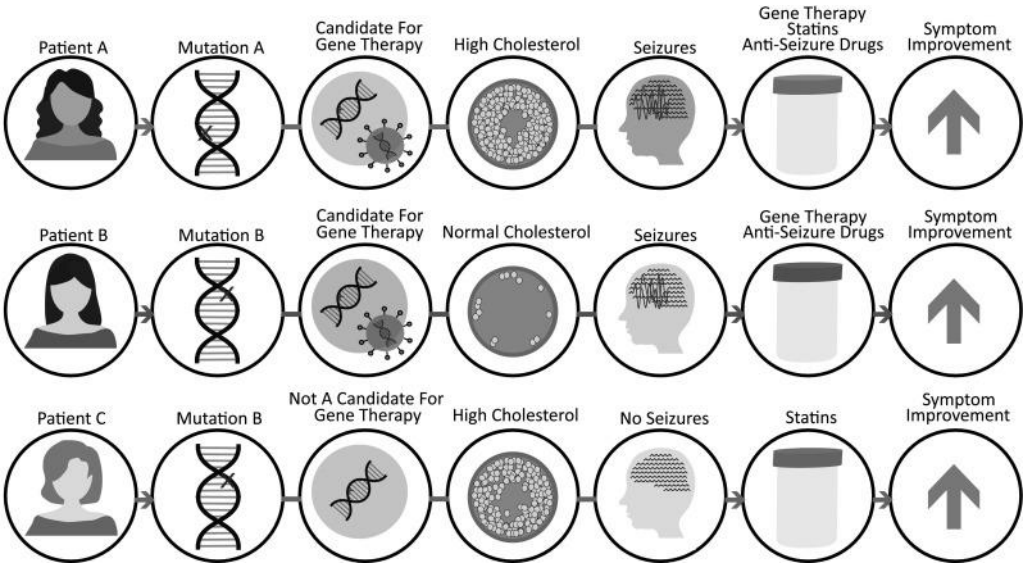

Figure 16. Precision medicine for RTT and CDD. Patients should receive individualized treatment based on their mutation and the different XCI skewing (Vashi & Justice, 2019)(Open Access).

One of the main methodologies to identify biological markers is electroencephalography (EEG). EEG procedures supervise neural reactions to a recurrent sensory stimulus (evoked potentials, EPs) or define the on-going background activity during resting state and give information about how neural networks run in the brain. Of relevance, most of the EEG signals originates from pyramidal cells of the cerebral cortex and hippocampus, cerebral regions that are strongly affected in RTT and CDD patients (Sörnmo & Laguna, 2005; Brown & Nunez, 1983).

Abnormal background EEG is a common characteristic of Rett syndrome and *CDKL5* Deficiency Disorder (Niedermeyer *et al*, 1986; Garofalo *et al*, 1988; Glaze, 2005). In auditory analysis, the "oddball" paradigm is used, in which a deviant random tone is produced in a sequence of standard tones. The deviant stimulus produces a greater amplitude "mismatch" response (mismatch negativity, MMN) on the EEG graphic. A recent clinical investigation on 14 RTT patients and 22 age-matched controls disclosed crucial differences in the duration of the MMN in RTT girls compared to healthy controls, thus reflecting a defect in the information processing in the RTT individuals (Foxe *et al*, 2016)(Figure 17).

Another approach for EPs is the visual evoked potentials (VEPs) that can be carried out with the support of patterned or unpatterned "flash" visual stimuli. In 2015 a study on

both mice and clinical patients detected a consistent decrease in VEP amplitude that became stronger in the later phases of RTT. In addition, RTT girls experienced a slower recovery from the principal peak of the VEP response that correlated with the *MECP2* mutation type (LeBlanc *et al*, 2015). Importantly, VEP is one of the most promising measurable outcomes also for CDD, especially because cortical visual impairment (CVI) is one of the main symptoms in human patients and clinical investigations already demonstrated a correlation between CVI and VEP (Demarest *et al*, 2019; Yan *et al*, 2020; Olson *et al*, 2021). At the preclinical level, Mazziotti et al. reported decreased cortical responses in amplitude in P30 mutant mice and, importantly, this reduction appeared to correlate with the impaired visual acuity in adult mutants. Of note, the study was carried out both in knockout male and heterozygous females, thus strengthening the relevance of the results (Mazziotti *et al*, 2017).

To summarize, EEG represents a promising biomarker for neurodevelopmental disease and it presents advantages such as low costs and wide availability. However, it is important to point out that limitations are also present. In fact, although sedation is not a basic requirement, a sleeping or quiet child is preferable to obtain stronger results. Also, a more reproducible and quantitative approach is mandatory because different studies reported dissimilar patterns of inter-electrode coherence.

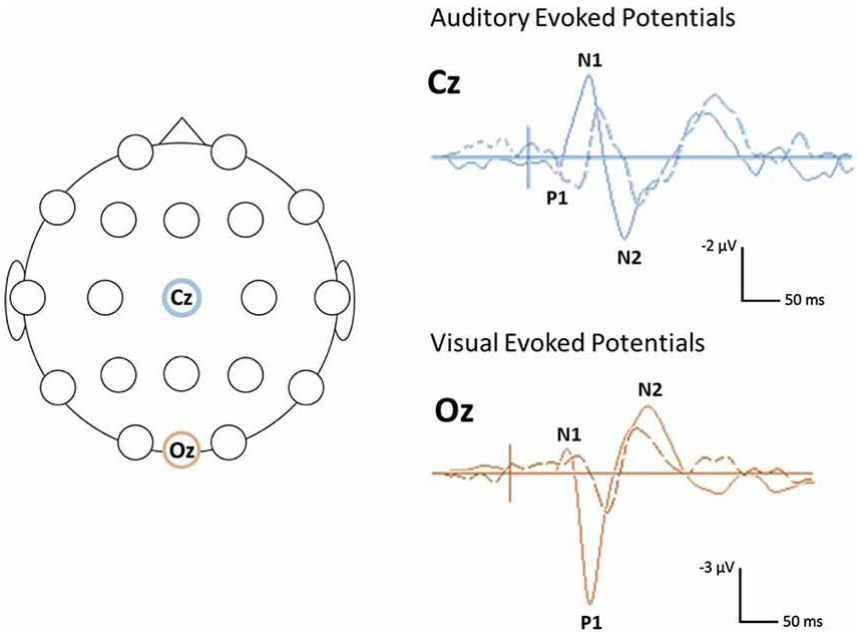

Figure 17. Representative image of visual and auditory EP waveforms and head locations. A 16-year-old girl having RTT (dotted line) was compared to an age-matched control (solid line). On the left it is depicted the position of the electrodes employed for the auditory (Cz) and visual (Oz) responses. P: primary positive component; N: negative component (Saby *et al*, 2021)(License Number 5224170704380).

In addition to EEG, pupillometry and cardiac oscillations have been considered as biomarkers in neurodevelopmental disease. Pupillometry is the measurement of pupil size and reactivity over time, while heart rate variability is the spontaneous modulation of the heart rate in wakefulness. Both parameters are affected in RTT patients. These methodologies represent an easy and low-cost method of analysis that, however, do not fit well with individuals carrying electronic implants or affected from sound disturbance such as machine noise (Artoni *et al*, 2020).

Another important instrument to obtain a valid biomarker is Magnetic Resonance Imaging (MRI), a powerful tool widely applied to ASD that enriches the understanding of neuropathological differences in neurodevelopmental disorders (Hernandez *et al*, 2015; Mahajan & Mostofsky, 2015; Lenroot & Yeung, 2013).

4.5 Magnetic Resonance Spectroscopy as a powerful approach to identify biomarkers

MRI is a powerful 3D imaging method, able to disclose functional and morphological alteration *in vivo* or from *ex vivo* samples. Due to its non-invasive characteristic, it was originally developed for anatomical imaging in humans; however, in recent years it has become popular also for studies with animal models (Hiremath & Najm, 2007; Hoyer *et al*, 2014) and many progresses have been made since the first report of a rat MR imaging over 40 years ago (Hansen *et al*, 1980).

MRI exploits the magnetic properties of hydrogen nuclei which are present in tissues in the form of water molecules. It is based on the physic principle that a moving charged particle induces a magnetic field and when an external radio frequency energy perturbs this alignment, nuclei can return to the resting state through a process called “relaxation time”. Tissues are characterized by two relaxation times: T1, which mirrors the rate at

which excited protons return to a state of equilibrium and T2, the time constant required to fall to the original value (Grover *et al*, 2015).

Importantly, MRI is a multiparametric tool, with different approaches described over years (Figure 18). Diffusion Tensor Imaging (DTI) measures the extent and the random motion of water diffusion, a phenomenon recognised as diffusion anisotropy. Based on the diffusion orientation it is possible to obtain a coloured map, where colours represent fiber's orientation and their brightness displays the degree of the anisotropy. Functional MRI (fMRI) describes regional and time-related changes in brain metabolism through the observation of the modifications connected to blood flow (DeYoe *et al*, 1994). Manganese Enhanced MRI (MEMRI) takes advantage of manganese ions (Mn^{2+}), which are analogues of calcium ions and can be internalized by neurons via Ca^{2+} channels (Silva & Bock, 2008; Silva *et al*, 2004). Magnetic Resonance Spectroscopy (MRS) gives information about metabolite levels. In contrast to classical MRI, MRS generates a spectrum, in which peaks can be attributed to chemical groups and metabolites, permitting its quantification (Hubesch *et al*, 1989).

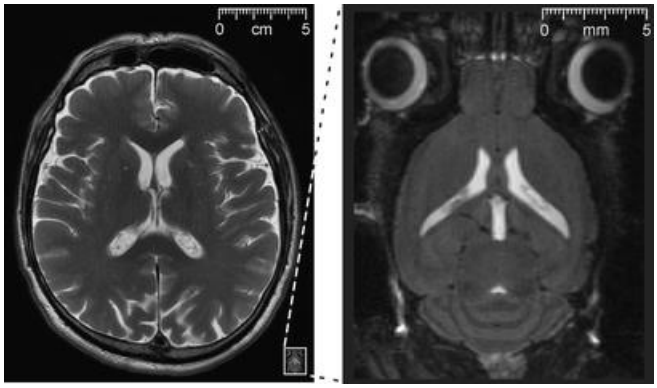

Figure 18. MRI in human and mouse. Comparison of Magnetic Resonance Imaging scans of a human (left) versus mouse (right) brain (Denic *et al*, 2011)(Open Access)

Although MRI has some limits, such as high costs, time-consuming investigations and the requirement of general anaesthesia, it has taken hold due to a multitude of advantages. First of all, it allows the study of living organisms without the exposure to potentially harmful ionizing radiation and it does not require contrast agents.

Moreover, MRI permits longitudinal studies to acquire multiple information from the same animal over time, a fundamental feature in neurodevelopmental diseases (Lau *et al*, 2008; Zhang *et al*, 2010). By using this technique, human studies on ASD patients reported an augment of brain development in the first years of life together with white matter deficits that seem to correlate with the onset of behavioural symptoms (Hardan *et al*, 2001; Aylward *et al*, 2002; Vaccarino & Smith, 2009; Ha *et al*, 2015). Contrasting data are described for corpus callosum, that was smaller in Piven et al. and Hardan et al., while a recent investigation reported a higher volume in ASD patients (Piven *et al*, 1997; Hardan *et al*, 2001; Lefebvre *et al*, 2015). On the other hand, MRS on autistic subjects showed increased glutamate levels in frontostriatal regions and reduced amount of GABA in anterior cingulate cortex, two brain regions related to cognitive functions, speech and social behaviour (Ito *et al*, 2017; Naaijen *et al*, 2017). Of relevance, despite over 70 genetic mouse models of autism having been generated, a very poor literature is present for volumetric analysis using MRI. Between these, Fragile X Mental Retardation 1 mouse showed atrophic arbor vitae (Ellegood *et al*, 2010), whereas Neuroligin3 KI and Integrin β3 KO mice displayed a decrease in total brain volume and white matter regions (Ellegood *et al*, 2011, 2012).

Of interest for my thesis, literature reported a consistent microcephaly in both human patients and mouse models of Rett syndrome (Casanova *et al*, 1991; Mahmood *et al*, 2010; Saywell *et al*, 2006; Ward *et al*, 2008; Ellegood *et al*, 2012). Other coherent findings are the shrinkage of the thickness of the motor cortex and corpus callosum (Saywell *et al*, 2006; Ward *et al*, 2008). More recently, Ellegood and colleagues analysed KO and the *Mecp2*^{308} mice, disclosing a decreased volume of several cerebral regions between mutants and wild type. Their findings also highlighted a variability in the neuroanatomy related to the type of the mutation (Ellegood *et al*, 2012). On the other hand, MRI literature on *Cdkl5* animal models is still poor. In addition to our study (Carli *et al*, 2021), it was recently described by Zerbi and colleagues a brain-wide connectivity mapping analysis in different mouse models of autism. Among them, authors explored the connectional signature of *Cdkl5* and *Mecp2* mice, thus revealing that they could be grouped together, consistently with the hypothesis that the two genes responsible for the diseases belong to the same molecular pathway (Zerbi *et al*, 2021; Mari *et al*, 2005). On

the other hand, contrasting results have been reported in human patients. Bahi-Busson and colleagues described consistent morphological abnormalities in white matter of the temporal poles, together with cerebellar atrophy (Bahi-Buisson *et al*, 2008). Oppositely, Yamamoto et al. showed no structural abnormality in any of the analysed patients, with a single exception in a 20 years CDD girl (Yamamoto *et al*, 2015). Very recently, a review described that MRI scan reflects the disease severity, with a more severe cerebral atrophy on male patients. However, brain anomalies were detected in few cases and at later stages of the disease, thus suggesting that they could be a secondary effect of epileptic seizures (Kobayashi *et al*, 2021).

To conclude, the versatility of MRI might enhance the comprehension of biological processes and the development of new therapeutic approaches.

5. Aim of the work

Rett syndrome and *Cdkl5* Deficiency Disorders are neurodevelopmental diseases characterized by a plethora of symptoms with a different severity in accordance to the type and location of the mutation. Despite several years of efforts, an incomplete comprehension of the molecular mechanisms driving the progression of the clinical symptoms is still present and, unfortunately, there is no available treatment for RTT and CDD. In fact, therapeutic approaches are still basically symptomatic. The multifunctional roles of MeCP2, responsible for most cases of RTT, and the wide functions of CDKL5, whose mutations are associated with CDD, together with, at least for MeCP2, regional specific dysfunctions associated with the protein deficiency, certainly represent main problems for the identification of effective therapies. Both genes are located on the X-chromosome and are subjected to random X inactivation pattern in females; moreover, especially for Rett syndrome, it is still debated which might be the most effective mouse model to be used in preclinical studies.

Crucially, we are still missing a qualitative and quantitative biomarker able to monitor the diseases' progression but also the concrete efficacy of a therapeutic treatment. To fill this gap of knowledge my thesis aimed at:

- using a multiparametric approach as Magnetic Resonance Imaging to investigate anatomical, functional and metabolic changes in the *Cdkl5*- and *Mecp2*-deficient mouse brain;
- starting a preliminary pharmacological approach based on the obtained results;
- longitudinally following both genders of a full knockout and a knockin (Y120D) mouse models of Rett syndrome, in order to investigate to what extent different *Mecp2* genetic lesions and gender affect disease evolution overtime.

6. Results

6.1 A comprehensive MRI study in a *Cdkl5* mouse model unveils defects in metabolites related to energy homeostasis

The results obtained in chapters 6.1.1, 6.1.2, 6.1.3, 6.2.1 have already been published in a work of which I appeared as first author (Carli *et al*, 2021).

6.1.1 MRI morphological analysis

MRI is a powerful non-invasive technique permitting to recognize anatomical alterations and to unveil biomarkers of disease progression. In particular, brain mouse imaging has a great relevance in various neurological and neurodevelopmental diseases and its application to Rett syndrome and *CDKL5* Deficiency Disorder might facilitate the acquisition of anomalies translatable into clinical assessment. Importantly, the relatively non-invasive character of MRI allows longitudinal investigations during development and aging.

Since an overall MR investigation in preclinical models of CDD was missing, we first focused on *Cdkl5* knockout mouse line (Amendola *et al*, 2014). To have a general indication of the translational potential of MRI, we examined *ex vivo* and *in vivo* brains of adult hemizygous male (P70) and heterozygous female (P160-195) mice, in order to compare animals with similar behavioural features between genders (Fuchs *et al*, 2018; Okuda *et al*, 2018). No difference in body weight was reported for all the animals included in the study (mean grams ± SEM: 40.6 ± 0.4 vs 40.5 ± 0.7 in *Cdkl5*$^{-/y}$ compared to WT males and 43.6 ± 1.7 vs 45.5 ± 1.3 in *Cdkl5*$^{-/+}$ vs WT females, Figure 19A). Similar results were obtained in analysing the brain weight after perfusion (mean milligrams ± SEM: 625.3 ± 20.1 vs 614.4 ± 19.3 in *Cdkl5*$^{-/y}$ compared to WT males and 643.9 ± 17.3 vs 651.0 ± 11.0 in *Cdkl5*$^{-/+}$ vs WT females, Figure 19B).

Thereafter, brains were MR scanned and virtually segmented in rostral to caudal slices; the cerebral area of each section was measured to obtain the total brain volume and brain sizes of *Cdkl5*$^{-/y}$ and *Cdkl5*$^{-/+}$ mice were compared to their corresponding controls. Interestingly, we found no volume alteration in both male and female mutant brains. As a matter of fact, the *ex vivo* measurements reported a perfect match among the two genotypes in each slice of analysis (Figure 19C-D) and the total brain volume was not

significantly different from that of controls (mean cm^3 ± SEM: 0.399 ± 0.009 vs 0.405 ± 0.007 in *Cdkl5*$^{-/y}$ compared to WT males and 0.400 ± 0.008 vs 0.400 ± 0.006 in *Cdkl5*$^{-/+}$ vs WT females, Figure 19E). Accordingly, *in vivo* quantitative examination of 23 brain slices of P70 *Cdkl5*$^{-/y}$ mice confirmed an identical cerebral size with respect to the corresponding *Cdkl5*$^{+/y}$ (Figure 19F-G). Further, we did not identify any gross structural alteration.

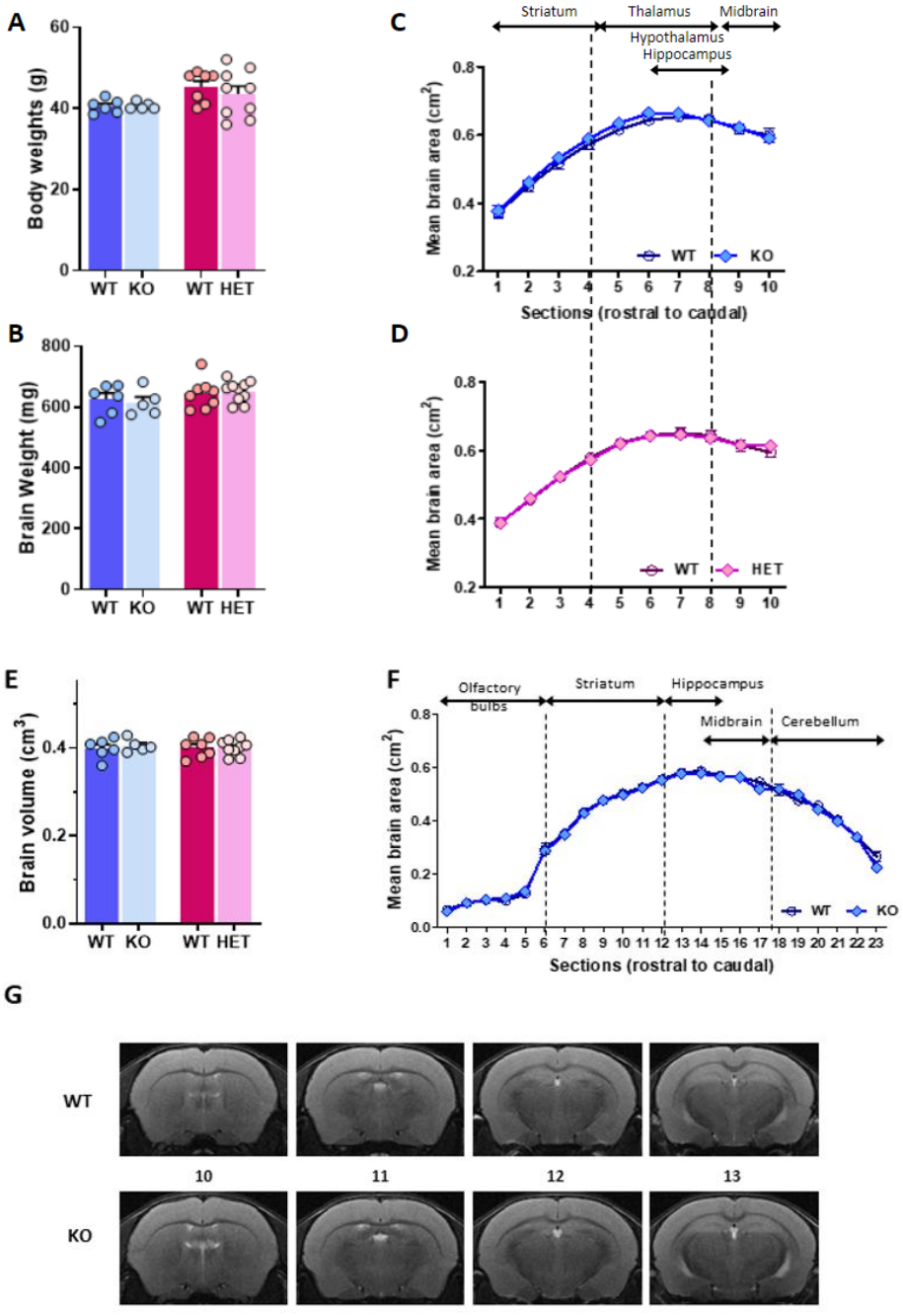

Figure 19. *Cdkl5* mutant mice do not manifest cerebral atrophy. **(A)** No difference was found in body weight (g) of *Cdkl5*$^{-/y}$ and *Cdkl5*$^{-/+}$ compared to controls. **(B)** Scatter dot plot showed that the weight (mg) of brains was similar among all groups. **(C, D)** *Ex vivo* MRI on male (C, n: WT = 6, KO = 5, P70) and female (D, n: WT = 7, HET = 9, P160-195) mouse brains showed matching cerebral area from slice 1 to 10. **(E)** Scatter dot plot indicated no difference in brain volume (cm^3) between WT and mutants of both genders. **(F)** *In vivo* MRI confirmed no meaningful alterations between KO (n = 5) and WT (n = 4) overall the brain. **(G)** Representative *in vivo* T2 weighted MR images of slices 10 to 13 from *Cdkl5*$^{+/y}$ and *Cdkl5*$^{-/y}$ brains. Student's t-test was performed in all the analysis and graphs represent mean ± SEM.

6.1.2 Manganese Enhanced MRI

Then, we tested whether *ex vivo* Manganese Chloride MRI (MEMRI) could permit identifying in which cerebral regions the loss of *Cdkl5* has a major impact. The purpose was to use this unbiased approach to select in which brain area investigating the neurochemical profile by proton magnetic resonance spectroscopy (^{1}H-MRS).

Mn^{2+} is a paramagnetic agent able to enter excitable cells through voltage-gated calcium channels Cav1.2. Since it shortens the relaxation time (T1) of tissues, MEMRI provides a map of cerebral activity (Duong, 2011; Sato *et al*, 2018).

Manganese enhancement of *ex vivo* brains from symptomatic mice (P70 for *Cdkl5*$^{-/y}$ and P160-195 for *Cdkl5*$^{-/+}$) was compared to WT littermates. The intraperitoneally administration of $MnCl_2$ resulted in enhancement of T1-weighted spin-echo images and we appreciated a consistent increase in the manganese accumulation across the whole brain of both *Cdkl5*$^{-/y}$ and *Cdkl5*$^{-/+}$ mice compared to saline-treated animals (blank) and to control littermates (Figure 20). The manganese contrast was not uniformly distributed, although *Cdkl5* mutants showed an intensified $MnCl_2$ signal in most of the analysed brain regions, in particular in those associated with cognitive functions and with the visual system (Table 1).

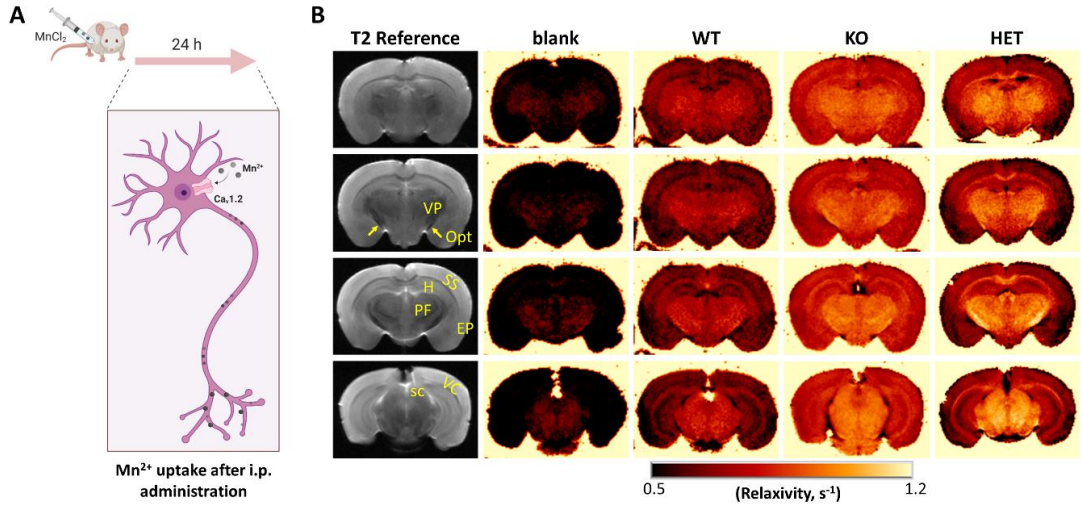

Figure 20. The *Cdkl5* mutant brain manifests a drastic increase of the MEMRI signal. (A) Simplified experimental design of MEMRI: 24 hours after an intraperitoneally administration of $MnCl_2$, manganese enters active neurons through voltage-gated calcium channels and it accumulates in an activity-dependent manner. As a paramagnetic ion, Mn^{2+} can shorten the relaxation time (T1) of tissues and unveiling the neuronal activity in identified regions of interest (ROIs). **(B)** Representative T2-weighted MRI images: investigated ROIs are depicted in the first column, while maps of relaxivity (1/T1, colored images) from blank, WT, *Cdkl5* KO and HET mice are shown in columns 2-5. EP: entorhinal-perirhinal cortex; H: hippocampus; Opt: optic tract; PF: parafascicular nucleus of the thalamus; SC: superior colliculus; SS: somatosensory cortex; VC: visual cortex; VP: ventral posterior nucleus of the thalamus.

A great manganese uptake was in fact displayed overall the hippocampus of *Cdkl5*$^{-/y}$ mouse ($p = 0.0286$), a brain region strongly related to several molecular and behavioural pathological phenotypes of CDD (Fuchs *et al*, 2014b; Okuda *et al*, 2017; Tang *et al*, 2017a)(Fuchs *et al*, 2014a; Okuda *et al*, 2017; Tang *et al*, 2017a). Conversely, *Cdkl5*$^{-/+}$ mice hippocampus exhibited only a not significant trend towards increase. To deepen a correlation between Mn^{2+} uptake and CDD phenotypes, we also investigated the principal nodes of the visual system, which is commonly affected in *Cdkl5* patients. Interestingly, the superior colliculus of both mutant groups displayed a significant manganese accumulation (KO: $p = 0.0286$ and HET: $p = 0.0303$). A similar enhancement was observed also in the visual cortex of the HET group (KO: $p = 0.114$ and HET: $p = 0.0025$), while no difference was found in the optic tract.

Of relevance, *Cdkl5*$^{-/y}$ and *Cdkl5*$^{-/+}$ experienced significant enhancement in T1 signal across several portions of the cerebral cortex, such as the auditory cortex (KO: $p = 0.0286$ and HET: $p = 0.0177$), the posterior parietal association cortex (KO: $p = 0.057$ and HET:

p = 0.202) and the entorhinal-perirhinal cortex (EP) (KO: p = 0.114 and HET: p = 0.0025). A similar trend to manganese increased signal was displayed also in the parafascicular nucleus (PF) and in the ventral posterior nucleus (VP) of thalamus of both genders (VP, KO: p = 0.114 and HET: p = 0.106; PF, KO: p = 0.114 and HET: p = 0.149). Eventually, an almost significant hyperintensity was found also in the KO hypothalamus (p = 0.057), but not in heterozygous females (p = 0.432).

Table 1. Manganese enhancement (%) of *Cdkl5*$^{-/y}$ and *Cdkl5*$^{-/+}$ compared to WT littermates

% Enhancement compared to WT (Mean ± SEM)		Male		Female	
		KO	p value	HET	p value
	Hippocampus	47.3 ± 14.6	0.0286*	21.7 ± 5.1	0.268
Cerebral Cortex	Auditory cortex	21.5 ± 8.6	0.0286*	43.0 ± 5.6	0.0177*
	Entorhinal-Perirhinal (EP) cortex	36.3 ± 17.4	0.114	77.3 ± 6.1	0.0025**
	Piriform cortex	47.7 ± 19.3	0.114	17.2 ± 6.3	0.432
	Posterior parietal association area	34.2 ± 13.2	0.057$	22.5 ± 6.1	0.202
	Retrosplenial cortex	35.2 ± 16.2	0.200	18.5 ± 7.7	0.432
	Somatosensorial cortex (SS)	31.3 ± 14.1	0.0826	22.4 ± 6.1	0.1042
Thalamus	Parafascicular nucleus (PF)	35.1 ± 10.5	0.114	14.1 ± 5.3	0.149
	Ventral posterior nucleus (VP)	34.5 ± 15.2	0.114	26.8 ±5.9	0.106
Visual System	Optic tract (Opt)	16.8 ±13.5	0.486	-9.7 ± 4.0	0.149
	Superior Colliculus (SC)	71.8 ± 25.6	0.0286*	27.7 ± 6.1	0.0303*
	Visual cortex (VC)	58.1 ± 31.5	0.114	63.4 ± 7.1	0.0025**
	Hypothalamus	54.8 ± 8.9	0.057$	-6.9 ± 7.6	0.432

*Mann-Whitney U test: * p < 0.05, ** p <0.01, $ p = 0.057*

6.1.3 Magnetic Resonance Spectroscopy

To corroborate the capability of MEMRI to select brain regions involved in the onset and the development of the pathology, for *in vivo* MR spectroscopy we selected a cerebral area that showed a prominent manganese uptake, the hippocampus, and a less reactive cerebral region, the thalamus. Although it would have been interesting to acquire the neurochemical profile of the visual system, technical limitations impeded to obtain a low

signal-to-noise ratio (SNR) in the superior colliculus and in the visual cortex. In addition, since MRS is a macroscopic analysis, we focused this study only in male *Cdkl5* animals in order to avoid confounding results connected to the variable degree of X-chromosome inactivation (XCI).

MR spectroscopy permits a precise investigation of the influence of genotype in regional brain metabolite levels and to the best of our knowledge this is the first study exploring the neurochemical profile in a mouse model of CDD. By positioning a single-voxel in the hippocampus (Figure 21A) and thalamus (Figure 22A), through LCModel software we were able to observe characteristic spectral patterns of the following metabolites: creatine with phosphocreatine (PCr+Cr), gamma-aminobutyric acid (GABA), glutamine (Gln), glutamate (Glu), glutathione (GSH), glycerophosphocholine with phosphocholine (GPC+PCh), lactate (Lac), myo-Inositol (Ins), N-acetyl aspartate (NAA), N-acetyl-aspartate with N-acetyl-aspartyl-glutamate (NAA+NAAG), phosphocholine (PCh), phosphocreatine (PCr) and taurine (Tau)(Table 2). In some cases, we reported the sum of two metabolites (i.e. GPC+PCh, Cr+PCr and NAA+NAAG) because of the cross-correlation between signals arising from adjacent peaks.

Table 2: Metabolite concentration (mM) in brain regions acquired by *in vivo* MRS

Metabolites (mM)	Hippocampus			Thalamus		
	WT	KO	p value	WT	KO	p value
Creatine-phosphocreatine (Cr+PCr)	8.1 ± 0.1	7.7± 0.1	0.028*	6.9 ± 0.2	6.5 ± 0.1	0.367
GABA	2.5 ± 0.2	2.3 ± 0.2	0.326	2.9 ± 0.1	2.7 ± 0.1	0.210
Glutamate (Glu)	10.2 ± 0.2	9.8 ± 0.2	0.281	10.2 ± 0.3	10.3 ± 0.2	0.947
Glutamine (Gln)	3.7 ± 0.2	2.9 ± 0.2	0.0044**	3.3 ± 0.3	3.3 ± 0.2	0.965
Glutathione (GSH)	1.9 ± 0.1	2.1 ± 0.1	0.320	1.7 ± 0.2	1.4 ± 0.1	0.145
Glu+Gln (Glx)	13.7 ± 0.2	12.6 ± 0.3	0.015*	13.4 ± 0.4	13.5 ± 0.2	0.691
Glu/Gln	2.7 ± 0.1	3.5 ± 0.2	0.017*	3.1 ± 0.2	3.2 ± 0.2	0.742
GPC+ Phosphocholine (PCh)	1.8 ± 0.1	1.5 ± 0.04	0.0015**	1.9 ± 0.1	1.7 ± 0.05	0.034*
Lactate (Lac)	3.0 ± 0.7	2.3 ± 0.2	0.425	4.1 ± 0.8	3.8 ± 0.6	0.726
Myo-Inositol (Ins)	4.7 ± 0.3	4.5 ± 0.2	0.585	3.8 ± 0.1	3.7 ± 0.2	0.637

NAA	7.6 ± 0.4	6.9 ± 0.2	0.114	8.4 ± 0.6	8.0 ± 0.3	0.492
NAA+NAAG	8.5 ± 0.4	7.5 ± 0.2	0.034*	8.9 ± 0.4	8.6 ± 0.2	0.579
Phosphocholine (PCh)	1.6 ± 0.1	1.1 ± 0.1	0.229	N.D	N.D.	-
Phosphocreatine (PCr)	5.8 ± 0.6	5.8 ± 0.5	0.942	5.6 ± 0.9	4.5 ± 0.5	0.445
Taurine (Tau)	9.2 ± 0.5	8.9 ± 0.4	0.717	4.3 ± 0.2	3.9 ± 0.1	0.077$

*Mann-Whitney U test: * p< 0.05, ** p< 0.01; $ p=0.053; N.D. not detectable*

Initially, we analysed the data using the Partial Least Squares Discriminant Analysis (PLS-DA). This multivariate statistical method allowed to separate *Cdkl5* KO and WT littermates for their metabolic profile (Figure 21B, 22B). Metabolites that mainly influenced the cluster discrimination were identified by variable's importance in the projection (VIP) and we focused on those having a score >1.2 (Figure 21C, 22C).

First, we compared results from the hippocampus of *Cdkl5*$^{-/y}$ and *Cdkl5*$^{+/y}$ animals (Figure 21D-E). MRS unveiled in the mutant mouse a downregulation of metabolites having well-defined roles in energy metabolism and neurotransmission, such as Glu, Gln, NAA and total creatine. In fact, we found a higher glutamate to glutamine ratio in mutant hippocampus with respect to WT (27.4 ± 8.0%; p = 0.017). Notably, this was caused by a significant reduction of glutamine levels (-22.6 ± 4.6%; p = 0.0044), since glutamate amounts were unaffected in KO mouse (-4.4 ± 2.3%; p = 0.281).

In addition, the sum of creatine and phosphocreatine (Cr+PCr) was significantly different among groups, being lower in KO hippocampus compared to WT (-4.4 ± 1.4%; p = 0.028). Creatine plays a pivotal role in brain energy homeostasis and ATP buffering in numerous ATP-producing processes in neurons and glia (Wyss & Kaddurah-Daouk, 2000; Wallimann *et al*, 1992). On the same line, NAA is considered a reliable marker for monitoring neuronal energy impairment (Vagnozzi *et al*, 2007) and we found that the sum of NAA and its metabolite NAAG displayed a significant drop (-11.2 ± 2.5%, p = 0.034) in KO mouse. On the other hand, lactate, an indicator of altered metabolism (McKnight, 2004) was barely measurable in both genotypes, suggesting that there was no critical energy failure.

Eventually, the concentration of total choline (GPC+PCh) was significantly deregulated in KO mice compared to WT (-14.9 ± 2.5% relative to WT; p = 0.0015).

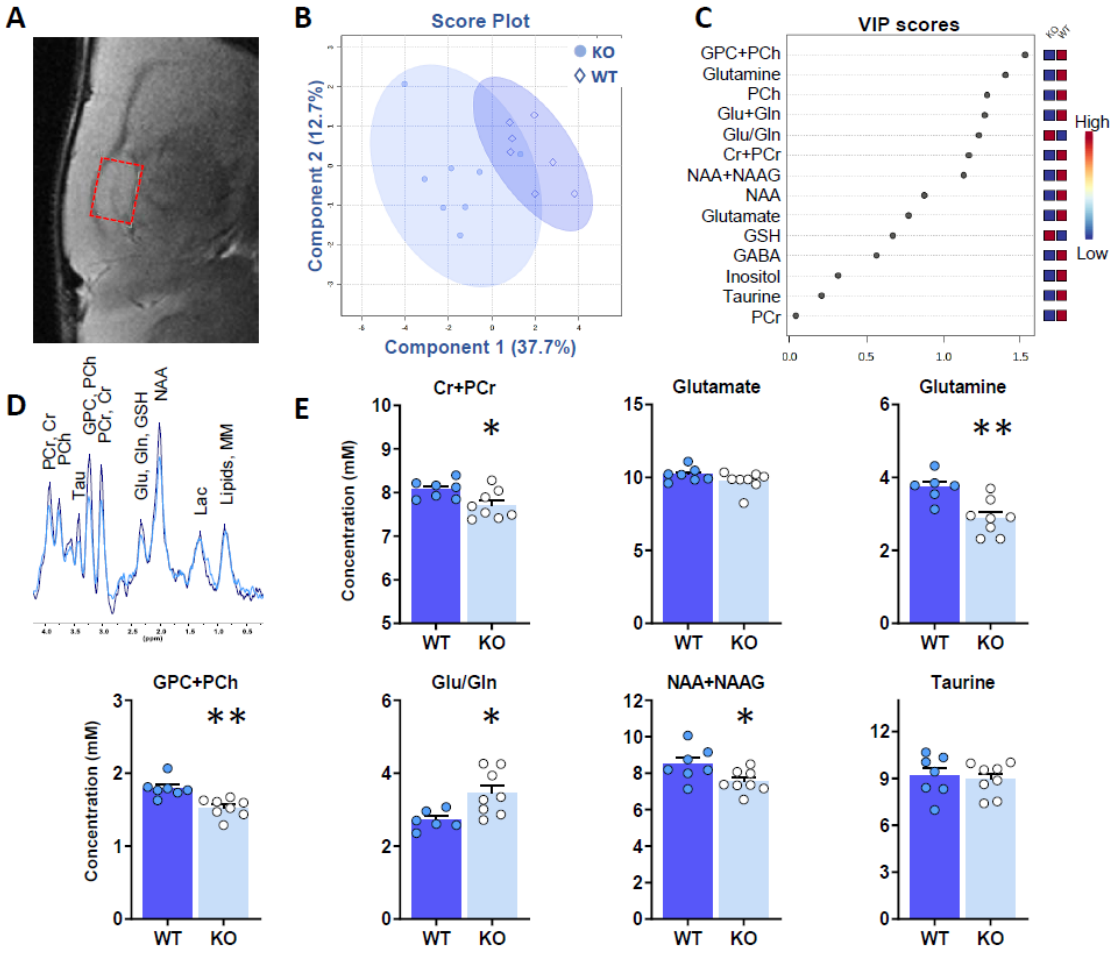

Figure 21. ***In vivo*** **MRS of KO hippocampus discloses a severe downregulation of metabolites related to energy homeostasis**. **(A)** Voxel placement in the left hippocampus. **(B)** Partial Least Squares-Discriminant Analysis (PLS-DA) in WT (n = 7) and *Cdkl5* KO (n = 8) animals. **(C)** The top metabolites chosen on the basis of variable's importance in the projection (VIP) scores (>1.2). **(D)** *In vivo* ^{1}H-MRS spectra from the hippocampus of a KO (light blue) and WT (dark blue) mouse. **(E)** Scatter dot plots showed the principal metabolites measured through MR spectroscopy. Total creatine (Cr+PCr), glutamine, GPC+PCh, Glu/Gln ratio and NAA+NAAG are dysregulated in KO hippocampus. Cr: Creatine; Glu: glutamate; Gln: Glutamine; GPC: glycerophosphocholine; PCh: phosphocholine; PCr: phosphocreatine; NAA: N-acetyl-aspartate; NAAG: N-acetyl-aspartyl-glutamate. Statistical significance assessed by Mann-Whitney U-test (Glu) or Student's t test (Cr+PCr, Gln, GPC+PCh, Glu/Gln, NAA+NAAG and Tau) in accordance with D'Agostino-Pearson normality test for data distribution: * $p < 0.05$, ** $p < 0.01$. All graphs represent mean ± SEM.

To corroborate the capability of MEMRI to mirror the presence of a neuronal dysfunction in the most reactive brain regions, we compared MRS hippocampal results with those in the thalamus (Table 2 and Figure 22), which reported a faint manganese

contrast. In KO thalamus we found a lower rate of the GPC+PCh (-10.3 ± 2.5%, p = 0.034), whose levels reflect alterations in membrane turnover and neurotransmission. Furthermore, we observed a trend toward reduction in the anti-oxidant taurine (-10.3 ± 3.0%, p = 0.077). All in all, MR spectroscopy confirmed a milder effect in the neurochemical profile of the thalamus with respect to hippocampus, although both brain districts evidenced defects in metabolites related to energy homeostasis.

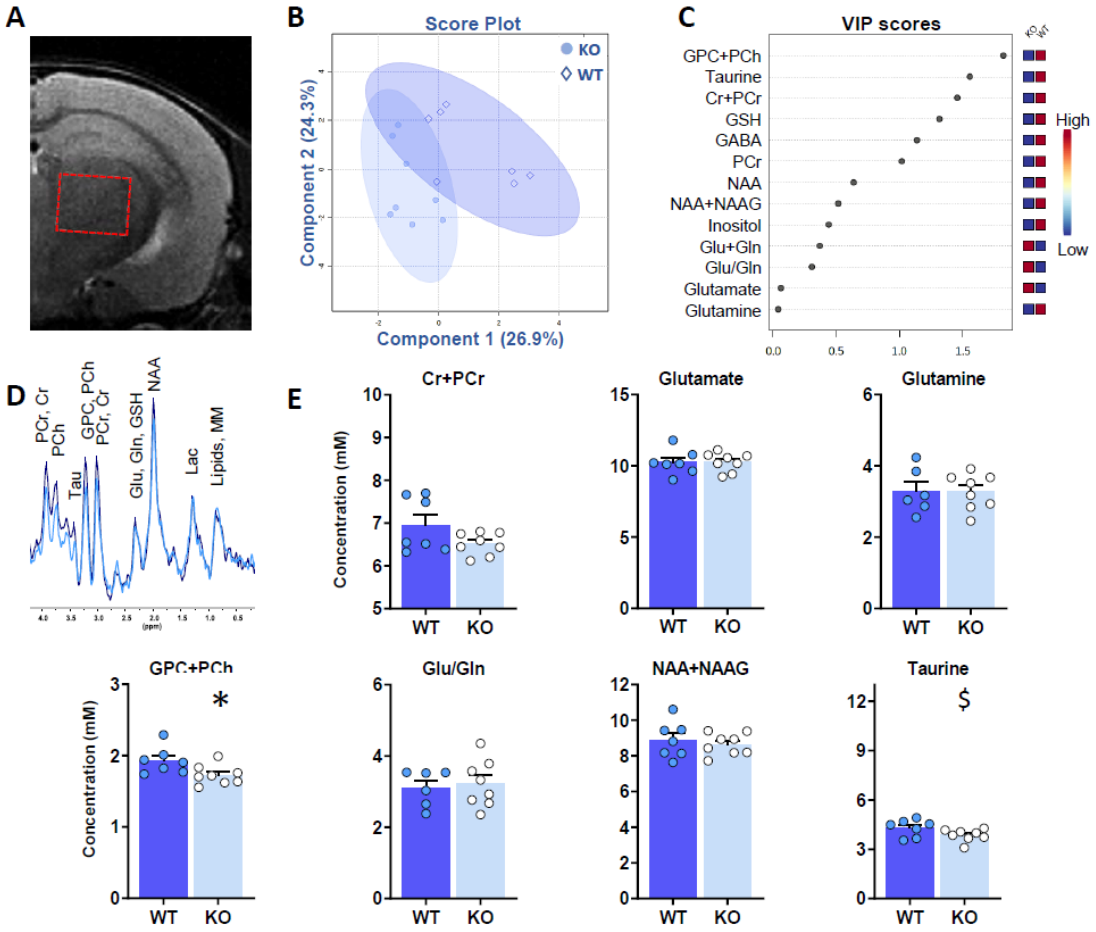

Figure 22. *Cdkl5* KO thalamus reveals a significant defect only in total choline. **(A)** Voxel placement in the right thalamus. **(B)** Partial least-squares discriminant analysis (PLS-DA) showing the segregation of *Cdkl5* KO metabolites (n = 8) compared to WT mice (n = 7). **(C)** VIP score indicated the metabolites having the higher influence to groups discrimination (VIP score >1.2). **(D)** *In vivo* ^{1}H-MRS spectra from thalamus of a KO (light blue) and WT (dark blue) mouse. **(E)** Principal metabolites measured through MR spectroscopy. Total choline (GPC+PCh) was significantly reduced, while taurine displayed a tendency toward reduction in KO thalamus. Cr: Creatine; Glu: glutamate; Gln: Glutamine; GPC: glycerophosphocholine; PCh: phosphocholine; PCr: phosphocreatine; NAA: N-acetyl-aspartate; NAAG: N-acetyl-aspartyl-glutamate. Statistical significance assessed by Mann-Whitney U-test (PCr+Cr) or Student's t test (Glu, Gln, GPC+PCH, Glu/Gln, NAA+NAAG and Tau) in accordance with D'Agostino-Pearson normality test for data distribution: * $p < 0.05$, $ $p = 0.077$. All graphs represent mean ± SEM.

6.2 *Cdkl5* KO brain features shortage of ATP and shows altered levels of AMPK and complex IV of the electron transport chain

6.2.1 Cdkl5 deficiency affects mitochondrial functions in the murine hippocampus

In accordance with the observed metabolite dysregulation and few recent works reporting a possible link between *Cdkl5* deficiency and energy homeostasis impairment (Pecorelli *et al*, 2015; Jagtap *et al*, 2019; Vigli *et al*, 2019), we proceeded exploring mitochondrial functions in the hippocampus of *Cdkl5* null mice. By using CellTiter Glo Luminescent kit (Chida *et al*, 2012) we measured ATP levels in WT and KO hippocampi, reporting a drastic reduction in the null tissues (-35.0 ± 4.2%)(Figure 23A).

Around 20% of the ATP produced in the body is dedicated to the brain (Magistretti & Allaman, 2015), whose functions depend on an adequate energy supply. ATP is produced by mitochondria and fluctuation in ATP amount could be strictly related to mitochondrial number. We thus used qPCR to calculate the mitochondrial DNA copy number (mtDNA-CN) and no difference in mitochondrial to nuclear DNA ratio was found in KO and WT hippocampi (+1.2 ± 0.4%)(Figure 23B). To understand the molecular causes of the reported ATP reduction, we investigated mechanisms necessary for restoring ATP homeostasis. It is well known that adenosine monophosphate-activated protein kinase (AMPK) senses metabolic impairment. In response to the depletion of the intracellular ATP, AMPK phosphorylation of threonine 172 is able to promote catabolism and to re-establish ATP levels (Ronnett *et al*, 2009). Therefore, we measured AMPK levels by western blot and we found a significant decrease in AMPK Thr172 phosphorylation (+18.2 ± 4.3%) in *Cdkl5*$^{-/y}$ hippocampus (Figure 23C). Intriguingly, in addition to its role in restoring ATP balance, AMPK is involved in long-term memory formation and synaptic plasticity (Dash *et al*, 2006; Marinangeli *et al*, 2018), thus suggesting a possible link between its deficiency and hippocampal impairment described in CDD.

To increase our comprehension of the possible molecular causes of the mitochondrial defect, we also evaluated in KO and WT hippocampi the mRNA levels of several genes involved in mitochondrial homeostasis (Figure 23E). First, we selected the transcriptional coactivator peroxisome proliferator-activated receptor-γ coactivator-1α (Pgc-1α), a crucial regulator of mitochondrial content. In fact, it enhances mitochondrial volume and function by upregulating numerous nuclear transcription factors implicated in the

expression of genes required for mitochondrial health (Menzies & Hood, 2012; Lin *et al*, 2005; Scarpulla, 2008). In accordance with mtDNA content, we found unaffected *Pgc-1α* levels in KO hippocampi (-9.8 ± 4.7%). To strengthen the hypothesis that mitochondrial number is unaltered in our experimental model, genes related to fusion and fission as Mitochondrial Fission Protein 1 (*Fis-1*) and Optic Atrophy 1 (*Opa-1*) were then considered and their levels were found to be comparable to WT (-6.5 ± 7.9% and -4.8 ± 5.7%, respectively). Besides, to have a complete overview, we added to the analysis Tomm40, the central pore-forming subunit of the translocase complex in the mitochondrial outer membrane, and Timm23, which is located in the inner membrane (Lohret *et al*, 1997; Mokranjac & Neupert, 2015). As before, no difference between genotypes were found (-4.4 ± 8.2% and -2.1 ± 6.9%, respectively).

We then focused on genes related to ATP production, that depends on electron transfer through the process of oxidative phosphorylation (OXPHOS). OXPHOS is exploited by five multimeric enzyme complexes that form the electron transport chain (ETC) (Wallace, 2005) and we chose one representative gene from each ETC complex and measured their expression at the transcriptional and molecular level (Figure 23D-F). We observed a significant reduction in the mRNA levels of the complex IV gene *Cox-7b* (-31.1 ± 12.6%; Figure 23D), that codifies for Cytochrome C Oxidase Subunit 7B. On the contrary, the expression of the other analysed genes, corresponding to *Ndufv2* (NADH dehydrogenase ubiquinone flavoprotein 2; Complex I), *Sdha* (succinate dehydrogenase; Complex II), *Uqrc1* (ubiquinol cytochrome c oxidoreductase chain 1, Complex III) and *Atp5a1* (ATP synthase F1 subunit alpha; Complex V) resulted comparable between WT and KO. Accordingly, we conducted western blot of OXPHOS complex subunits by using an antibody cocktail containing five antibodies, one each against a single complex subunit. Importantly, antibodies in the cocktail were selected because they are each against a subunit which is labile when its complex is unassembled and between them only complex IV Mtco1 is a mitochondrial DNA (mtDNA) encoded subunit. Of relevance, we found that the KO mouse hippocampus exhibits a strong decrease in Mtco1 levels (-12.1 ± 4.2%, Figure 23F), therefore confirming a defect in complex IV.

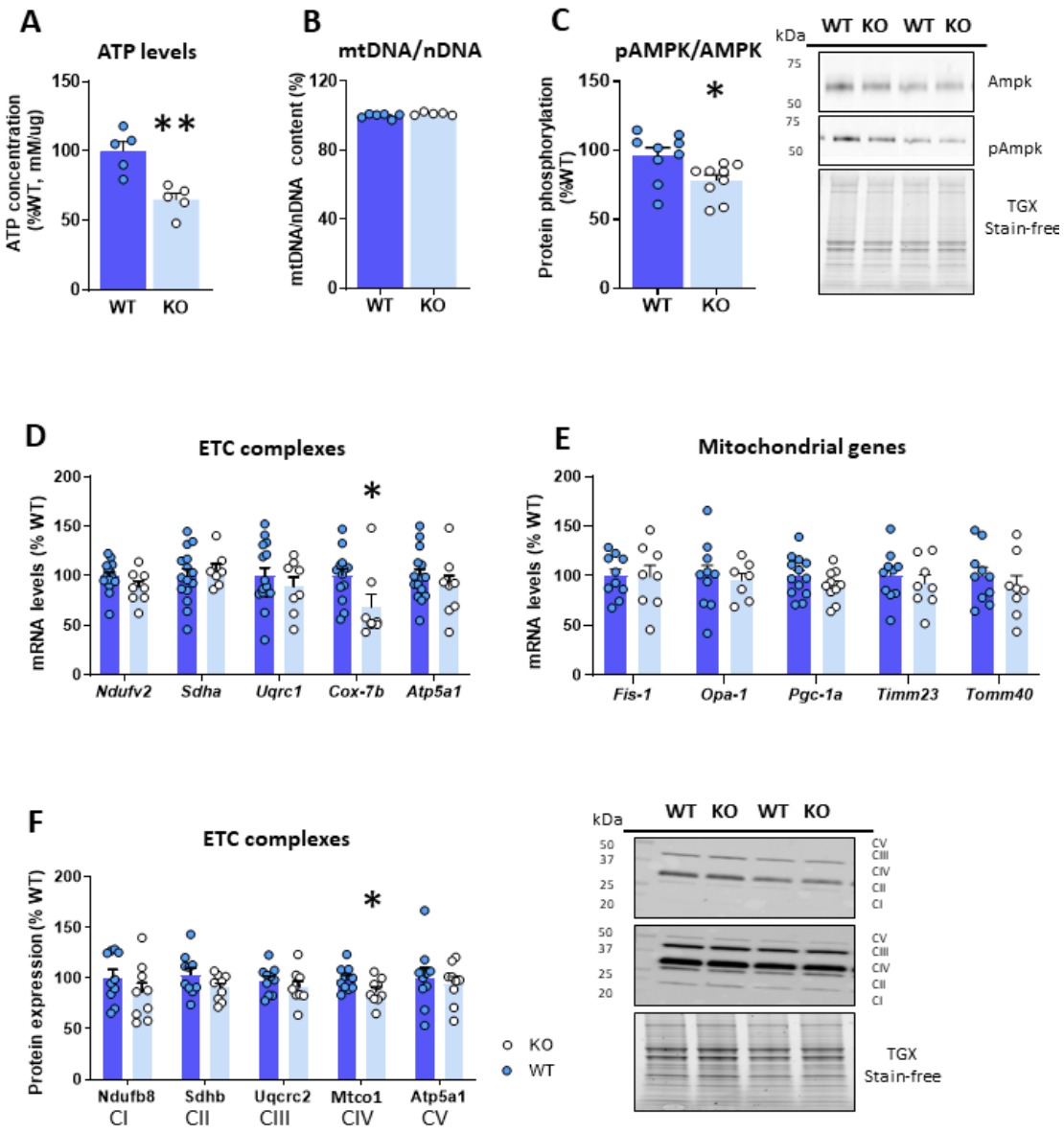

Figure 23. The *Cdkl5* KO hippocampus features strong impairment in AMPK activation and ETC complex IV levels. (A) CellTiter Glo luminescence assay unveiled a drastic decrease in ATP levels of *Cdkl5* KO (n = 5) hippocampus compared to WT littermates (n = 5). **(B)** qPCR analysis depicted with a scatter dot plot showed that the mtDNA/nDNA is not affected by *Cdkl5* loss. **(C)** Quantification of western blots revealed a defect in AMPK activation in the hippocampus of *Cdkl5* KO (n = 9) with respect to WT (n = 9). Values are reported as arbitrary units and data are expressed as percentage of WT. Right panels display a representative western blot of total AMPK and phosphorylated AMPK (pAMPK Thr172). Total protein content, visualized by TGX Stain-Free technology (Bio-Rad), was used for data normalization. **(D, E)** Transcriptional levels of the principal mitochondrial genes and OXPHOS complex subunits were analysed by quantitative RT-PCR in WT and KO hippocampi. Results displayed a consistent reduction of *Cox-7b*. *Hprt* was used as internal standard. **(F)** Protein expression levels of OXPHOS complex subunits. In *Cdkl5* KO a significant reduction of the complex IV was

confirmed (n = 10 WT, n = 9 KO). Right panel displays a representative western blot of the ETC complexes. Total protein content, visualized by TGX Stain-Free technology (Bio-Rad), was used for data normalization. Statistical significance was assessed by Student's t test or Mann-Whitney U test, in accordance with D'Agostino-Pearson test for data distribution; * $p < 0.05$ and ** $p < 0.01$. Data are expressed as percentage of WT and all graphs are presented as mean ± SEM.

6.2.2 Cdkl5 mitochondrial defect slightly affects thalamus but not cerebral cortex

Considering the aforementioned results, we continued using electron transport chain and pAMPK phosphorylation as molecular readouts of our study. The next step was to measure the presence and extent of the mitochondrial defect in other relevant brain regions for CDD. In accordance with data shown in Table 1 and Figure 21-22, we selected thalamus to parallel MRI results and molecular data. In addition, due to its relevance in CDD literature (Pizzo *et al*, 2016; Ren *et al*, 2019) and in line with MEMRI results, we added the cerebral cortex to the analysis.

Western blot analyses of respiratory complex subunits in *Cdkl5* KO mouse exhibited a drastic and selective decrement of Mtco1 levels in thalamus (-64.9 ± 9.0% compared to WT; Figure 24A), which strengthen results obtained in the hippocampus. No significant difference was observed in the other complexes' subunits. However, it is relevant to note that in this brain region the pAMPK/AMPK ratio did not present significant difference (-7.6 ± 6.7%; Figure 24B); accordingly, we measured comparable amounts of ATP among mutant and WT animals (-28.2 ± 18.0%). In the cerebral cortex the levels of the OXPHOS complex subunit remained comparable to WT values (Figure 24D). Importantly, we also observed unaffected levels of pAMPK phosphorylation (6.3 ± 9.6%; Figure 24E), in line with similar levels of ATP (12.4 ± 7.1%; Figure 24F). In conclusion, considering that thalamus resulted less affected than hippocampus, we decided to continue our studies on mitochondrial dysfunction in the *Cdkl5* KO brain focusing on hippocampus.

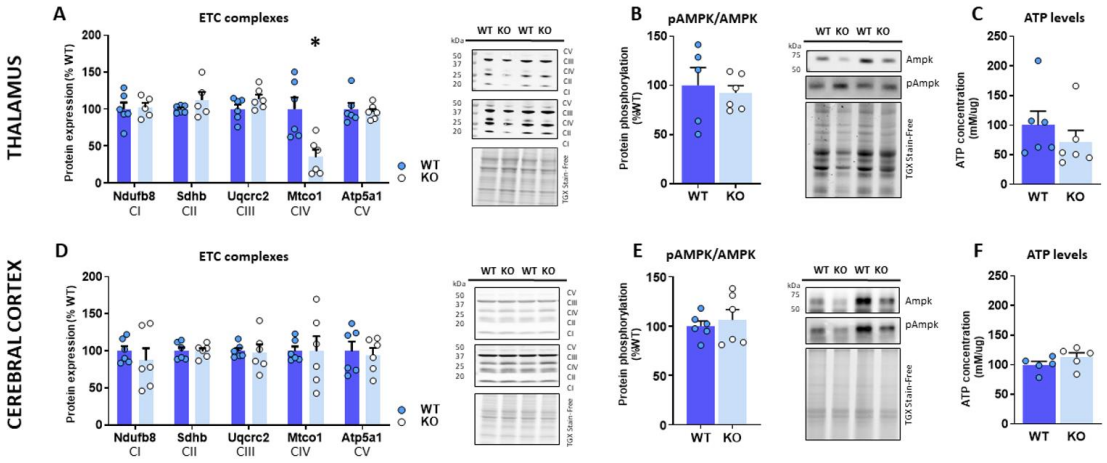

Figure 24. Mitochondrial impairment is slightly extended to *Cdkl5* KO thalamus (A, D) Protein expression levels of OXPHOS complex subunits in thalamus (A) and cerebral cortex (D). The *Cdkl5* null thalamus confirms a strong reduction of Mtco1 (n = 6 WT, n = 6 KO). Right panels display representative western blots of the ETC complexes. Total protein content, visualized by TGX Stain-Free technology (Bio-Rad), was used for data normalization. **(B, E)** Graphs show unaltered levels of pAMPK activation in both thalamus (B, n = 5 WT, n = 6 KO) and cerebral cortex (E, n = 6 WT, n = 6 KO). Right panels display representative western blots of the AMPK and its phosphorylated form (pAMPK (Thr172). Total protein content, visualized by TGX Stain-Free technology (Bio-Rad), was used for data normalization. **(C, F)** Scatter dot plots show analogous levels of ATP content in thalamus (C, n = 6 WT, n = 6 KO) and cerebral cortex (F, n = 5 WT, n = 5 KO) among WT and KO animals. Statistical significance was assessed by Student's t test or Mann-Whitney U test, in accordance with D'Agostino-Pearson test for data distribution; * $p < 0.05$. Data are expressed as percentage of WT and all graphs are presented as mean ± SEM.

6.2.3 A longitudinal study reveals that mitochondrial defects peak at P70

Given the central role of mitochondria in energy metabolism, the study of age-related mitochondrial impairments might help in disclosing the mechanism(s) leading to neurodevelopmental disorders. To better understand when the mitochondrial defect arises in the *Cdkl5* null hippocampus and how it progresses, we performed a longitudinal molecular analysis. In addition to the already analysed P70 (Figure 23), we thus selected an early time point, P10, and an intermediate time point, P40.

Western blot analyses of ETC complexes (Figure 25A,D) showed normal levels of all subunits at both ages, thus implying that the onset of complex IV defects occurs later. A trend toward an increase of AMPK activation (pAMPK; Figure 25B) was instead observed in KO hippocampi at P10 (18.8 ± 6.6%; $p = 0.0855$); in possible good accordance, a non-significant increment of the ATP content was observed in KO samples (71.9 ± 31.9%; Figure 25C). This apparent upregulation in ATP homeostasis disappeared at P40. In fact, no consistent deficiency was found at any levels of analysis

(pAMPK/AMPK ratio: 10.0 ± 6.3%; ATP: 8.1 ± 4.7%; Figure 25E and F). Of relevance, AMPK activation was in line with ATP levels at any point of analysis.

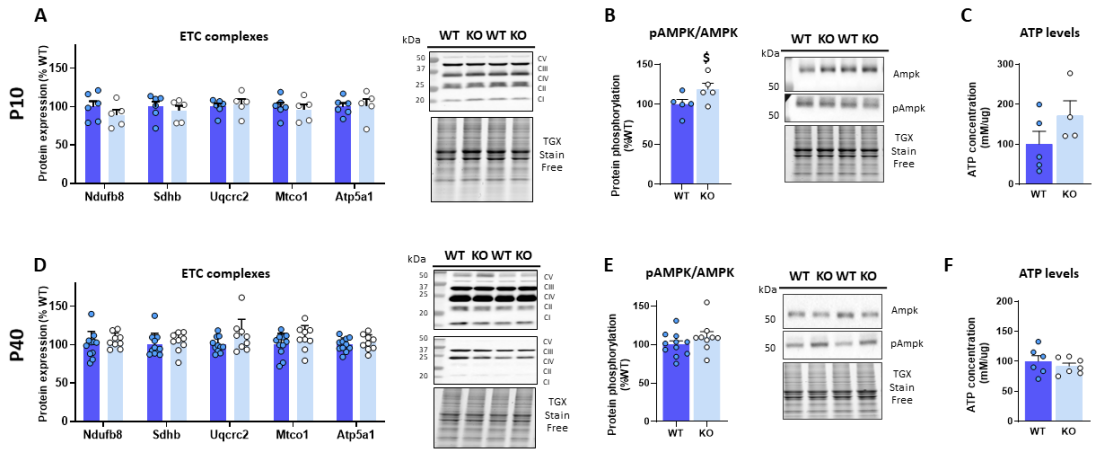

Figure 25. AMPK and ATP levels are not defective at early time points. (A, D) Scatter dot plots reveal comparable ETC levels between WT and KO at P10 (A) and P40 (D). Representative western blots of total OXPHOS are shown. Total protein content, visualized by TGX Stain-Free technology (Bio-Rad), was used for data normalization. **(B, E)** Graphs show the pAMPK/AMPK ratio at P10 (B) and P40 (E). Representative western blots of total AMPK and phosphorylated AMPK (pAMPK) are shown. Total protein content was used for data normalization. **(C, F)** CellTiter Glo luminescence assay unveils unaffected ATP levels in *Cdkl5* KO hippocampus both at P10 (C) and P40 (F). For all experiments the statistical significance was assessed by Student's t test or Mann-Whitney U test in accordance with data distribution; $ p = 0.0855. Data are expressed as percentage of WT and all graphs are presented as mean ± SEM.

These results prompted us to investigate whether at P70, in addition to defective complex IV levels, a functional defect in the electron transport chain was present. To explore it, we evaluated the mitochondrial respiratory capacity and O_2 consumption through High Resolution Respirometer (HRR), state-of-the-art methodology in mitochondrial research. Briefly, cryopreserved P70 hippocampi from KO and WT littermates were homogenate and were put in parallel chambers of Oroboros O_2k respirometer. Respiration was determined in an assay medium plus catalase (MiR06) that permits the reoxygenation of the chambers by catalase-mediated O_2 generation. The red (WT) and blue (KO) lines shown in Figure 26A represent the oxygen fluxes and indicate the volume of oxygen converted by the tissues per time per mg of tissue (pmol/s/mg of tissue).

HRR monitors the passage of the electrons from complex I to IV and the resultant synthesis of ATP from ADP and phosphate in complex V (ATP synthase). As a

consequence, the assay permits characterizing the behaviour of N- and S-linked pathways (NADH-dependent via respiratory complex I and succinate-dependent via respiratory complex II) of the mitochondrial ETC in a substrate-dependent manner. Non-phosphorylating respiration (state 2) is induced by adding the CI-linked substrates pyruvate and malate. Afterwards, the addition of saturating concentrations of ADP gives indication about the OXPHOS capacity of CI-linked activity (state 3). The OXPHOS capacity with combined CI and CII-linked substrates (state 3+S) is evaluated by the addition of succinate. Addition of the uncoupler FCCP increases the H^+ leak across the inner membrane and by a selective inhibitor of CI (rotenone) the measurement of the CII-linked activity (state 3+S+Rot) is provided. Eventually, CII and CII are stopped through the addition of antimycin A and malonic acid and mitochondrial CIV is activated by TMPD, the artificial substrate able to reduce cytochrome c in the presence of ascorbate (Figure 26B).

Figure 26C shows that respiration driven by NADH-linked (pyruvate/malate) or $FADH_2$-linked (succinate) substrates is not affected in *Cdkl5* null hippocampi. Accordingly, we noticed that the maximal respiratory capacity of the electron transport chain is not impaired in KO samples, although a slight trend toward reduced O_2 flux was observed in CII functionality after the addition of rotenone (-4.9 ± 2.3%; p value = 0.0990). Interestingly, by adding complex IV specific substrates we detected a significant deregulation (-11.5 ± 2.4%), thus reinforcing our data indicating that mitochondrial respiratory activity of complex IV is compromised in the P70 *Cdkl5* null hippocampus.

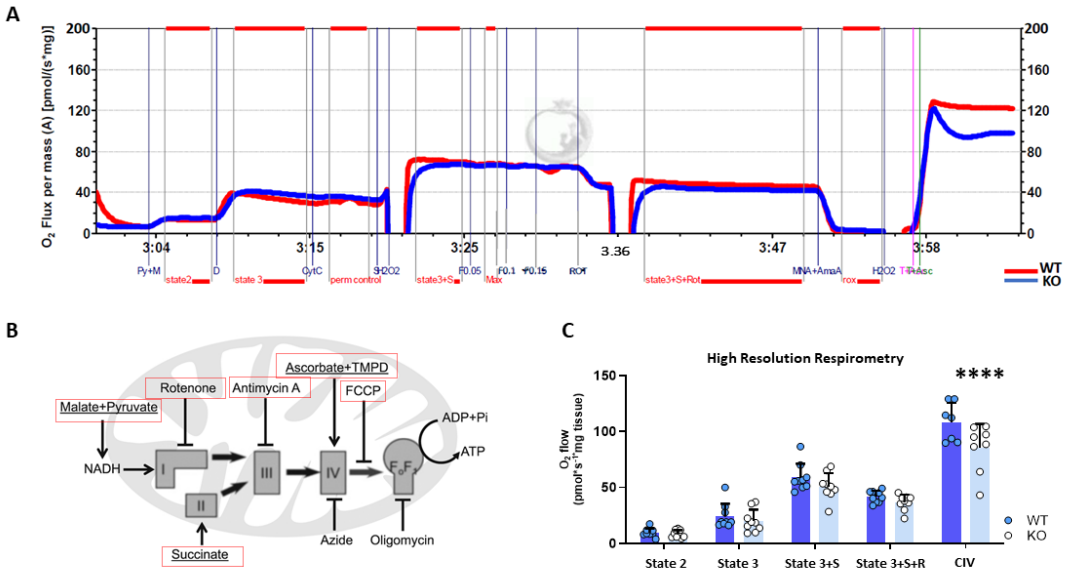

Figure 26. High Resolution Respirometry confirms defective activity of complex IV at P70. (A) Representative respirometry traces of WT (red line, n = 9) and KO (blue line, n = 9) hippocampi. CytC: cytochrome c; F: FCCP; Py+M: pyruvate+malate; ROT: rotenone; MNA+AmaA: malonic acid+antimycin A; T+Asc: TMDP+ascorbate. **(B)** Schematic representation of the substrates and inhibitors that can be used in the assay (adapted from Long *et al*, 2019). Dotted lines highlight substrates used in our protocol. **(C)** Graph shows $\dot{V}O_2$ resulting from the activity of the electron transport chain complexes. KO samples show significant impaired activity of complex IV. Statistical significance was assessed by Multiple t test; **** p <0.0001. Graph is presented as mean ± SEM.

6.2.4 The administration of Metformin rescues some behavioural phenotypes of the Cdkl5 KO mouse

We proceeded testing whether a pharmacological treatment targeting the observed defects in AMPK activation could have beneficial effects. In recent years, it emerged that the dimethylbiguanide Metformin can recover brain defects in mitochondrial homeostasis and ATP shortage. Indeed, although Metformin is a first line FDA-approved drug for the treatment of type 2 diabetes mellitus (Hundal *et al*, 2000; Hotta, 2019), it was recently proved that it also exerts off-target effects on mitochondrial functions (Martin-Montalvo *et al*, 2013; Zuliani *et al*, 2020; Peralta *et al*, 2020). In addition, Metformin was recently used in a mouse model of Rett syndrome, where it rescued brain mitochondrial alterations, such as decreased ATP levels and defective protein expression of electron transport chain complexes (Zuliani *et al*, 2020). Consequently, we elegised Metformin for our treatment. In accordance with previous findings that addressed its effectiveness, we selected a 100mg/kg dose, which is reported to give analogous drug plasma concentration to those

normally used in type-2 diabetes patients (~20 mg/kg)(Howell *et al*, 2017; Zhou *et al*, 2016).

We started the pharmacological administration at a pre-symptomatic time point (P55) and we performed a 20 days treatment in *Cdkl5* KO animals and corresponding controls (100 mg/kg, once a day; i.p.)(Figure 27A). To obtain a solid baseline of the behavioural phenotype, animals underwent a battery of tests at P50, which was then repeated after 10 and 20 days from the start of the pharmacological treatment. Moreover, a small group of mice was also tested 10 days after the last injection to examine the possible long-term effect of Metformin (Figure 27A).

Marble test was selected since it is regularly used for the categorisation of autism-related behaviour and general environment interest (Thomas *et al*, 2009). Furthermore, Open field test was useful to investigate the locomotor and exploratory activity of mice, while Novel Object Recognition (NOR) test allowed us to investigate mice memory when a novel object was introduced in a familiar environment, by measuring the time spent interacting with the novel object with respect to the familiar one (discrimination index). Importantly, NOR was the only test performed in a different cohort of mice, to avoid that the animals recall objects previously seen.

Cdkl5 KO mice manifested altered behaviour in all tests. In Marble test WT animals buried a large number of marbles (10.1 ± 0.3), while *Cdkl5* KO mice manifested low interest in digging and burying them (7.2 ± 0.5), thus indicating a failure in the accomplishment of innate behavioural patterns (Figure 27B). Moreover, we observed that KO animals travelled significantly longer distances with respect to their WT littermates in Open field test, revealing elevated locomotor activity (WT: 5246 ± 422.6; KO: 6863 ± 379.3)(Figure 27C). Eventually, in the Novel Object Recognition familiarization phase WT and KO showed no difference (WT: 0.06 ± 0.05; KO: -0.04 ± 0.07). However, when four hours later a familiar object was substituted with a novel one the discrimination index of WT mice was significantly larger compared to KO (WT: 0.18 ± 0.07; KO: 0.02 ± 0.08)(Figure 27D).

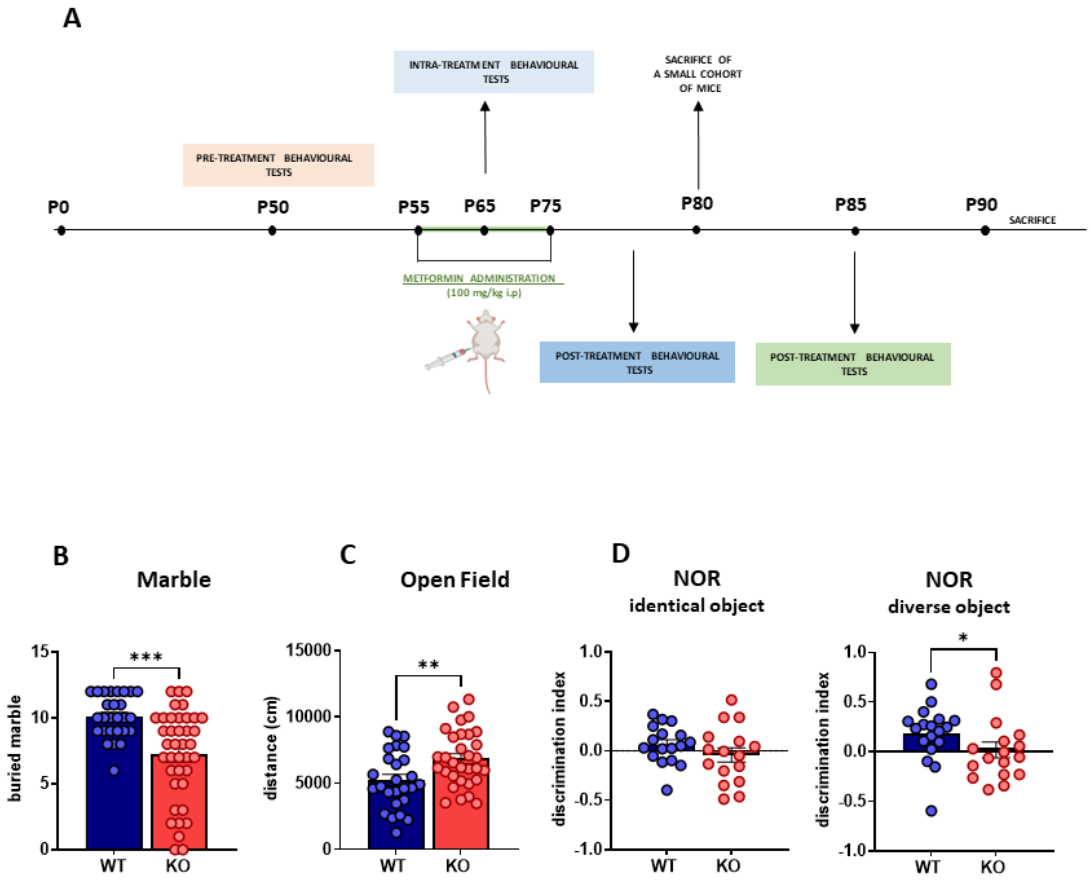

Figure 27. Metformin treatment aims to rescue behavioural phenotypes related to *Cdkl5* deficiency. (A) Graphical representation of the treatment experimental schedule. **(B)** Graph shows that KO animals bury a significantly low number of marbles compared to WT. **(C)** Scatter dot plot features the distance travelled by mice in the open-field arena, highlighting an increased locomotor activity in KO mice. **(C)** Discrimination index of time spent exploring the two identical objects during the familiarization phase shows no difference between WT and KO, while a robust preference for the novel object was observed in WT mice during the test phase. Statistical significance was assessed by Student's t test or Mann-Whitney U test in accordance to data distribution; * p <0.05; ** p <0.01; *** p<0.001. All graphs are presented as mean ± SEM.

To assess whether the Metformin treatment could rescue the observed phenotypes of *Cdkl5* KO animals, a new battery of behavioural tests was carried out the 10th days of the drug administration. Interestingly, Metformin treatment significantly increased the marble-burying behaviour in *Cdkl5* KO-treated animals (WT: 8.9 ± 0.4; KO: 5.7 ± 0.9; KO-treated: 9.1 ± 0.2)(Figure 28A), thus revealing that Metformin prompted the interest for the environment in mutant animals. Locomotor performance was investigated in the Open field and we confirmed the presence of a defect between WT and KO animals (WT: 5035 ± 342.8; KO: 7394 ± 590.6), which was ameliorated by Metformin treatment (KO-

treated: 6779 ± 617.1)(Figure 28B). Then, learning and memory were assessed through the NOR test. In the familiarization phase all groups spent equal time exploring the two identical objects, however when the novel object was presented to mice the high variability did not allow to confirm the presence of a statistical difference between WT and KO. On the same line, no effect was observed in treated animals (Figure 28C).

Animals were tested again at the end of the treatment (20th day of the schedule). From now on, due to the limited number of mice, we decided to eliminate the WT treated experimental group, since previous tests revealed comparable behaviours among WT treated and untreated animals. Importantly, both the Marble and the Open field tests revealed a trend of the KO treated animals towards amelioration, although no statistical significance was achieved (Marble test - WT: 8.8 ± 2.3; KO: 5.4 ± 2.4; KO-treated: 7.1 ± 1.0; Open field - WT: 5466 ± 214.0; KO: 7813 ± 1101.0; KO-treated: 6942 ± 840.1)(Figure 28D,E). In line with previous results, no change in the discrimination index was observed in saline- or metformin-treated animals (Figure 28F). Considering the encouraging results, to define the benefits of a chronic administration of Metformin, a novel pharmacological treatment on additional animals is currently ongoing.

Eventually, to investigate whether Metformin could exert beneficial long-term effects, behavioural tests were performed 10 days after the end of the treatment (30th day of the experimental schedule).

Interestingly, a slight positive effect could be still observed in the Marble test. In fact, the statistical difference between WT and KO mice *(*WT: 10.3 ± 0.6; KO: 7.3 ± 1.0) disappeared in the WT and KO-treated comparison *(*KO-treated: 7.9 ± 0.7)(Figure 28F). Similarly, the Open field test confirmed that KO animals travel higher distances *(*WT: 3840 ± 487.4; KO: 5163 ± 261.4*)* but the defect was less prominent in treated animals *(*KO-treated: 4812 ± 503.1*)(*Figure 28G*)*. On the contrary we did not reveal any improvement in the NOR test (Figure 28H).

Our results suggest that Metformin treatment improves some typical behavioural deficit of *Cdkl5* KO mice, such as poor interest for the environment and locomotor hyperactivity, that however do not strongly persist after treatment.

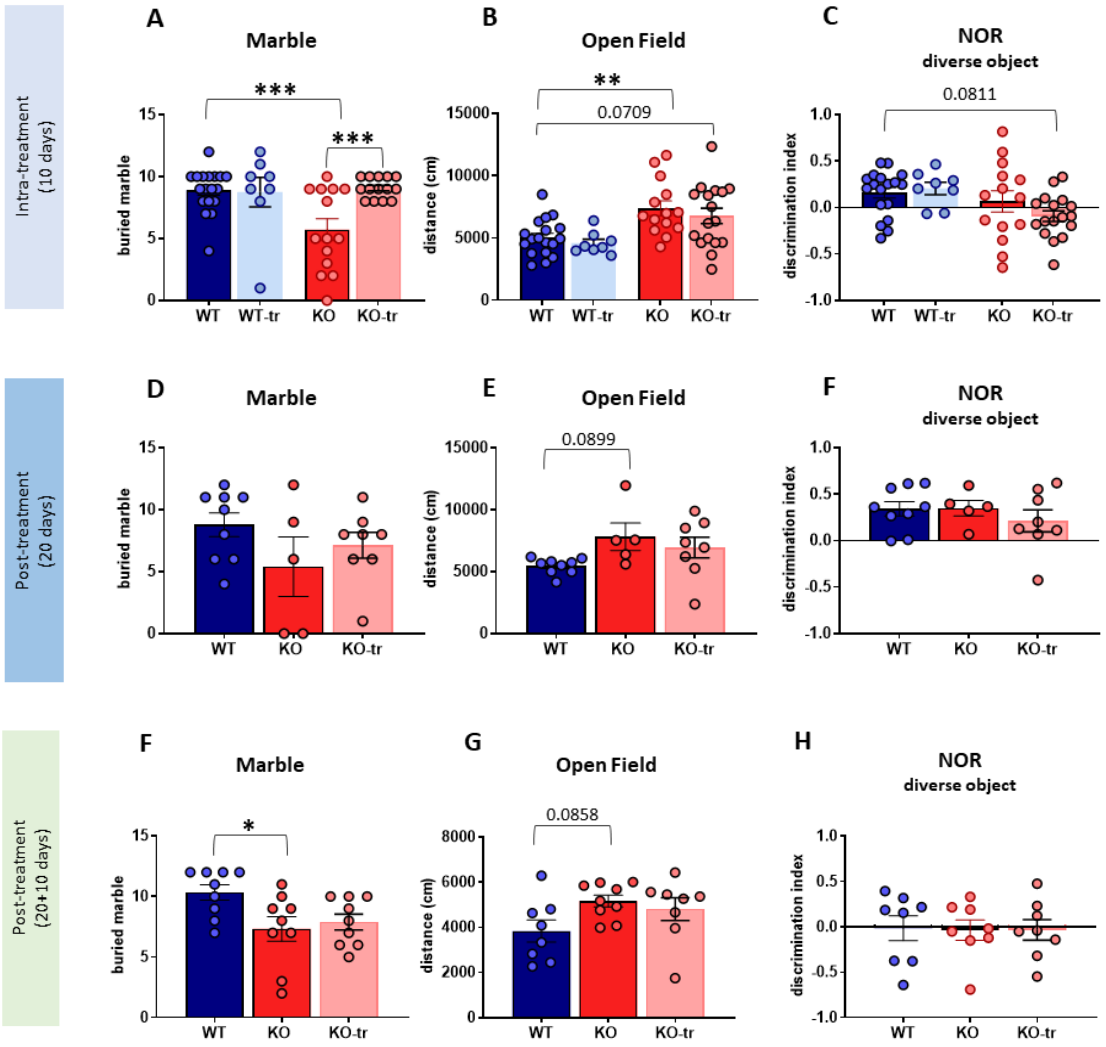

Figure 28. *Cdkl5* KO mice benefit from a Metformin treatment. (A-C) Graphs show behavioural results after 10 days of Metformin administration, thus revealing a positive effect in Marble (A) and Open field (B) tests, but not in NOR (C). **(D-F)** Graphs indicate that 20 days of Metformin treatment leads to a different trend between KO and KO-treated mice, especially in total distance travelled in the Open field test (E). **(F-H)** Graphs depict the effects of Metformin 10 days after treatment tested through Marble test (F), Open Field (G) and NOR test (H). No difference among groups were observed in the discrimination index in the NOR test. Statistical significance was assessed by Two-way ANOVA (A-C) or One-way ANOVA (D-H), both followed by Tukey post-hoc, * p <0.05; ** p <0.01; *** p<0.001. All graphs are presented as mean ± SEM.

6.2.5 Molecular analyses confirm that Metformin treatment exacerbates pAMPK impairment in the Cdkl5 KO hippocampus

To investigate whether Metformin could reach the hippocampus thereby modulating AMPK levels, a cohort of animals was sacrificed immediately after the 20 days treatment.

Hippocampi were lysed and sub-fractionated into mitochondria- and cytosol-containing fractions. Indeed, it was recently reported that a fraction of AMPK, named as mitoAMPK, is present on the outer mitochondrial membrane where it plays a role in mitochondrial quality control. Further, it may act as an energetic signal, particularly when ATP production through OXPHOS is limited (Zhao *et al*, 2019; Drake *et al*, 2021). Thus, we considered it relevant to explore whether Metformin could activate cytosolic and/or mitoAMPK.

Cytosolic and mitochondrial fractions derived from *Cdkl5* WT, KO and KO-treated mice were analysed through Western Blots. Cytoplasmic pAMPK levels and pAMPK/AMPK ratio appeared increased in WT hippocampi with respect to KO, thus confirming our previous results (pAMPK: +26.6 ± 6.0% compared to KO; pAMPK/AMPK ratio: +30.8 ± 12.8%)(Figure 29A-B). However, this difference was abolished when WT animals were compared to KO-treated mice, therefore proving its expected activity. On the contrary, phosphorylated mitoAMPK did not differ among genotypes and no effect was exerted by Metformin (WT: 100.0 ± 4.4%; KO: 93.6 ± 4.9%; KO-treated: 91.4 ± 2.9%)(Figure 29D-E).

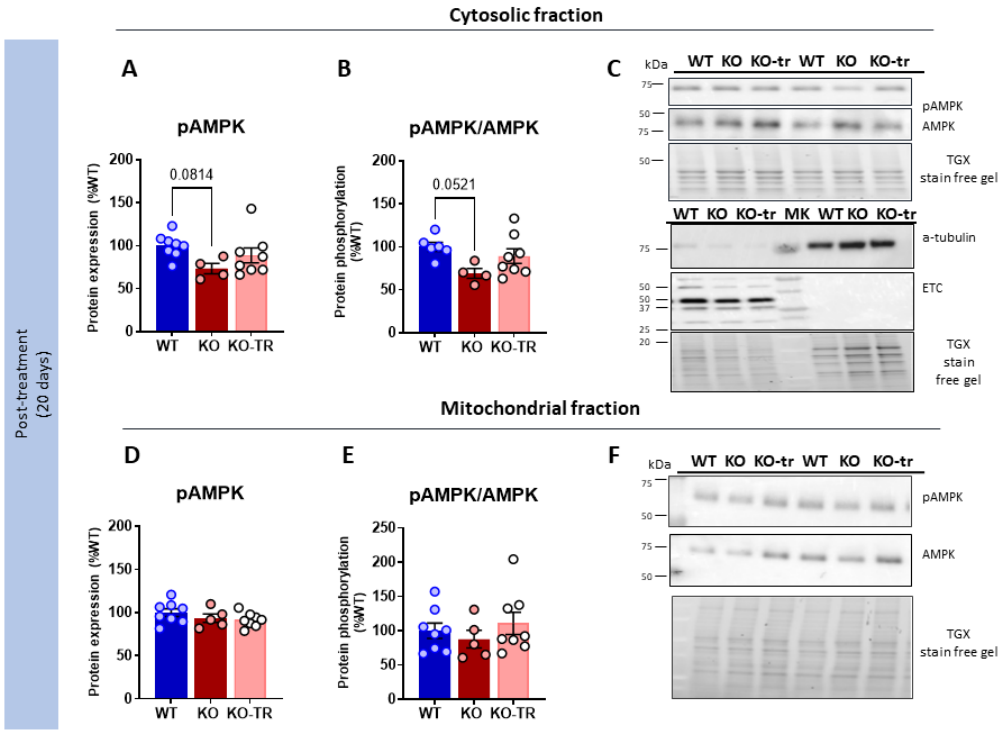

Figure 29. Metformin activates AMPK phosphorylation in *Cdkl5* KO hippocampi. (A-C) Graphs show pAMPK (A) and pAMPK/AMPK ratio (B) in the cytoplasmic fraction. The genotype difference observed among WT and KO is no longer present when WT is compared to KO-treated hippocampi. A KO animal was excluded from the analysis since it was recognized as an outlier. (C) Representative western blots of total AMPK and phosphorylated AMPK (pAMPK) are shown, together with a-tubulin and total OXPHOS to confirm the successful fractionation. Total protein content was used for data normalization. **(D-E)** Graphs reveal unaltered pAMPK levels (D) and pAMPK/AMPK ratio (E) among groups in the mitochondrial fraction. (F) Representative western blots of total AMPK and phosphorylated AMPK (pAMPK) are shown. Total protein content was used for data normalization. Statistical significance was assessed by One-way ANOVA, followed by Tukey post-hoc. All graphs are presented as mean ± SEM.

Similar results, although reduced in entity, were observed 10 days after the end of Metformin administration (30^{th} day of the schedule)(Figure 30). In fact, a significant downregulation of pAMPK was selectively observed only in the cytoplasmic fraction of untreated KO hippocampi (WT: 100.0 ± 14.2%; KO: 84.3 ± 9.6%; KO-treated: 63.2 ± 5.5%).

All in all, molecular analyses confirmed that Metformin reaches the hippocampus but it exerts its effect only on cytosolic AMPK. Considering that AMPK is a crucial sensor hub of the cells involved in several pathways, in the future we will investigate whether different molecular pathways modulated by AMPK could be affected by the treatment.

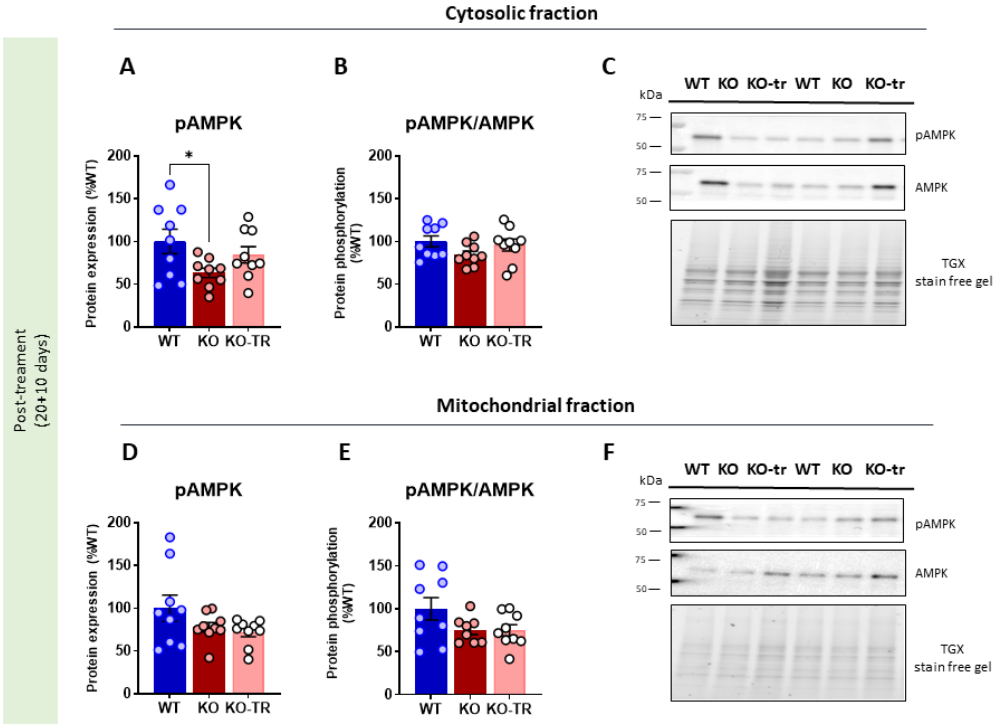

Figure 30. Metformin has no stronger long-term effect 10 days after the end of the treatment. (A-C) Graphs show pAMPK (A) and pAMPK/AMPK ratio (B) in the cytoplasmic fraction, thus revealing Metformin modulation on pAMPK levels. (C) Representative western blots of total AMPK and phosphorylated AMPK (pAMPK) are shown. Total protein content was used for data normalization. **(D-E)** Graphs depict unaffected pAMPK levels (D) and pAMPK/AMPK ratio (E) in the mitochondrial fraction. (F) Representative western blots of total AMPK and phosphorylated AMPK (pAMPK) are shown. Total protein content was used for data normalization. Statistical significance was assessed by One-way ANOVA, followed by Tukey post-hoc, * $p < 0.05$. All graphs are presented as mean ± SEM.

6.3 Longitudinal MRI studies provide indications of different disease progression accordingly to *Mecp2* deficiency and gender

6.3.1 Mecp2 loss or mutation deeply affects total brain volume

MRI provided interesting functional indications for the *Cdkl5* null brain; we thus decided to extend this approach also to *Mecp2* deficient mouse models. Recently, we have demonstrated that *Mecp2*-null and *Mecp2*-Y120D mice have similar behavioural phenotypes, but discordant molecular features (i.e. overall chromatin compaction, recruitment of co-repressor complexes on heterocromatic DNA and transcriptional activity)(Gandaglia *et al*, 2019). We proposed the importance of characterizing discrepancy and common features among mice carrying various *Mecp2* mutations, in

order to understand whether personalized medicine should be considered for RTT. For these reasons, we studied and compared *Mecp2* KO and KI brains of both genders in a longitudinal MRI study.

Initially, by MRI we performed an *ex vivo* morphological analysis in a fully symptomatic age, corresponding to P40 for males and P150 for females. No difference in body weight was found between experimental groups (Figure 31A). After fixation, brains were weighted and a general decrease in total brain weight was noticed in mutant animals (male *Mecp2*$^{-/y}$: -11.3 ± 1.7%; female *Mecp2*$^{-/+}$: -9.6 ± 2.4%; male *Mecp2*$^{Y120D/y}$: -10.4 ± 2.4%; females *Mecp2*$^{Y120D/+}$: -13.2 ± 1.2%) (Figure 31B). Thereafter, brains were MR scanned and virtually segmented in rostral to caudal slices; the cerebral area of each section was manually measured to obtain the total brain volume. We unveiled that *Mecp2* loss or mutation deeply affects cerebral size with a consistent volume reduction along the whole mutant brain (Figure 31C-H). In fact, a significant volume decrease with respect to WT was found in *Mecp2*$^{-/y}$ (-13.4 ± 2.0%), *Mecp2*$^{-/+}$ (-10.5 ± 1.3%) and *Mecp2*$^{Y120D/+}$ (-7.0 ± 0.9%). A trend towards reduction was also observed in *Mecp2*$^{Y120D/y}$ (-10.8 ± 4.1%) male mice that however did not reach statistical significance most likely due to the higher variability.

In addition, and in line with the experimental setup used in *Cdkl5* animals, we tested whether *ex vivo* Manganese Chloride MRI could permit identifying in which cerebral regions the loss or mutation of *Mecp2* has a major impact on brain function. However, unexpectedly, we were not able to reach a significant difference in the analysed brain regions, probably due to the high variability and to the small cohort of animals.

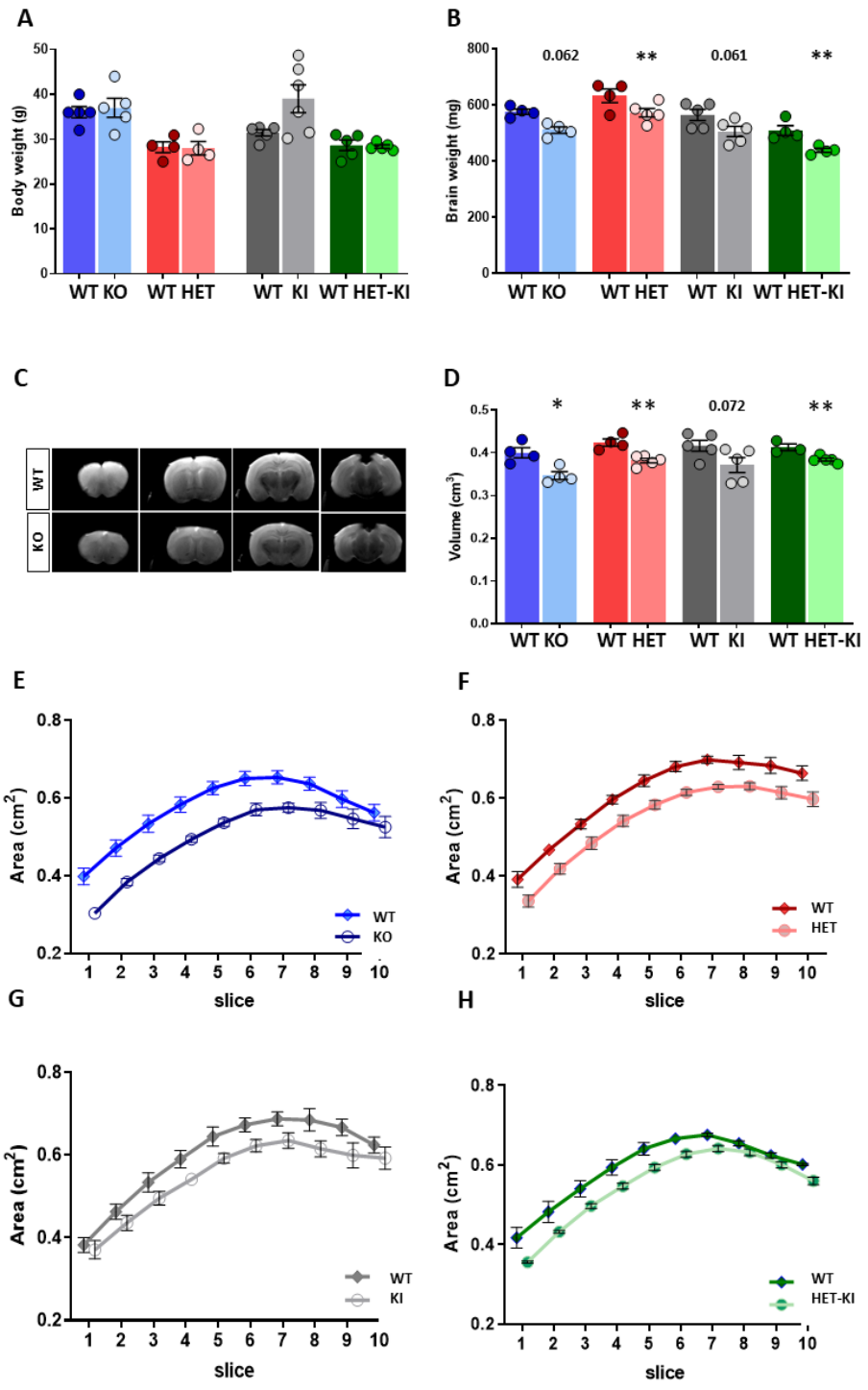

Figure 31. **Microcephaly appears consistent throughout the brain of *Mecp2* mutant mice**. **(A)** No difference was found in body weight (g) of *Mecp2*-null and -Y120D compared to controls. **(B)** Brain weight (mg) is deeply affected by *Mecp2* mutations in all the experimental groups. Each mutant mouse was evaluated in comparison to WT littermates. **(C)** Representative T2 weighted MR slice images from a *Mecp2* WT and a KO brain. **(B)** Scatter dot plots show a significant cerebral volume (cm^3) reduction in both *Mecp2*-null and *Mecp2*-Y120D animals. **(E-H)** *Ex vivo*

MRI of null (E-F, n: male WT = 4, KO = 4; females WT = 4, HET = 5) and Y120D animals (G-H, n: male WT = 5, KI = 5; females WT = 3, HET-KI =5) displayed reduced volume in almost all the analysed brain sections. Mutant mice were evaluated in comparison to WT littermates by Student's t-test or Mann-Whitney in accordance with data distribution. * p value < 0.05; ** p value < 0.01.

Thus, we proceeded with a longitudinal analysis by *in vivo* MRI that should permit a comprehensive structural analysis of the brain overtime and to overcome technical limits of the *ex vivo* setting. For instance, the brain volume could have been altered by paraformaldehyde (PFA) fixation and ventricles collapse might have contributed to the relative volume shrinkage. In addition, some cerebral regions, as the olfactory bulb and cerebellum, had been partially damaged during brain dissection, thus impeding their measurement.

To this purpose, we used an advanced neuroimaging tool (ANTx2, open-source software) that allows automatic segmentation for quantitative morphometric analysis (Koch *et al*, 2019). We scanned and followed animals from a generally defined "pre-symptomatic time point", in which behavioural defects are not yet well-overt, corresponding to P20 for males and P60 for females, to a barely-symptomatic time point (P30 for males and P90 for females) and a fully-symptomatic time point (P40 for males and P200 for females).

Interestingly, mixed-effect model analysis of the longitudinal MRI revealed a strong effect for both age and genotype and confirmed a widespread volume reduction of the brain in all mutant animals that from now on we will call atrophy, however without alluding to neuronal death (Table 3 and Figure 32). In particular atrophy was already observed at P20, when symptoms are not yet overt (KO P20: -4.9 ± 1.1% compared to WT; KI P20 -5.9 ±1.5%)(Figure 32A,C) and become significantly different at P30, independently from the genotype (KO P30: -8.5 ± 1.4%; P40: -10.1 ± 1.0%; KI P30 -11.0 ± 2.2%; P40 -11.6 ± 2.0%). Interestingly, atrophy was always observed in female mutant animals. In fact, a smaller size of heterozygous female brains was evident since pre-symptomatic time points (HET P60: -6.8 ± 0.8%; HET-KI P60: -7.2 ± 1.8%)(Figure 32B,C) and the defect worsened at P200 (HET P200: -12.7 ± 2.0%; HET-KI P200: -12.7 ± 1.0%).

To clarify how the RTT brains develop along time, we measured in what manner the cerebral volume of each animal changed in comparison to their first time point of analysis (P20 for males and P60 for females). Remarkably, mutant males of both genotypes showed a growth trajectory similar to their WT littermates, that, however, became significantly divergent from WT at the last point of the analysis (Figure 32E,G). Conversely, whereas WT brains maintained the same volume (measured at P60) overtime, mutant female brains presented a different trend. In fact, *Mecp2*$^{+/-}$ heterozygous females displayed a tendency towards a progressive reduction of the brain volume (Figure 32F), while the HET-KI brain volume appeared constant through time (Figure 32H).

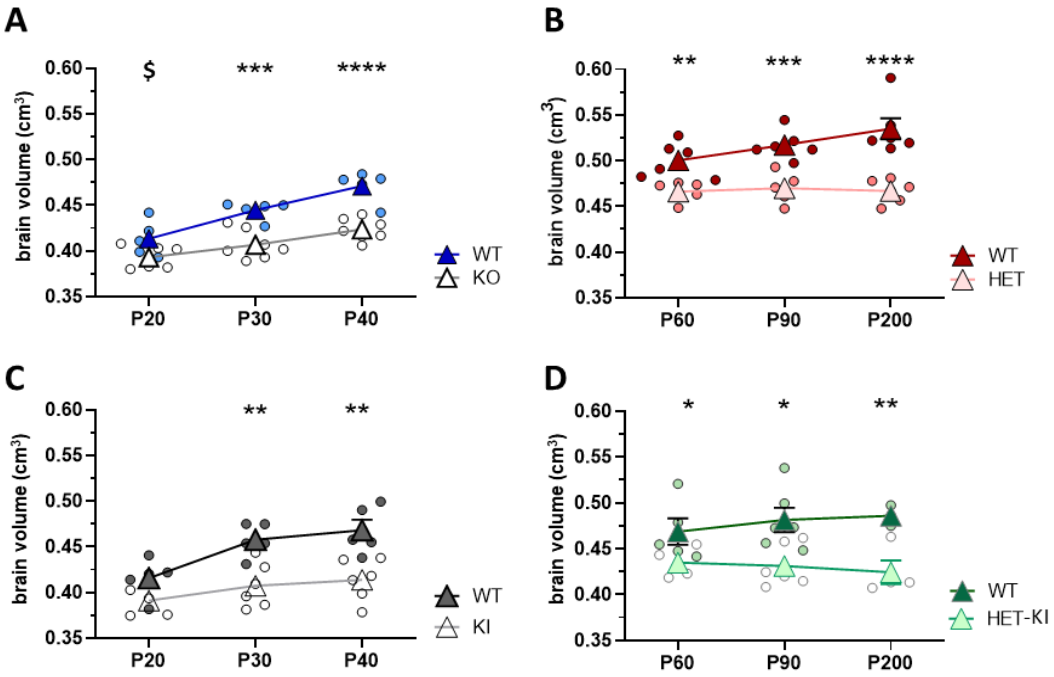

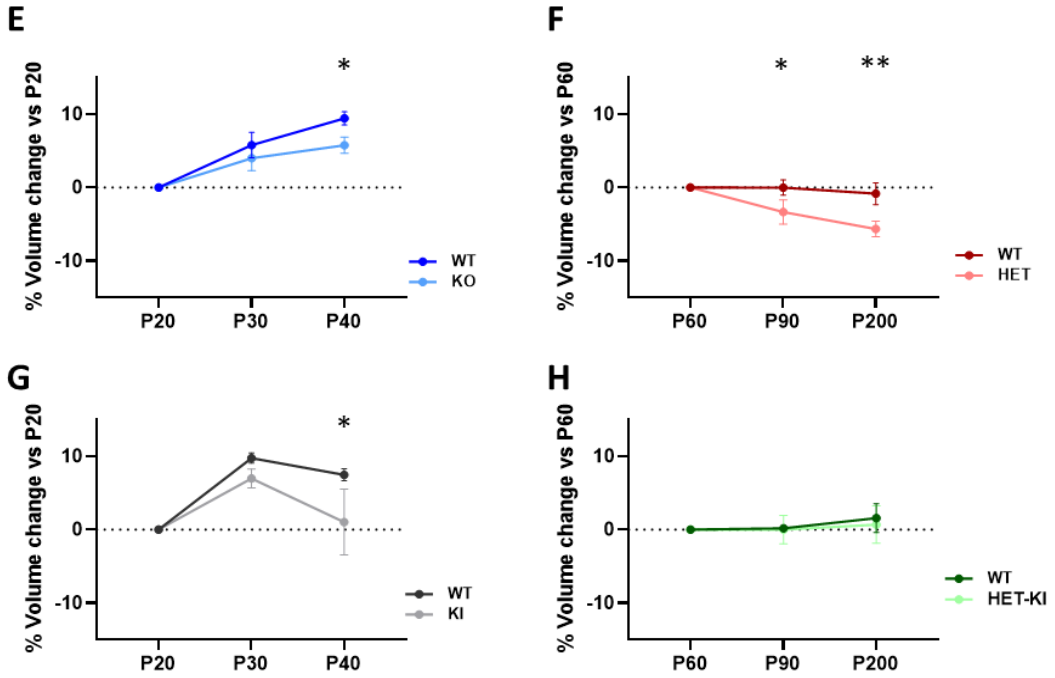

Figure 32. ***Mecp2* mutant animals experience persistent brain volume atrophy**. *In vivo* longitudinal MRI showed a significant reduction in the total brain volume (cm^3) of *Mecp2*-null **(A-B)** and *Mecp2*-Y120D **(C-D)** animals of both genders. Male mice (white for *Mecp2*-null and *Mecp2*-Y120D) unveiled a significant defect since P30. Females (pink for *Mecp2*-null, light green for *Mecp2*-Y120D) showed a significant reduction of the brain volume at any time point of analysis. **(E-H)** Graphs show how the mouse brain develops in comparison to the first time point of analysis in *Mecp2*-null and *Mecp2*-Y120D animals of both genders. Male mutant animals of null (E) and Y120D (G) line showed a similar but underdeveloped growth trajectory compared to WT. Females from the null line (F) presented a progressive cerebral atrophy, while Y120D females (H) have brain development trajectory comparable to WT littermates. Null mouse line: male WT, n = 5; KO, n = 7; female WT, n = 6; HET, n = 6. Y120D mouse line: male WT, n = 5; KI, n = 6; female WT, n = 6; HET-KI, n = 6. Animals whose fitting in the segmentation was not optimal were excluded from the analysis. Each mutant mouse was evaluated in comparison to their WT littermates by Two-way repeated measures ANOVA or Mixed-Model Analysis, followed by Sidak post-hoc (A-D) or Fisher's LSD post-hoc (E-H); * p value < 0.05; ** p value < 0.01; *** p value < 0.001; **** p value < 0.0001.

Table 3: Comparison of total brain volume (cm^3) between mutant mice and their corresponding WT littermates

Gender	Null mouse line			Y120D mouse line		
Male	**WT**	**KO**	**p value**	**WT**	**KI**	**p value**
P20	0,413 ± 0,009	0,393 ± 0,005	0.0876	0,416 ± 0,010	0,391 ± 0,007	0.1061
P30	0,445 ± 0,004	0,407 ± 0,006	**0.0004**	0,458 ± 0,008	0,407 ± 0,010	**0.0027**
P40	0,471 ± 0,008	0,424 ± 0,004	**<0.0001**	0,468 ± 0,012	0,414 ± 0,009	**0.0013**
Female	**WT**	**HET**	**p value**	**WT**	**HET-KI**	**p value**

P60	0,500 ± 0,008	0,466 ± 0,004	**0.0083**	0,469 ± 0,014	0,435 ± 0,009	**0.0279**
P90	0,517 ± 0,006	0,470 ± 0,008	**0.0005**	0,481 ± 0,013	0,431 ± 0,009	**0.0121**
P200	0,535 ± 0,012	0,467 ± 0,005	**<0.0001**	0,486 ± 0,006	0,424 ± 0,013	**0.0027**

Two-way repeated measures ANOVA (or Mixed model), Sidak post-hoc, were used for statistical analysis; Null mouse line: WT, n = 5; KO, n = 7; female WT, n = 6; HET, n = 6. Y120D mouse line: male WT, n = 5; KI, n = 6; female WT, n = 6; HET-KI, n = 6. In some cases, the automatic segmentation was not optimal thus the MRI data were excluded from the analysis (n = 1 KO at P20; n = 1 HET-BIRD at P90; n= 1 HET-KI at P200).

In summary, MRI morphological analyses revealed a consistent effect of *Mecp2* deficiency on the overall cerebral volume which, therefore, could be considered a solid "benchmark" of the disease.

6.3.2 Mecp2 deficient mouse brains exhibit different regional phenotypes depending on sex and genotype

Based on the solid results obtained with the morphological analysis we further exploited the potential of atlas-based whole brain segmentation with ANTx2 (Koch *et al*, 2019) to identify if and which brain regions are mainly affected. This unbiased approach allowed us to delineate a large number of brain structures (825-835 areas) from the T2-weighted MRI images confirming previous findings and, in particular, the influence of genotype and gender on the progression of the disease.

We divided the analysis in order to answer three major questions: how different portions of the brain evolve along time; to what extent a specific brain region contributes to the general brain atrophy depicted in Figure 32; what is the regional developmental trajectory of the most relevant cerebral area.

First, we followed the development of specific brain structures overtime (a detailed overview could be found in Tables 4 and 5, a synthesis is provided in Figures 33-36). Summarizing, cerebral cortex, hippocampus and brainstem appeared as the most atrophic/underdeveloped regions of male mutant animals (Table 4). In particular, prefrontal, visual, somatomotor and somatosensorial portions of the cerebral cortex mainly contributed to the atrophy in KI males, while entorhinal and somatosensorial cortices are responsible for that in KO. A similar volumetric decrease was observed in the whole hippocampal formation of both genotypes, with a strong impact from CA1 and

CA3. Additionally, the brainstem shrinkage principally depended on midbrain and pons in KI, and selectively from the pons in KO.

Table 4: Regional cerebral volume difference (%) of *Mecp2*$^{-/y}$ and *Mecp2*$^{Y120D/y}$ compared to WT littermates

Anatomical Region	BIRD %difference to WT (Mean ± SEM) [p value]			Y120D %difference to WT (Mean ± SEM) [p value]		
	P20	P30	P40	P20	P30	P40
Cerebrum regions						
Cerebrum	-5.2 ± 0.8 [0.2426]	-8.4 ± 1.8 [**0.0041**]	-10.6 ± 1.5 [**0.0002**]	-8.1 ± 2.4 [0.0736]	-11.8 ± 2.2 [**0.0022**]	-12.6 ± 1.9 [**0.0009**]
Cerebral cortex	-5.1 ± 0.9 [0.3767]	-8.5 ± 2.1 [**0.0088**]	-10.4 ± 1.7 [**0.0007**]	-8.4 ± 2.5 [0.0713]	-12.5 ± 2.2 [**0.0018**]	-13.6 ± 1.9 [**0.0005**]
Prefrontal cortex	-6.4 ± 2.9 [0.6433]	-8.6 ± 2.6 [0.2388]	-8.3 ± 2.8 [0.2797]	-12.9 ± 3.6 [0.0591]	-14.9 ± 3.7 [**0.0096**]	-17.4 ± 2.2 [**0.0027**]
Entorhinal cortex	-7.8 ± 2.1 [0.2351]	-11.5 ± 2.5 [**0.0232**]	-14.5 ± 3.0 [**0.0016**]	-6.3 ± 2.6 [0.3393]	-9.5 ± 2.8 [0.0585]	-13.9 ± 2.0 [**0.0024**]
Somatomotor cortex	-5.0 ± 1.7 [0.6746]	-9.8 ± 2.4 [**0.0167**]	-9.6 ± 1.9 [**0.0139**]	-12.2 ± 2.9 [**0.0202**]	-16.9 ± 2.2 [**0.0002**]	-15.5 ± 2.2 [**0.0006**]
Somatosensory cortex	-5.3 ± 1.7 [0.3798]	-11.1 ± 2.1 [**0.0017**]	-12.0 ± 1.6 [**0.0004**]	-10.2 ± 2.7 [**0.0902**]	-15.5 ± 2.6 [**0.0018**]	-16.1 ± 2.7 [**0.0014**]
Visual cortex	-2.7 ± 1.8 [0.7819]	-7.9 ± 2.1 [0.0501]	-13.0 ± 1.9 [**0.0003**]	-7.9 ± 2.2 [0.1554]	-12.2 ± 2.7 [**0.0071**]	-18.7 ± 1.4 [**<0.0001**]
Hippocampal area	-8.0 ± 1.0 [**0.0314**]	-10.9 ± 1.5 [**0.0006**]	-14.0 ± 2.1 [**<0.0001**]	-9.0 ± 2.8 [0.0592]	-12.5 ± 2.9 [**0.0031**]	-15.2 ± 1.8 [**0.0003**]
CA1	-10.6 ± 1.3 [**0.0036**]	-12.1 ± 2.3 [**0.0003**]	-11.9 ± 2.0 [**0.0003**]	-11.0 ± 2.5 [**0.0137**]	-12.1 ± 2.3 [**0.0081**]	-15.8 ± 1.9 [**0.0002**]
CA3	-8.9 ± 3.1 [0.2035]	-13.3 ± 1.9 [**0.0123**]	-15.8 ± 2.8 [**0.0016**]	-10.2 ± 4.5 [0.2525]	-11.2 ± 2.7 [**0.0101**]	-18.8 ± 2.6 [**0.0061**]
Dentate gyrus	-13.2 ± 2.4 [**0.0038**]	-11.0 ± 2.2 [**0.0175**]	-9.7 ± 2.6 [**0.0210**]	-10.0 ± 2.6 [**0.0311**]	-17.6 ± 5.5 [**0.0255**]	-16.1 ± 2.0 [**0.0002**]
Ammon's horn	-9.6 ± 1.7 [**0.0222**]	-9.9 ± 1.8 [**0.0004**]	-13.8 ± 2.1 [**<0.0001**]	-11.0 ± 3.0 [**0.0332**]	-14.1 ± 3.6 [**0.0031**]	-16.4 ± 2.0 [**0.0007**]
Cerebral nuclei	-5.6 ± 0.7 [**0.0441**]	-8.1 ± 1.3 [**0.0007**]	-11.4 ± 0.8 [**<0.0001**]	-6.9 ± 2.9 [0.1442]	-9.3 ± 2.2 [0.0151]	-8.7 ± 2.0 [0.0208]
Striatum	-6.3 ± 0.6 [**0.0234**]	-7.8 ± 1.4 [**0.0014**]	-11.1 ± 0.8 [**<0.0001**]	-6.5 ± 2.8 [0.1926]	-10.1 ± 2.2 [**0.0088**]	-9.1 ± 2.1 [**0.0171**]

Caudatoputamen	-6.9 ± 1.1 [**0.0372**]	-7.3 ± 1.6 [**0.0127**]	-11.5 ± 1.2 [<**0.0001**]	-7.2 ± 3.0 [0.0635]	-8.4 ± 2.7 [0.3799]	-7.6 ± 2.4 [0.2037]
Pallidum	-2.5 ± 2.0 [0.7518]	-9.4 ± 1.4 [**0.0019**]	-12.9 ± 1.1 [<**0.0001**]	-8.6 ± 3.2 [0.0707]	-5.6 ± 2.4 [0.2851]	-7.0 ± 1.9 [0.1160]
Olfactory area	-2.5 ± 2.0 [0.8988]	-9.4 ± 1.4 [0.6733]	-12.9 ± 1.1 [0.5885]	-5.2 ± 3.1 [0.4884]	-7.5 ± 2.1 [0.1315]	-8.5 ± 2.3 [0.0536]
Brainstem regions						
Brainstem	-4.4 ± 2.0 [0.1832]	-8.0 ± 0.9 [**0.0016**]	-9.5 ± 0.8 [**0.0001**]	-6.8 ± 2.3 [0.1452]	-10.0 ± 2.1 [**0.0091**]	-10.4 ± 2.3 [**0.0054**]
Interbrain	-6.0 ± 1.8 [**0.0066**]	-9.6 ± 0.7 [<**0.0001**]	-9.7 ± 0.8 [<**0.0001**]	-5.7 ± 3.2 [0.3029]	-11.1 ± 2.0 [**0.0058**]	-10.6 ± 2.2 [**0.0071**]
Thalamus	-7.4 ± 1.8 [**0.0074**]	-6.7 ± 1.2 [**0.0073**]	-7.4 ± 1.4 [**0.0017**]	-6.6 ± 2.9 [0.2648]	-11.1 ± 2.5 [**0.0110**]	-8.7 ± 2.4 [0.0506]
Hypothalamus	-4.3 ± 2.5 [0.2955]	-13.1 ± 0.8 [<**0.0001**]	-12.4 ± 0.7 [<**0.0001**]	-4.7 ± 3.9 [0.5477]	-11.2 ± 2.1 [**0.0143**]	-13.0 ± 2.4 [**0.0029**]
Midbrain	-4.9 ± 1.8 [0.0861]	-7.4 ± 1.3 [**0.0016**]	-8.0 ± 0.9 [**0.0004**]	-10.1 ± 3.2 [0.0596]	-12.4 ± 1.8 [**0.0081**]	-12.5 ± 2.7 [**0.0056**]
Hindbrain	-2.9 ± 2.4 [0.08519]	-7.2 ± 1.6 [0.1476]	-10.5 ± 1.5 [**0.0105**]	-5.2 ± 2.8 [0.4409]	-7.3 ± 2.6 [0.1148]	-8.6 ± 2.4 [**0.0481**]
Pons	-6.4 ± 2.6 [0.3142]	-11.4 ± 1.2 [**0.0073**]	-14.0 ± 1.4 [**0.0006**]	-4.4 ± 2.9 [0.6926]	-11.0 ± 3.7 [**0.0268**]	-12.1 ± 2.5 [**0.0164**]
Medulla	-1.1 ± 2.6 [0.9924]	-4.9 ± 2.3 [0.5674]	-8.6 ± 2.1 [0.0854]	-5.5 ± 4.0 [0.4643]	-5.3 ± 2.2 [0.4278]	-6.9 ± 2.5 [0.2097]
Cerebellum regions						
Cerebellum	-4.1 ± 2.8 [0.5629]	-9.5 ± 2.1 [**0.0145**]	-10.6 ± 1.4 [**0.0029**]	-11.5 ± 5.5 [0.1046]	-8.5 ± 3.0 [0.2369]	-10.2 ± 1.9 [0.0929]
Cerebellar cortex	-4.3 ± 2.9 [0.5434]	-9.6 ± 2.1 [**0.0135**]	-10.7 ± 1.4 [**0.0029**]	-11.6 ± 5.5 [0.1009]	-8.3 ± 3.1 [0.2501]	-10.3 ± 1.8 [0.0906]
Vermal region	-4.4 ± 3.4 [0.4828]	-7.8 ± 2.2 [0.0660]	-12.8 ± 1.3 [**0.0005**]	-15.8 ± 7.8 [0.0635]	-8.9 ± 2.9 [0.3799]	-10.7 ± 2.3 [0.2037]
Fiber tracts and ventricular system						
Corpus callosum	-9.1 ± 1.7 [0.0606]	-9.5 ± 2.2 [**0.0210**]	-12.6 ± 2.0 [**0.0012**]	-9.4 ± 1.8 [**0.0363**]	-15.2 ± 2.8 [**0.0003**]	-17.1 ± 2.8 [<**0.0001**]
Ventricular system	-12.8 ± 2.7 [**0.0024**]	-8.6 ± 2.4 [**0.0419**]	-11.8 ± 1.7 [**0.0023**]	-11.0 ± 3.3 [0.1110]	-11.2 ± 2.2 [0.0742]	-6.7 ± 3.6 [0.4361]

Two-way repeated measures ANOVA (or Mixed model), Sidak post-hoc, was used for statistical analysis; Null mouse line: WT, n = 5; KO, n = 7; Y120D mouse line: WT, n = 5; KI, n = 6. The box of brain structures whose volume reduction is > 10% are highlighted in orange;

when the volume reduction ameliorates overtime, the box is highlighted in light orange. Animals whose fitting in the segmentation was not optimal were excluded from the analysis (n = 1 KO P20).

Regional volumetric changes with variable severity were observed also in females of both genotypes, in which we discovered a decrease higher than 10% in the cerebral cortex and the hippocampus (Table 5). The volumetric differences in HET-KI mice are distributed over all cerebral cortex sub-regions from P90, with a greater contribution of the prefrontal one at P200; on the other hand, we noticed a comparable but delayed volumetric decrease (P200) in HET females. Hippocampus presented a different pattern, with a major degree of diminution due to the CA1 and dentate gyrus in HET-KI and by the CA3 in HET. In addition, HET animals also depicted a strong effect in brainstem, in which atrophy is consistently present from P90. Furthermore, HET-KI showed significantly smaller size of the corpus callosum that is not consistent in null genotype.

Table 5. Regional cerebral volume differences (%) of *Mecp2*$^{-/+}$ and *Mecp2*$^{Y120D/+}$ compared to WT littermates

Anatomical Region	BIRD %difference to WT (Mean ± SEM) [p value]			Y120D %difference to WT (Mean ± SEM) [p value]		
	P60	P90	P200	P60	P90	P200
Cerebrum regions						
Cerebrum	-6.5 ± 0.8 [**0.0257**]	-8.6 ± 1.4 [**0.0033**]	-12.9 ± 1.2 [**<0.0001**]	-7.5 ± 2.1 [**0.0233**]	-11.1 ± 2.2 [**0.0109**]	-14.7 ± 2.9 [**0.0013**]
Cerebral cortex	-6.1 ± 0.9 [0.0534]	-8.4 ± 1.5 [**0.0063**]	-12.6 ± 1.3 [**<0.0001**]	-8.1 ± 2.3 [**0.0176**]	-11.6 ± 2.3 [**0.0104**]	-15.2 ± 3.0 [**0.0017**]
Prefrontal cortex	-7.2 ± 2.1 [0.1665]	-9.8 ± 2.7 [**0.0495**]	-13.3 ± 2.1 [**0.0039**]	-7.6 ± 2.5 [0.2986]	-16.0 ± 3.9 [**0.0291**]	-27.0 ± 4.6 [**0.0023**]
Entorhinal cortex	-11.8 ± 2.0 [**0.0090**]	-13.8 ± 2.6 [**0.0010**]	-15.7 ± 2.3 [**0.0002**]	-7.0 ± 2.0 [0.0607]	-11.8 ± 2.9 [**0.0233**]	-13.8 ± 2.2 [**0.0194**]
Somatomotor cortex	-4.8 ± 1.4 [0.2359]	-6.0 ± 2.1 [0.1392]	-11.4 ± 1.7 [**0.0006**]	-9.0 ± 3.1 [0.0509]	-12.5 ± 1.8 [**0.0111**]	-18.5 ± 3.6 [**0.0005**]
Somatosensory cortex	-5.1 ± 1.3 [0.1352]	-7.0 ± 1.7 [**0.0178**]	-11.8 ± 1.4 [**0.0001**]	-9.9 ± 3.9 [**0.0241**]	-11.2 ± 2.4 [**0.0345**]	-19.5 ± 3.2 [**0.0005**]
Visual cortex	-5.7 ± 1.9 [0.2896]	-8.9 ± 1.9 [0.1113]	-13.9 ± 3.1 [**0.0008**]	-9.4 ± 2.0 [**0.0089**]	-11.7 ± 2.6 [**0.0102**]	-18.0 ± 1.5 [**0.0004**]
Hippocampal area	-10.9 ± 1.6 [**0.0105**]	-13.9 ± 1.8 [**0.0010**]	-17.9 ± 1.5 [**<0.0001**]	-7.8 ± 1.1 [**0.0080**]	-12.6 ± 2.7 [**0.0019**]	-15.3 ± 2.1 [**0.0013**]

CA1	-8.1 ± 2.0 [0.1677]	-15.4 ± 1.3 [**0.0022**]	-20.1 ± 1.0 [**<0.0001**]	-8.5 ± 2.7 [**0.0200**]	-12.9 ± 3.2 [**0.0061**]	-19.6 ± 3.3 [**0.0010**]
CA3	-11.8 ± 2.1 [**0.0079**]	-15.4 ± 0.6 [**0.0009**]	-22.3 ± 2.0 [**<0.0001**]	-7.9 ± 3.9 [0.1919]	-17.3 ± 3.3 [**0.0021**]	-7.8 ± 3.4 [0.4715]
Dentate gyrus	-5.9 ± 1.7 [0.5726]	-11.0 ± 2.2 [**0.0025**]	-22.8 ± 1.4 [**<0.0001**]	-8.2 ± 3.5 [0.2082]	-12.0 ± 3.1 [**0.0438**]	-14.2 ± 4.3 [0.0990]
Ammon's horn	-9.8 ± 1.6 [**0.0361**]	-18.0 ± 1.1 [**0.0010**]	-20.6 ± 1.2 [**<0.0001**]	-8.3 ± 1.3 [**0.0183**]	-14.6 ± 3.2 [**0.0012**]	-15.5 ± 2.8 [**0.0059**]
Cerebral nuclei	-8.4 ± 0.5 [**0.0013**]	-9.6 ± 1.4 [**0.0004**]	-14.3 ± 1.0 [**<0.0001**]	-5.1 ± 1.8 [0.1291]	-9.0 ± 2.0 [**0.0216**]	-13.2 ± 2.7 [**0.0009**]
Striatum	-8.4 ± 0.5 [**0.0023**]	-9.5 ± 1.3 [**0.0009**]	-15.0 ± 0.9 [**<0.0001**]	-5.4 ± 1.6 [0.0853]	-9.2 ± 2.1 [**0.0158**]	-12.7 ± 2.8 [**0.0011**]
Caudatoputamen	-8.4 ± 0.4 [**0.0054**]	-7.3 ± 1.6 [**0.0009**]	-16.6 ± 0.6 [**<0.0001**]	-5.4 ± 1.6 [0.1551]	-8.3 ± 1.5 [**0.0306**]	-14.3 ± 3.0 [**0.0004**]
Pallidum	-8.1 ± 1.0 [**0.0028**]	-10.1 ± 1.1 [**0.0002**]	-10.6 ± 1.4 [**<0.0001**]	-3.7 ± 2.9 [0.6847]	-7.6 ± 1.8 [0.1450]	-15.6 ± 3.1 [**0.0039**]
Olfactory area	-1.9 ± 0.5 [0.8347]	-3.9 ± 1.2 [0.3222]	-8.2 ± 1.4 [**0.0045**]	-7.9 ± 2.3 [0.0504]	-10.9 ± 2.4 [**0.0331**]	-7.5 ± 3.8 [0.2446]
Brainstem regions						
Brainstem	-8.2 ± 1.0 [**0.0009**]	-11.0 ± 1.0 [**<0.0001**]	-14.6 ± 1.1 [**<0.0001**]	-8.1 ± 2.0 [**0.0325**]	-9.8 ± 1.8 [**0.0189**]	-9.5 ± 2.4 [**0.0420**]
Interbrain	-7.8 ± 0.7 [**0.0010**]	-11.0 ± 1.2 [**<0.0001**]	-14.1 ± 1.0 [**<0.0001**]	-8.1 ± 1.8 [**0.0107**]	-9.6 ± 2.0 [**0.0106**]	-13.1 ± 1.9 [**0.0006**]
Thalamus	-8.1 ± 0.9 [**0.0022**]	-9.6 ± 1.6 [**0.0004**]	-13.7 ± 0.8 [**<0.0001**]	-7.9 ± 2.5 [**0.0180**]	-8.4 ± 2.3 [**0.0450**]	-14.8 ± 2.5 [**0.0008**]
Hypothalamus	-7.3 ± 0.6 [**0.0103**]	-12.7 ± 1.0 [**<0.0001**]	-14.7 ± 1.7 [**<0.0001**]	-8.2 ± 1.0 [**0.0458**]	-11.1 ± 2.2 [**0.0050**]	-10.9 ± 2.2 [**0.0120**]
Midbrain	-8.1 ± 1.5 [**0.0037**]	-10.8 ± 1.5 [**0.0002**]	-12.1 ± 0.9 [**<0.0001**]	-6.0 ± 2.2 [0.1132]	-9.8 ± 2.0 [**0.0206**]	-11.7 ± 2.9 [**0.0112**]
Hindbrain	-8.5 ± 1.4 [**0.0034**]	-11.2 ± 0.9 [**0.0001**]	-16.8 ± 1.5 [**<0.0001**]	-9.6 ± 2.3 [0.0774]	-10.0 ± 1.8 [0.0593]	-5.2 ± 3.2 [0.6951]
Pons	-9.8 ± 1.6 [**0.0156**]	-14.1 ± 1.4 [**0.0005**]	-18.8 ± 1.4 [**<0.0001**]	-11.5 ± 2.9 [0.0649]	-11.6 ± 2.2 [0.0515]	-3.0 ± 2.8 [0.8165]
Medulla	-7.7 ± 2.0 [**0.0169**]	-9.8 ± 1.1 [**0.0020**]	-15.7 ± 1.7 [**<0.0001**]	-8.6 ± 4.0 [0.2423]	-9.3 ± 1.6 [0.1407]	-6.3 ± 3.8 [0.7596]
Cerebellum regions						
Cerebellum	-4.9 ± 2.0 [0.3783]	-5.6 ± 3.1 [0.2713]	-7.0 ± 0.9 [0.0795]	-4.1 ± 1.9 [0.2761]	-8.8 ± 1.9 [0.0595]	-10.2 ± 3.6 [**0.0172**]

Cerebellar cortex	-4.7 ± 2.1 [0.3965]	-5.7 ± 3.1 [0.2496]	-7.1 ± 0.9 [0.0737]	-4.1 ± 1.9 [0.2775]	-8.7 ± 2.0 [0.0683]	-10.0 ± 3.6 [**0.0210**]
Vermal region	-5.7 ± 2.9 [0.4119]	-5.3 ± 3.1 [0.5286]	-8.3 ± 1.0 [0.0957]	-3.2 ± 3.0 [0.6362]	-7.8 ± 1.6 [0.1695]	-11.0 ± 3.3 [**0.0421**]
Fiber tracts and ventricular system						
Corpus callosum	-8.8 ± 1.3 [0.0776]	-10.5 ± 2.5 [**0.0339**]	-15.2 ± 1.3 [**0.0004**]	-11.1 ± 2.5 [**0.0177**]	-8.6 ± 3.0 [0.1296]	-21.2 ± 2.9 [**0.0011**]
Ventricular system	-13.3 ± 4.1 [**0.0283**]	-15.8 ± 5.1 [**0.0073**]	-11.5 ± 2.2 [**0.0335**]	-5.5 ± 4.2 [0.5674]	-10.9 ± 1.9 [**0.0291**]	-19.8 ± 3.4 [**0.0005**]

Two-way repeated measures ANOVA (or Mixed model), Sidak post hoc, was used to obtain statistical significance; Null mouse line: WT, n = 6; HET, n = 6; Y120D mouse line: WT, n = 6; HET-KI, n = 6. The box of brain structures whose volume reduction is > 10% are highlighted in orange; volume reduction >20% are depicted in dark orange; when the volume reduction ameliorates overtime, the box is highlighted in light orange. Animals whose fitting in the segmentation was not optimal were excluded from the analysis (n = 1 HET-BIRD P90; n= 1 HET-KI P200, n= 1 WT from the Y120D line at P200).

Then, to clarify how specific cerebral structures contributed to brain atrophy we normalized the volumes of each brain portion to the total brain volume, in order to determine the relative volume (detailed in Tables 6 and 7). Additionally, considering our results and those brain regions that appear to have a high impact on Rett syndrome (Bedogni *et al*, 2016; Murakami *et al*, 1992; Achilly *et al*, 2021; Li *et al*, 2016; Gulmez Karaca *et al*, 2018), we analyzed the growth trajectory of cerebral cortex, hippocampus and cerebellum (Figures 33-35).

By following the specific regional development since the first time point of analysis (P20 for males and P60 for females), we reported age-related volumetric changes in both males and females affected from the *Mecp2* deficiency.

Interestingly, while the WT, KO and KI male cerebral cortex kept growing along the analysis (ended at P40), more aged *Mecp2* heterozygous females (P200) evidenced a slight but significant volumetric decline with age. By focusing on the negative slope of the curve we hypothesize the occurrence of an actual brain tissue atrophy (degeneration), or in alternative a phenomenon of premature senescence of mutant females (Figure 34).

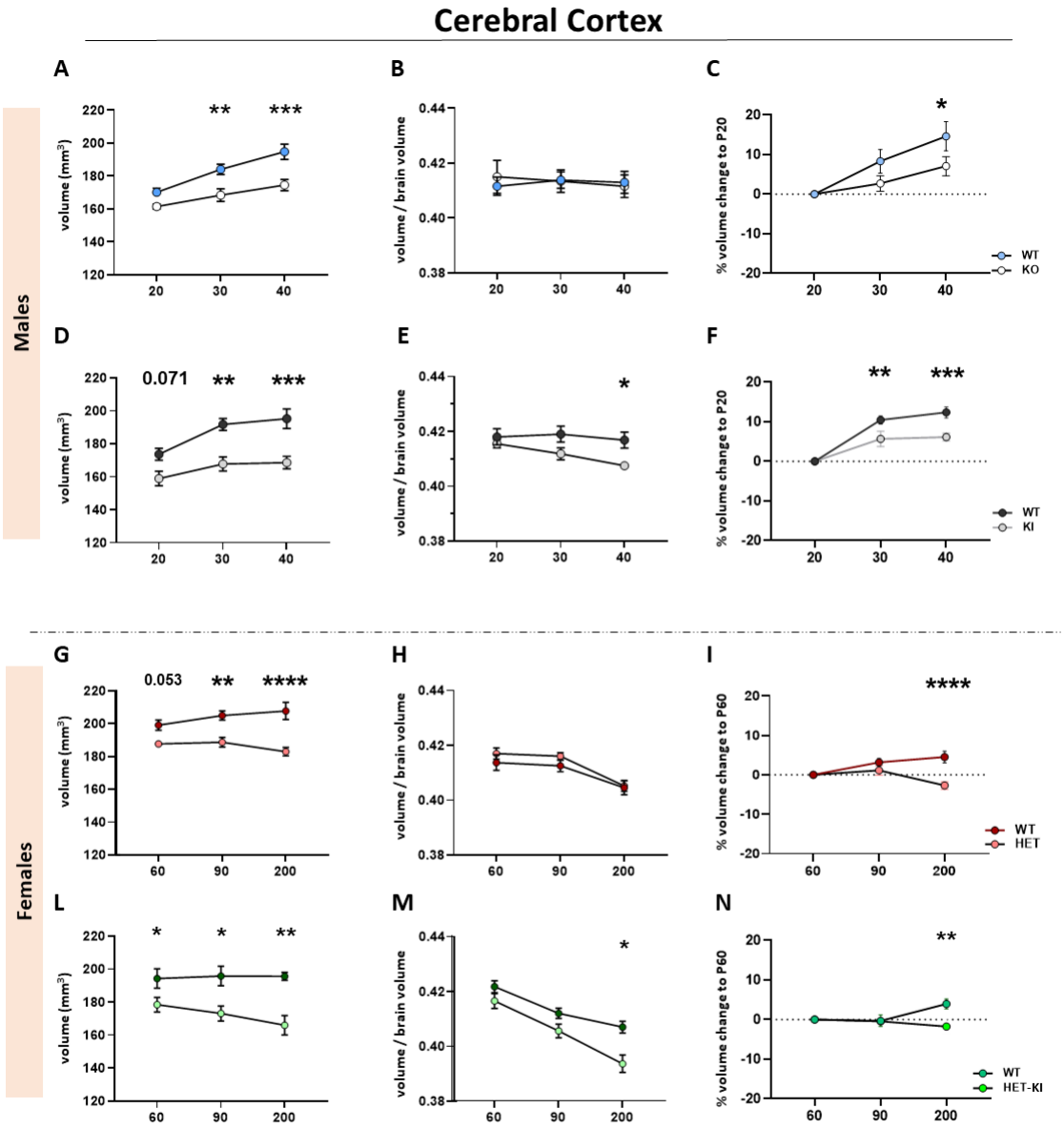

Figure 33. **Cerebral cortex displays a reduced total volume in mutant animals and different developmental trajectories in comparison to the first time point of analysis**. **(A,D,G,L)** Graphs show the total cortical volume (mm^3) across time, which appeared to be affected in all the mutant animals. **(B,E,H,M)** Graph depicts the relative volume of the cerebral cortex, which appeared smaller at a later time point in Y120D males (E) and females (M). **(C,F,I,N)** Graphs show the developmental trajectory of the cerebral cortex in comparison to the first time point of analysis in *Mecp2*-null and *Mecp2*-Y120D animals of both genders. Male mutant animals of null (C) and Y120D (F) lines showed a similar but underdeveloped growth curve compared to WT. Females from the null (I) and Y120D (N) lines displayed a different trend compared to WT at the later time point. Null mouse line: male WT, n = 5; KO, n = 7; female WT, n = 6; HET, n = 6. Y120D mouse line: male WT, n = 5; KI, n = 6; female WT, n = 6; HET-KI, n = 6. Animals whose fitting in the segmentation was not optimal were excluded from the analysis. Each mutant mouse was evaluated in comparison to their WT littermates by Two-way repeated measures ANOVA or Mixed-Model Analysis, followed by Sidak post-hoc (total and relative

volume) or Fisher's LSD (% volume growth) post-hoc; * p value < 0.05; ** p value < 0.01; *** p value < 0.001; **** p value < 0.0001;

Hippocampus was found to differ significantly in absolute volume (mm^3) in all mutant brains since early time points, and the relative volume confirmed that it is a consistent smaller structure in mutant animals. Nevertheless, by comparing how the hippocampi developed with respect to the first time point of analysis we could clearly detect that WT hippocampus continued to expand across time, whereas in mutant animals a developmental stagnation is present, although without any sign of atrophy in comparison to the first time point of observation. The defect was particularly evident at the last time point for both genotypes, with the exception of HET-KI females (Figure 34).

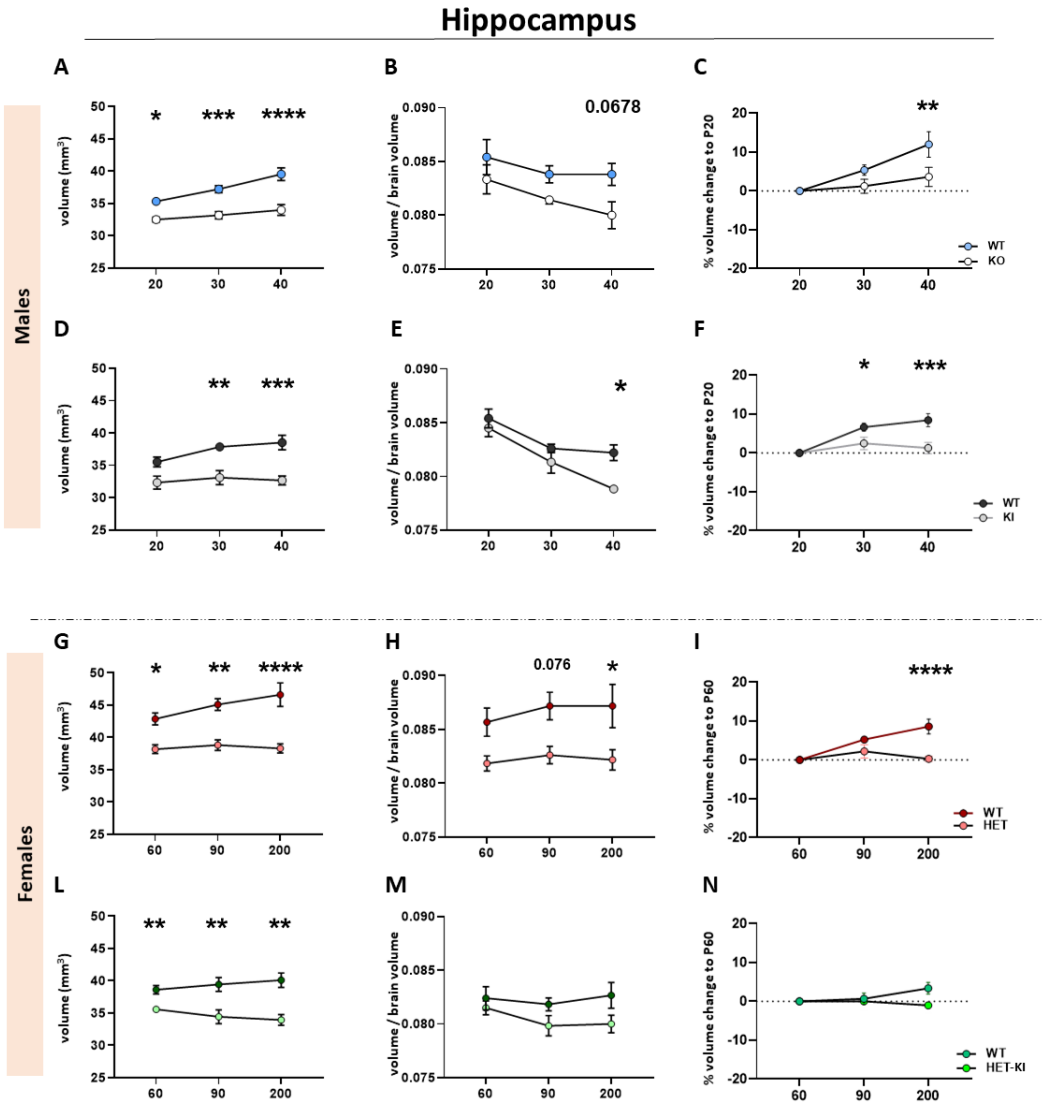

Figure 34. **Hippocampus is strongly atrophic from an early time point but displays age- and genotype- differences in its development**. **(A,D,G,L)** Graphs show the total hippocampal volume (mm^3) across time, which is strongly smaller in all the mutant animals. **(B,E,H,M)** Graph depicts the hippocampal/total brain volume ratio. Hippocampal was found to be smaller in KO (B), KI (E) and heterozygous females from the null line (H). **(C,F,I,N)** Graphs show the developmental trajectory of the hippocampus in comparison to the first time point of analysis in *Mecp2*-null and *Mecp2*-Y120D animals of both genders. WT hippocampi keep growing, while mutant animals stop their development in comparison to P20 (males) and P60 (females). Null mouse line: male WT, n = 5; KO, n = 7; female WT, n = 6; HET, n = 6. Y120D mouse line: male WT, n = 5; KI, n = 6; female WT, n = 6; HET-KI, n = 6. Animals whose fitting in the segmentation was not optimal were excluded from the analysis. Each mutant mouse was evaluated in comparison to their WT littermates by Two-way repeated measures ANOVA or Mixed-Model Analysis, followed by Sidak post-hoc (total and relative volume) or Fisher's LSD (% volume growth) post-hoc; * p value < 0.05; ** p value < 0.01; *** p value < 0.001; **** p value < 0.0001

Then, to have a comparison with a less affected brain region, we analysed the cerebellum, which presented a lower and less consistent degree of absolute reduction in total brain volume, mostly at later time points in KO males and in HET-KI females. By observing relative volumes, no significant findings were unveiled, with the exception of a slight tendency to increase in the heterozygous females of the null line. In concert with that, the developmental trajectory of the cerebellum from the first point of analysis appeared comparable between WT and mutant animals (Figure 36). This strengthens the evidence that in the RTT brain atrophy is dependent on particular structures, that deserve to be better investigated at the molecular, functional and metabolic levels.

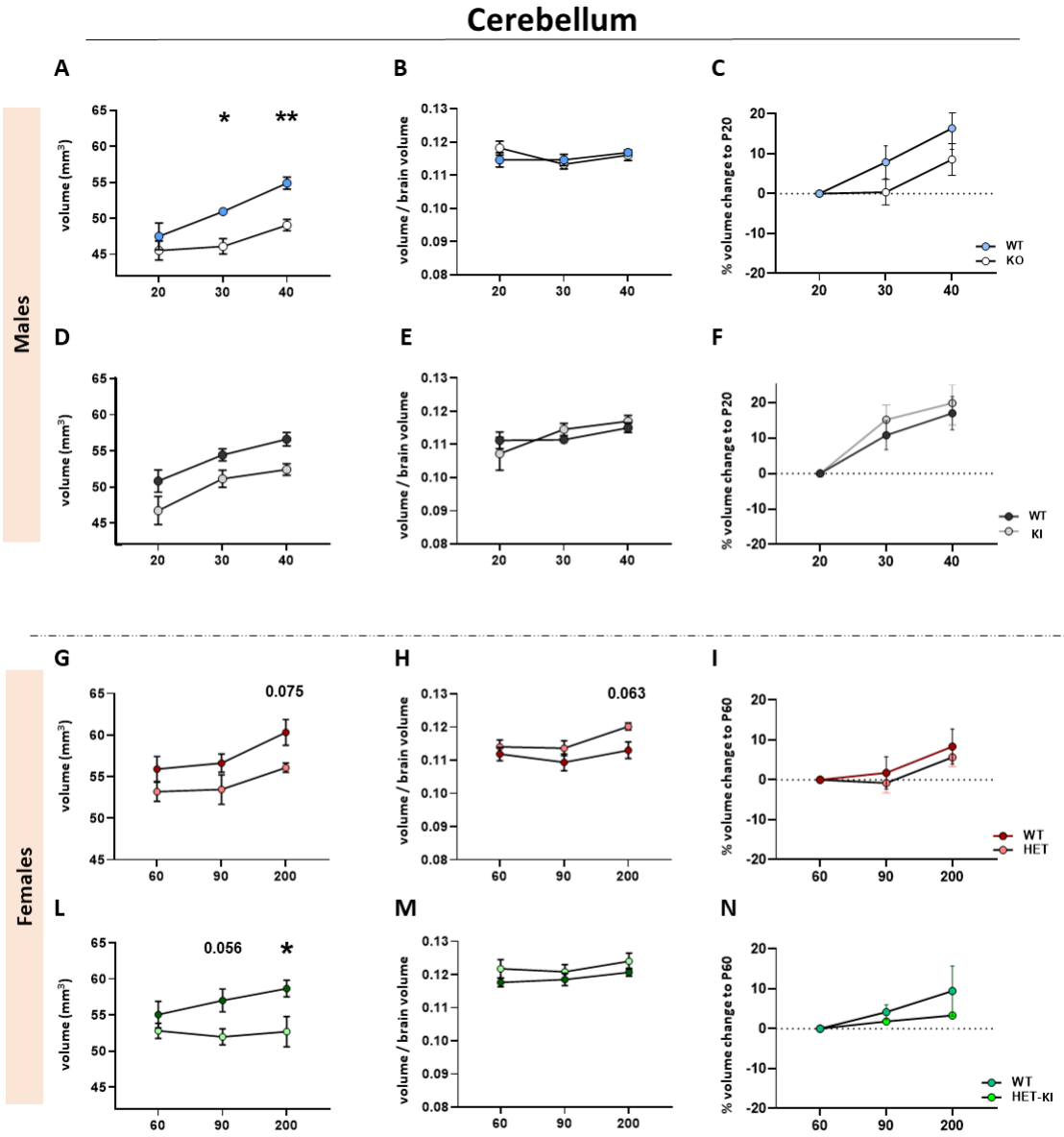

Figure 35. Cerebellar volume is not strongly affected from the *Mecp2* deficiency. (A,D,G,L) Graphs show the total cerebellar volume (mm^3) across time, which is reduced in the KO (A) and HET-KI (L) mice. **(B,E,H,M)** Graph depicts the cerebellum/total brain volume ratio. A slight tendency to increase was observed only in HET females (H). **(C,F,I,N)** Graphs show the developmental trajectory of the cerebellum in comparison to the first time point of analysis in *Mecp2*-null and *Mecp2*-Y120D animals of both genders. Developmental trajectory of mutant animals reflects those of WT littermates. Null mouse line: male WT, n = 5; KO, n = 7; female WT, n = 6; HET, n = 6. Y120D mouse line: male WT, n = 5; KI, n = 6; female WT, n = 6; HET-KI, n = 6. Animals whose fitting in the segmentation was not optimal were excluded from the analysis. Each mutant mouse was evaluated in comparison to their WT littermates by Two-way repeated measures ANOVA or Mixed-Model Analysis, followed by Sidak post-hoc (total and relative volume) or Fisher's LSD (% volume growth) post-hoc; * $p < 0.05$; ** $p < 0.01$.

Subsequently, to understand which sub-region is mostly responsible for the observed atrophy/developmental stagnation observed in the volume growth, we analysed the growth trajectory of most relevant parts of the cerebral cortex (Figure 36) and the hippocampus (Figure 37).

Sub-structural analysis of the cerebral cortex in KO animals revealed the presence of a decreased rate of development in the somatosensorial and somatomotor portions from P30, the defect is particularly evident at P40 in the visual cortex. KI animals mirror the developmental trend of KO, with the exception of the visual cortex, in which the presence of atrophy is well defined at P40. As already suggested by the growth trajectory of the whole cerebral cortex, heterozygous females from both genotypes showed regional atrophy at the late time point of analysis, bringing out the possible occurrence of premature senescence.

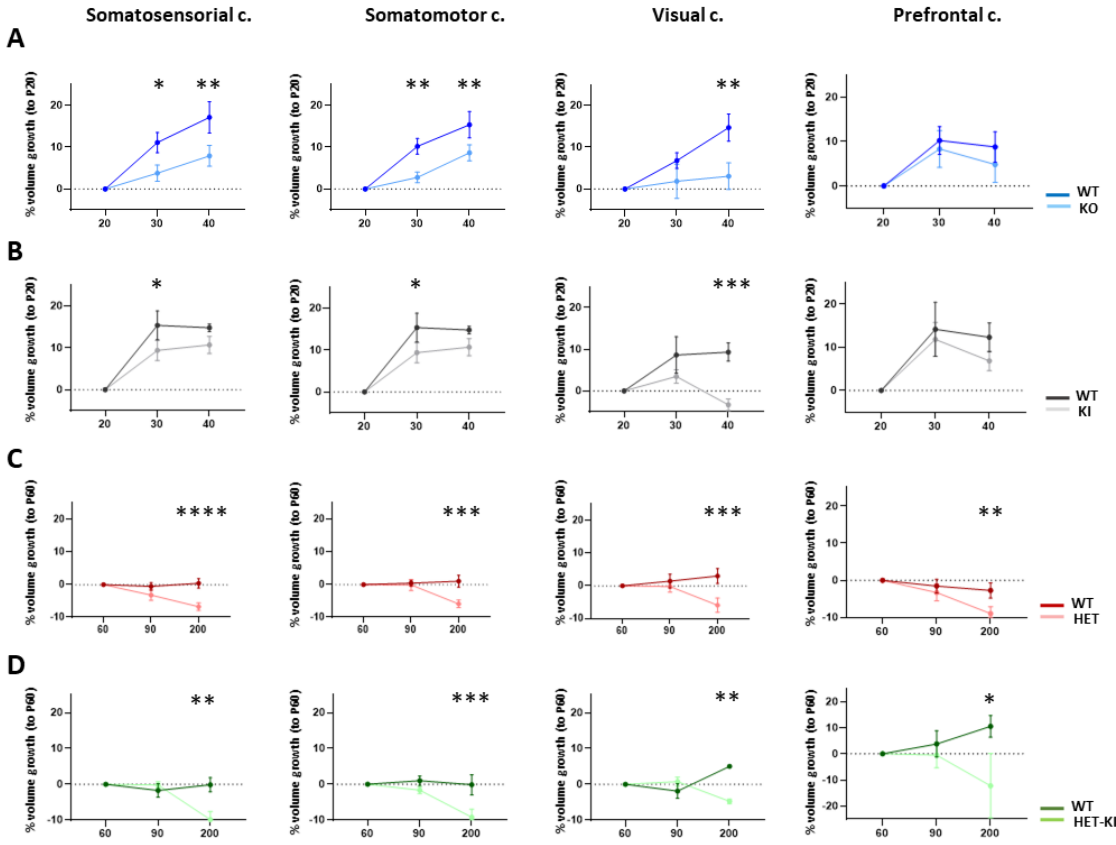

Figure 36. **Volume growth of the principal sub-regions of the cerebral cortex. (A-C)** Graphs show the developmental trajectory of different portions of the cerebral cortex in comparison to the first time point of analysis in *Mecp2*-null and *Mecp2*-Y120D animals of both genders. Mutant males (A,B) are subjected to a decreased rate of brain development, while tissue loss is consistently evident in mutant females (C,D) and in the visual cortex of KI males (B). Null mouse line: male WT, n = 5; KO, n = 7; female WT, n = 6; HET, n = 6. Y120D mouse line: male WT, n = 5; KI, n = 6; female WT, n = 6; HET-KI, n = 6. Animals whose fitting in the segmentation was not optimal were excluded from the analysis. Each mutant mouse was evaluated in comparison to their WT littermates by Two-way repeated measures ANOVA or Mixed-Model Analysis, followed by Fisher's LSD (% volume growth) post-hoc; * $p < 0.05$; ** $p < 0.01$; *** $p < 0.001$; **** $p < 0.0001$.

In the hippocampus different growth trajectories were observed. In fact, KO hippocampus grew similarly to WT controls in dentate gyrus and CA1 field, while a clear developmental stagnation was present in the CA3 field at P40. Conversely, KI shows a progressive atrophy in all the analysed sub-regions. The same trend was observed in heterozygous females, particularly in the null line.

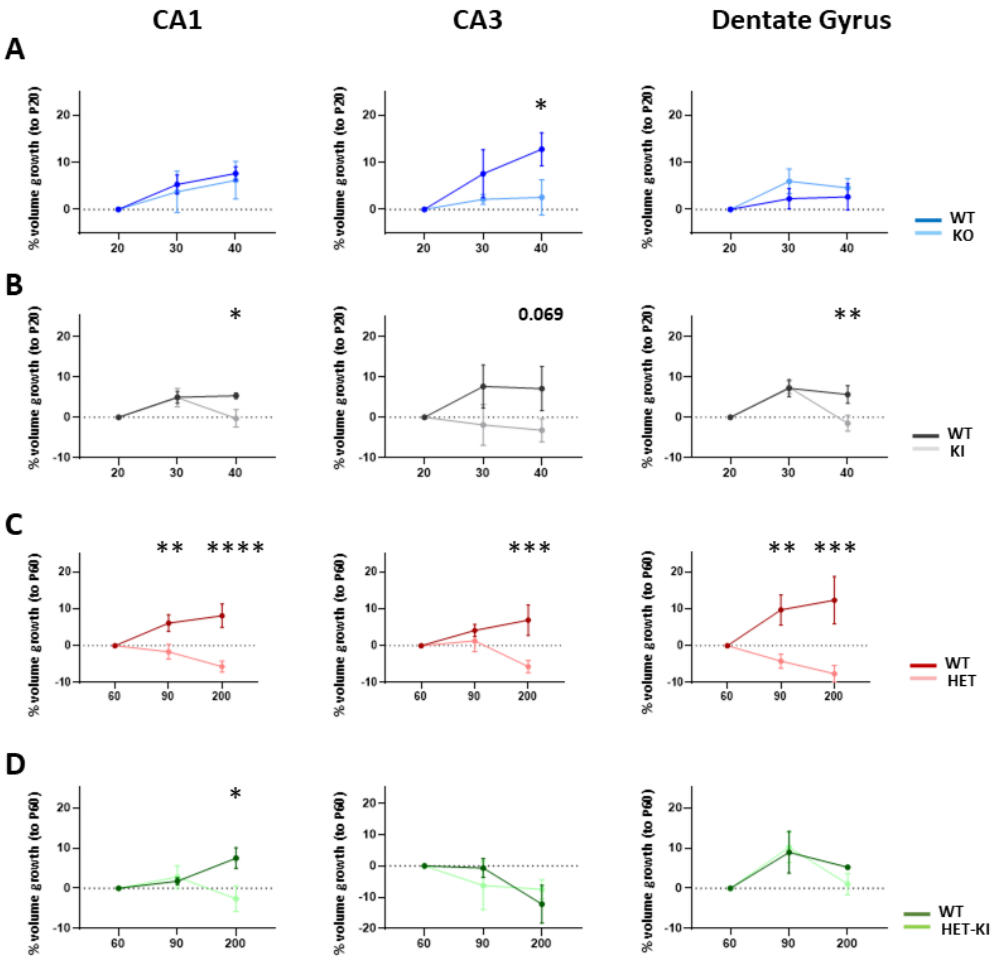

Figure 37. **Volume growth of the principal sub-regions of the hippocampus. (A-C)** Graphs depict the developmental trajectory of different portions of the hippocampus in comparison to the first time point of analysis in *Mecp2*-null and *Mecp2*-Y120D animals of both genders. KO (A) hippocampus shows a growth trajectory comparable to WT, with the exception of the CA3 field. KI (B), HET (C) and HET-KI (D) manifest a progressive atrophy in the majority of the analysed sub-regions. Null mouse line: male WT, n = 5; KO, n = 7; female WT, n = 6; HET, n = 6. Y120D mouse line: male WT, n = 5; KI, n = 6; female WT, n = 6; HET-KI, n = 6. Animals whose fitting in the segmentation was not optimal were excluded from the analysis. Each mutant mouse was evaluated in comparison to their WT littermates by Two-way repeated measures ANOVA or Mixed-Model Analysis, followed by Fisher's LSD (% volume growth) post-hoc; * $p < 0.05$; ** $p < 0.01$; *** $p < 0.001$; **** $p < 0.0001$.

Altogether our data unveiled that the major contribution in volume reduction of the RTT brain is consistently due to the cerebral cortex and hippocampus, although with a diverse rate in accordance to the genotype. Moreover, by analysing the developmental progression of specific sub-regions, we found a diverse trend in growth trajectory that

underlines a subregional effect of *Mecp2* deficiency in cerebral cortex and hippocampus development. Eventually, our data indicate the presence of a phenomenon of possible premature senescence and/or atrophy that appears particularly evident in the older heterozygous brains.

Table 6. Relative volume measurements (%) of *Mecp2*$^{-/y}$ and *Mecp2*$^{Y120D/y}$ compared to WT littermates

Anatomical Region	BIRD %difference to WT (Mean ± SEM) [p value]			Y120D %difference to WT (Mean ± SEM) [p value]		
	P20	P30	P40	P20	P30	P40
Cerebrum regions						
Cerebrum	0.6 ± 1.3 [0.8977]	0.1 ± 0.7 [>0.9999]	-0.6 ± 0.8 [0.9490]	-0.2 ± 0.8 [0.9947]	-0.9 ± 0.4 [0.6097]	-1.1 ± 0.2 [0.3828]
Cerebral cortex	0.8 ± 1.4 [0.7792]	-0.1 ± 1.0 [0.9999]	-0.4 ± 1.0 [0.9942]	-0.5 ± 0.4 [0.8281]	-1.7 ± 0.5 [0.0999]	-2.3 ± 0.3 [**0.0224**]
Anterior cingulate cortex	-1.1 ± 3.9 [0.9969]	-0.03 ± 2.4 [0.9996]	-1.9 ± 2.3 [0.9785]	-5.5 ± 2.8 [0.4690]	-4.2 ± 3.5 [0.6954]	-6.7 ± 1.7 [0.6074]
Entorhinal cortex	-2.8 ± 1.6 [0.8410]	-3.4 ± 1.7 [0.7057]	-5.0 ± 2.7 [0.4545]	1.8 ± 1.6 [0.9388]	1.6 ± 1.4 [0.9885]	-2.4 ± 1.4 [0.6655]
Somatomotor cortex	1.8 ± 1.9 [0.7444]	-1.5 ± 1.2 [0.9524]	0.6 ± 1.2 [0.9966]	-4.6 ± 1.6 [0.0823]	-6.6 ± 1.0 [**0.0041**]	-4.4 ± 0.8 [0.0888]
Somatosensory cortex	5.1 ± 1.3 [0.8261]	-2.8 ± 1.3 [0.2304]	-2.1 ± 0.9 [0.5803]	-2.4 ± 1.0 [0.6207]	-5.0 ± 1.4 [0.0348]	-5.0 ± 1.3 [0.0348]
Visual cortex	2.7 ± 2.8 [0.6866]	0.6 ± 1.1 [0.9993]	-3.2 ± 1.3 [0.5981]	0.2 ± 2.0 [0.9121]	-1.3 ± 1.9 [0.7597]	-7.9 ± 1.0 [**0.0398**]
Hippocampal area	-2.8 ± 1.5 [0.5448]	-2.6 ± 0.5 [0.3755]	-4.4 ± 1.6 [0.0678]	-1.2 ± 0.9 [0.7879]	-1.8 ± 1.3 [0.5659]	-4.0 ± 0.3 [**0.0112**]
CA1	-5.6 ± 1.5 [0.3662]	-4.0 ± 1.4 [0.1025]	-2.2 ± 1.5 [0.3555]	-3.2 ± 1.7 [0.3319]	-0.2 ± 1.1 [0.9986]	-4.8 ± 0.4 [0.2618]
CA3	-1.9 ± 4.4 [>0.9999]	-5.2 ± 1.7 [0.5322]	-6.3 ± 2.7 [0.4470]	-2.7 ± 3.1 [0.9252]	-7.8 ± 5.0 [0.3351]	-8.1 ± 1.8 [0.1350]
Dentate gyrus	-7.0 ± 2.9 [0.4660]	-1.6 ± 1.4 [0.9976]	0.3 ± 2.3 [0.9891]	-2.2 ± 1.4 [0.9976]	1.5 ± 2.4 [0.8750]	-5.2 ± 0.7 [0.5643]
Ammon's horn	-3.8 ± 2.5 [0.6224]	-4.5 ± 1.1 [0.1802]	-4.2 ± 1.6 [0.3887]	-3.4 ± 1.7 [0.3284]	-3.7 ± 2.4 [0.5334]	-5.5 ± 0.6 [0.0756]
Cerebral nuclei	-0.1 ± 1.2 [0.9842]	0.6 ± 1.2 [0.9818]	-1.4 ± 0.4 [0.6463]	1.2 ± 2.5 [0.8575]	1.9 ± 0.6 [0.6801]	3.3 ± 0.7 [0.3350]

Striatum	-1.2 ± 1.2 [0.6398]	0.9 ± 1.3 [0.8996]	-1.1 ± 0.4 [0.8903]	1.6 ± 2.5 [0.7852]	1.0 ± 0.8 [0.9828]	2.9 ± 0.5 [0.3765]
Caudatoputamen	-1.3 ± 2.1 [0.6637]	1.5 ± 1.6 [0.9323]	-1.5 ± 0.8 [0.8836]	0.9 ± 2.7 [0.9694]	2.9 ± 1.7 [0.4544]	4.5 ± 0.7 [0.1647]
Pallidum	-4.4 ± 1.0 [0.3759]	-0.9 ± 1.6 [0.9999]	-3.1 ± 1.1 [0.4543]	-0.6 ± 2.7 [0.9993]	6.0 ± 1.8 [0.1681]	5.3 ± 2.1 [0.3351]
Olfactory area	3.2 ± 1.5 [0.6823]	4.4 ± 3.6 [0.5808]	-6.0 ± 1.2 [0.2807]	3.0 ± 1.6 [0.3679]	3.9 ± 1.0 [0.1798]	3.6 ± 1.6 [0.1373]
Brainstem regions						
Brainstem	1.6 ± 1.2 [0.8988]	0.6 ± 1.3 [0.9881]	0.6 ± 1.4 [0.9677]	1.3 ± 0.8 [0.4754]	1.2 ± 0.3 [0.6335]	1.3 ± 0.6 [0.5914]
Interbrain	-0.7 ± 1.3 [0.9432]	-1.1 ± 1.1 [0.9091]	0.4 ± 1.0 [0.9854]	2.6 ± 3.4 [0.7667]	-0.1 ± 0.5 [0.9979]	1.0 ± 0.7 [0.9783]
Thalamus	-2.2 ± 2.1 [0.8580]	2.1 ± 1.5 [0.8587]	2.9 ± 1.5 [0.3625]	1.8 ± 3.5 [0.9518]	-0.04 ± 1.5 [>0.9999]	3.1 ± 0.7 [0.8065]
Hypothalamus	1.1 ± 1.6 [0.8948]	-4.9 ± 1.2 [**0.0462**]	-2.6 ± 1.0 [0.1992]	3.5 ± 3.7 [0.7055]	-0.2 ± 1.7 [0.9922]	-1.6 ± 1.6 [0.8972]
Midbrain	1.6 ± 0.9 [0.7181]	1.2 ± 1.0 [0.5967]	2.3 ± 1.0 [0.3914]	-2.2 ± 1.8 [0.5519]	-1.5 ± 1.1 [0.8553]	-1.1 ± 1.0 [0.8553]
Hindbrain	3.3 ± 1.7 [0.8007]	1.5 ± 2.3 [0.9654]	-0.5 ± 2.3 [0.9973]	3.0 ± 1.6 [0.4125]	4.1 ± 0.9 [0.1516]	3.3 ± 1.5 [0.2787]
Pons	0.2 ± 2.4 [0.9999]	-3.1 ± 1.8 [0.7284]	-4.5 ± 1.7 [0.4679]	3.9 ± 3.1 [0.3569]	-0.2 ± 2.3 [>0.9999]	-0.6 ± 1.0 [0.9711]
Medulla	4.9 ± 1.8 [0.7143]	4.0 ± 3.1 [0.7860]	1.6 ± 1.0 [0.9675]	2.6 ± 2.8 [0.5901]	6.4 ± 0.7 [0.0384]	5.3 ± 1.8 [0.1672]
Cerebellum regions						
Cerebellum	3.1 ± 1.8 [0.4271]	-1.2 ± 1.2 [0.9301]	-0.6 ± 1.4 [0.9827]	-3.9 ± 4.5 [0.6749]	2.8 ± 1.6 [0.8203]	1.6 ± 1.5 [0.9424]
Cerebellar cortex	3.0 ± 1.9 [0.4565]	-1.4 ± 1.2 [0.8608]	-0.7 ± 1.4 [0.9811]	-4.0 ± 4.5 [0.5495]	2.9 ± 1.7 [0.7949]	1.6 ± 1.5 [0.9607]
Vermal region	3.8 ± 1.8 [0.4896]	0.7 ± 1.8 [0.9981]	-3.1 ± 1.5 [0.6081]	-8.6 ± 7.3 [0.2775]	2.4 ± 1.7 [0.9745]	1.1 ± 2.7 [>0.9999]
Fiber tracts and ventrycular system						
Corpus callosum	-3.1 ± 2.4 [0.8655]	-1.1 ± 1.8 [0.9927]	-2.8 ± 1.5 [>0.9999]	-1.5 ± 1.1 [0.6737]	-4.7 ± 3.0 [0.3283]	-6.4 ± 1.7 [0.0606]
Ventricular system	-7.7 ± 2.4 [**0.0307**]	-0.1 ± 2.0 [0.8813]	-1.8 ± 1.9 [0.5243]	-3.1 ± 3.2 [0.7904]	-0.1 ± 1.9 [0.9840]	5.5 ± 2.3 [0.2216]

Two-way repeated measure ANOVA (or Mixed model), Sidak post-hoc, was used to obtain statistical significance; Null mouse line: WT, n = 5; KO, n = 7; Y120D mouse line: WT, n = 5; KI, n = 6. Orange box: volume decrease > 5%; Light orange: volume decrease ameliorates overtime. Green box: volume increase > 5%; Light green: volume increase ameliorates overtime. Animals whose fitting in the segmentation was not optimal were excluded from the analysis (n = 1 KO P20).

Table 7. Relative volume measurements (%) of *Mecp2*$^{-/+}$ and *Mecp2*$^{Y120D/+}$ compared to WT littermates

Anatomical Region	BIRD %difference to WT (Mean ± SEM) [p value]			Y120D %difference to WT (Mean ± SEM) [p value]		
	P60	P90	P200	P60	P90	P200
Cerebrum regions						
Cerebrum	0.3 ± 0.5 [0.9535]	0.6 ± 0.4 [0.6959]	-0.2 ± 0.4 [0.9752]	-0.4 ± 0.4 [0.5102]	-0.7 ± 0.4 [0.3685]	-2.4 ± 0.3 [**0.0027**]
Cerebral cortex	0.8 ± 0.9 [0.6446]	0.8 ± 0.3 [0.5215]	0.2 ± 0.5 [0.9952]	-1.1 ± 0.6 [0.1869]	-1.3 ± 0.5 [0.1398]	-2.8 ± 0.7 [**0.0118**]
Anterior cingulate cortex	-0.4 ± 1.6 [>0.9999]	-0.7 ± 1.9 [0.9739]	1.5 ± 1.1 [0.8756]	-0.2 ± 2.8 [0.8445]	-6.3 ± 2.9 [0.2997]	-16.6 ± 2.6 [**0.0423**]
Entorhinal cortex	-5.4 ± 1.7 [0.2701]	-5.2 ± 2.1 [0.4181]	-3.4 ± 1.8 [0.5508]	0.2 ± 0.8 [>0.9999]	-1.5 ± 1.6 [0.8141]	-1.2 ± 1.0 [0.8715]
Somatomotor cortex	2.1 ± 1.0 [0.2233]	3.5 ± 0.7 [0.0655]	1.5 ± 1.1 [0.5566]	-2.0 ± 1.4 [0.7563]	-2.2 ± 1.0 [0.6795]	-6.8 ± 1.3 [**0.0050**]
Somatosensory cortex	1.9 ± 1.0 [0.4607]	2.4 ± 0.8 [0.2031]	1.0 ± 0.9 [0.8777]	-3.1 ± 2.3 [0.1961]	-0.8 ± 0.9 [0.9798]	-7.8 ± 1.0 [**0.0026**]
Visual cortex	1.1 ± 1.6 [0.9910]	0.3 ± 0.9 [0.7853]	-1.3 ± 2.6 [0.9910]	-2.4 ± 0.6 [0.2558]	-1.6 ± 1.1 [0.7803]	-5.9 ± 1.7 [0.1024]
Hippocampal area	-4.4 ± 0.9 [0.1117]	-5.3 ± 0.8 [0.0760]	-5.8 ± 1.0 [**0.0252**]	-0.8 ± 0.8 [0.6522]	-2.6 ± 1.1 [0.2476]	-2.9 ± 0.9 [0.4147]
CA1	-1.4 ± 1.4 [>0.9999]	-6.9 ± 0.2 [0.1348]	-5.8 ± 1.0 [**0.0127**]	-1.5 ± 1.4 [0.9978]	-3.0 ± 1.7 [0.1736]	-8.0 ± 1.4 [**0.0089**]
CA3	-5.4 ± 2.1 [0.2024]	-6.7 ± 2.1 [0.2009]	-10.8 ± 1.6 [**0.0271**]	-0.9 ± 5.4 [0.9936]	-7.9 ± 2.1 [0.4099]	-5.9 ± 3.4 [0.5833]
Dentate gyrus	0.9 ± 1.6 [0.9846]	-9.5 ± 2.6 [0.0608]	-11.2 ± 1.5 [**0.0221**]	-1.1 ± 2.4 [0.9881]	-2.1 ± 1.9 [0.6080]	-1.7 ± 3.9 [0.9920]
Ammon's horn	-3.3 ± 1.0 [0.3701]	-6.5 ± 0.8 [0.0741]	-8.9 ± 0.9 [**0.0017**]	-1.2 ± 1.7 [0.8870]	-4.9 ± 1.8 [0.2159]	-3.1 ± 1.3 [0.7223]
Cerebral nuclei	-1.6 ± 0.6 [0.2908]	-0.4 ± 1.1 [0.9111]	-1.8 ± 0.7 [0.1142]	2.2 ± 1.0 [0.2345]	1.6 ± 0.9 [0.4721]	-0.6 ± 1.3 [0.9370]

Striatum	-1.7 ± 0.6 [0.3384]	-0.3 ± 1.1 [0.9956]	-2.6 ± 0.8 [**0.0280**]	1.9 ± 1.1 [0.3738]	1.3 ± 0.8 [0.6694]	-0.01 ± 0.9 [>0.9999]
Caudatoputamen	-1.6 ± 0.9 [0.5614]	-1.0 ± 1.3 [0.8110]	-4.4 ± 0.8 [**0.0035**]	1.9 ± 1.4 [0.3673]	2.5 ± 1.3 [0.5102]	-1.8 ± 1.4 [0.3081]
Pallidum	-1.4 ± 0.5 [0.7729]	-1.1 ± 1.3 [0.9172]	2.3 ± 1.1 [0.7729]	-3.7 ± 1.2 [0.8026]	3.2 ± 1.7 [0.7224]	-3.1 ± 3.0 [0.6395]
Olfactory area	5.3 ± 1.3 [**0.0405**]	5.8 ± 1.6 [**0.0232**]	5.2 ± 1.3 [0.0516]	-0.8 ± 0.7 [0.8940]	-0.6 ± 1.2 [0.9458]	5.9 ± 1.8 [**0.0263**]
Brainstem regions						
Brainstem	-1.4 ± 0.5 [0.3714]	-2.0 ± 0.9 [0.1145]	-2.3 ± 0.5 [0.0531]	-0.9 ± 1.0 [0.9428]	0.7 ± 0.5 [0.7794]	3.8 ± 1.3 [**0.0081**]
Interbrain	-1.0 ± 0.5 [0.7758]	-1.9 ± 1.5 [0.5418]	-1.7 ± 0.9 [0.4395]	-1.0 ± 1.0 [0.9864]	0.9 ± 0.7 [0.7503]	-0.3 ± 1.7 [0.9820]
Thalamus	-1.3 ± 0.7 [0.7004]	-0.4 ± 1.8 [0.9832]	-1.2 ± 0.9 [0.8462]	-0.8 ± 1.6 [0.9985]	2.2 ± 1.3 [0.4269]	-2.4 ± 0.3 [0.6487]
Hypothalamus	-0.5 ± 0.4 [0.9308]	-3.9 ± 1.6 [0.0655]	-2.4 ± 1.6 [0.4544]	-1.2 ± 1.0 [0.9375]	-0.8 ± 1.2 [0.8352]	2.3 ± 3.6 [0.6569]
Midbrain	-1.4 ± 1.2 [0.4855]	-1.8 ± 1.0 [0.4034]	0.7 ± 0.5 [0.9245]	1.3 ± 0.9 [0.6710]	0.7 ± 0.4 [0.9303]	1.1 ± 1.2 [0.9679]
Hindbrain	-1.8 ± 1.1 [0.4903]	-2.2 ± 1.1 [0.5162]	-4.7 ± 0.8 [**0.0063**]	-2.4 ± 1.7 [0.8812]	0.5 ± 1.2 [0.9879]	8.7 ± 2.8 [**0.0137**]
Pons	-3.2 ± 1.6 [0.5513]	-5.3 ± 2.0 [0.1221]	-7.0 ± 1.1 [**0.0150**]	-4.5 ± 2.6 [0.5647]	-1.4 ± 1.2 [0.9513]	11.4 ± 3.2 [**0.0473**]
Medulla	-1.0 ± 1.7 [0.9525]	-0.6 ± 0.9 [0.9727]	-3.6 ± 1.0 [0.2334]	-1.4 ± 3.9 [0.9985]	1.5 ± 1.3 [0.9494]	7.3 ± 3.1 [0.1455]
Cerebellum regions						
Cerebellum	2.1 ± 1.9 [0.8493]	3.7 ± 2.0 [0.4823]	6.5 ± 0.9 [0.0627]	3.4 ± 2.4 [0.4995]	1.8 ± 1.8 [0.7599]	2.9 ± 2.1 [0.8891]
Cerebellar cortex	2.3 ± 2.0 [0.7041]	3.6 ± 2.0 [0.5667]	6.4 ± 0.9 [0.0680]	3.5 ± 2.4 [0.6249]	2.0 ± 1.9 [0.7878]	3.1 ± 2.1 [0.8102]
Vermal region	1.3 ± 2.9 [0.9268]	4.1 ± 2.1 [0.5957]	5.1 ± 1.4 [0.4716]	4.5 ± 2.7 [0.4215]	3.0 ± 1.6 [0.5557]	1.9 ± 1.9 [0.7783]
Fiber tracts and ventricular system						
Corpus callosum	-2.2 ± 0.8 [0.9570]	-1.5 ± 1.4 [0.9972]	-2.7 ± 0.9 [0.7456]	-4.3 ± 2.8 [0.9162]	2.1 ± 2.3 [0.6060]	-9.7 ± 0.7 [0.1224]
Ventricular system	-7.0 ± 3.9 [0.1841]	-7.5 ± 4.5 [0.3096]	1.3 ± 1.8 [0.9848]	1.8 ± 2.7 [0. 9638]	-0.5 ± 1.8 [0.9500]	-8.0 ± 4.1 [0.1550]

Two-way repeated measure ANOVA (or Mixed model), Sidak post hoc, was used to obtain statistical significance; Null mouse line: WT, n = 6; HET, n = 6; Y120D mouse line: WT, n = 6; HET-KI, n = 6. Orange box: volume decrease < 5%; Light orange: volume decrease ameliorates overtime. Green box: volume increase > 5%; Light green: volume increase ameliorates overtime. Animals whose fitting in the segmentation was not optimal were excluded from the analysis (n = 1 HET-BIRD P90; n= 1 HET-KI P200, n= 1 WT from the Y120D line at P200).

6.4 Magnetic resonance spectroscopy of *Mecp2* deficient mice reveals regional dysregulation of metabolites related to neurotransmission and energy metabolism

To assess whether the *Mecp2* deficient mouse brain suffers from specific metabolic defects, we proceeded with a longitudinal ^{1}H-MRS study, selecting for the analysis the highly affected hippocampus and the little compromised cerebellum.

As a matter of fact, we did not reveal consistent metabolites' deregulation across *Mecp2* genotypes and/or genders. However, we noticed that few metabolites were more often found dysregulated among different experimental groups.

Great care is warranted in phosphocreatine (PCr), whose levels exhibit a significant decline in the null line in the hippocampus and in the Y120D line in the cerebellum. PCr importance in the ATP production has already been discussed in the *Cdkl5* chapter, and it fit well with the energy homeostasis failings diffusely reported in Rett syndrome (Großer *et al*, 2012; Dave *et al*, 2019; Zuliani *et al*, 2020).

Figure 38 shows the metabolites mostly affected in the hippocampus, which are mainly related to neurotransmission. In fact, glutamine levels were elevated in KO from early time points, and in concert with that, glutamate-to-glutamine ratio drastically dropped, a defect also extended to the cerebellum (Figure 39). A common feature between KO and KI animals is the decrease in GABA levels at the later stages of the analysis. Of relevance, GABA, together with glutamate and glutamine, represent the pivotal neurotransmitters for the maintenance of excitation/inhibition balance. Altogether, this suggested the presence of a regional unbalance in the E/I equilibrium, that is in line with the synaptic defect reported in *Mecp2* literature (Li *et al*, 2016; Lu *et al*, 2016) and with results obtained through the restoration of *Mecp2* in a GABAergic conditional KO mouse, where authors observed a reversal of several RTT phenotypes (Ure *et al*, 2016).

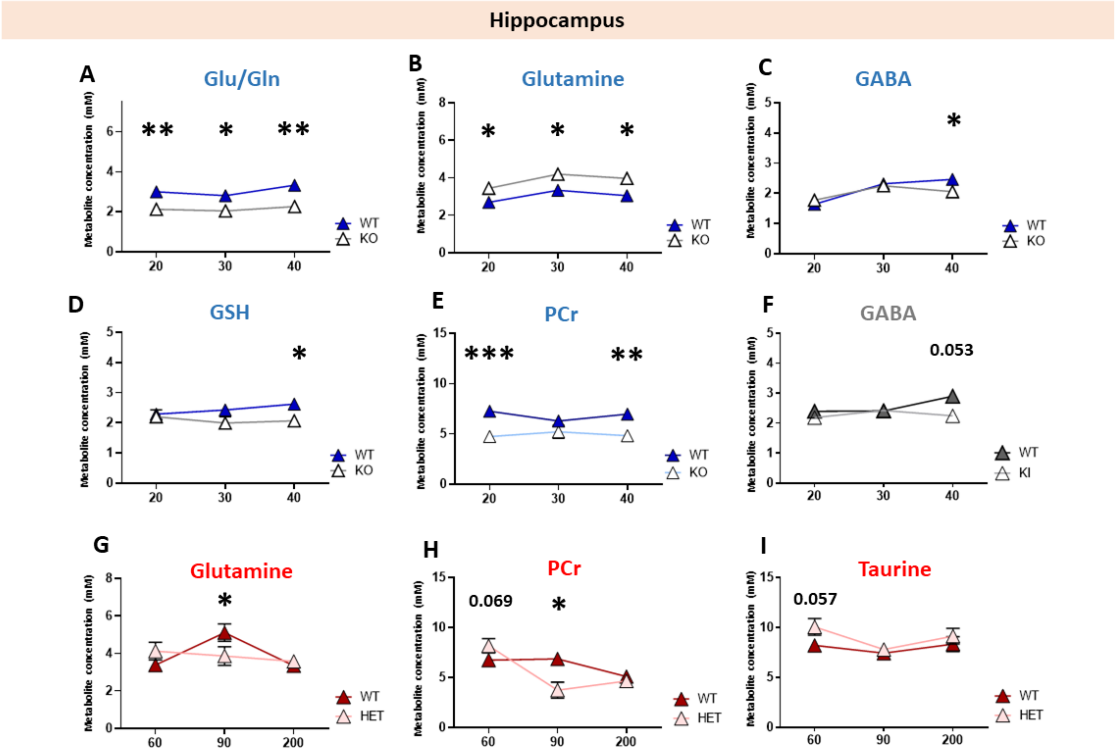

Figure 38. ***Mecp2*** **deficiency in the hippocampus affects metabolites related to neurotransmission.** Graphs show the most significantly deregulated metabolites (mM) in the hippocampus. **(A-E)** Graphs depict a deregulation in Glu/Gln ratio, glutamine, GABA, GSH and PCr in KO mice; **(F)** Graph shows reduced levels of GABA in KI at P20. **(G-I)** Graphs display glutamine, PCr and taurine dysregulation in HET females from the null line. Gln: glutamine; Glu: glutamate; GSH: glutathione; PCr: phosphocreatine; Each mutant mouse was evaluated in comparison to their WT littermates by Two-way repeated measures ANOVA or Mixed-Model Analysis, Fisher post-hoc; * p value < 0.05; ** p value < 0.01; *** p value < 0.001. All graphs represent mean ± SEM.

Furthermore, antioxidants were found to be deregulated solely in the null line. Elevated taurine levels were measured in HET cerebellum and hippocampus at P200, while a downregulation of GSH was noticed in the P40 hippocampus of KO animals, thus suggesting deranged neuronal protective mechanisms. Concomitantly, Figure 39 shows the major metabolites deregulated in the cerebellum, which mainly belong to the energy homeostasis and oxidative stress classes. In particular, n-acetyl aspartate (NAA) impaired levels were detected at the first time point of analysis in both genders of mutant animals from the null line, although with opposite direction. In fact, in KO mice n-acetyl aspartate was lowered, while HET animals had upregulated levels. Importantly, reduced levels of inositol was detected in KO animals at P20.

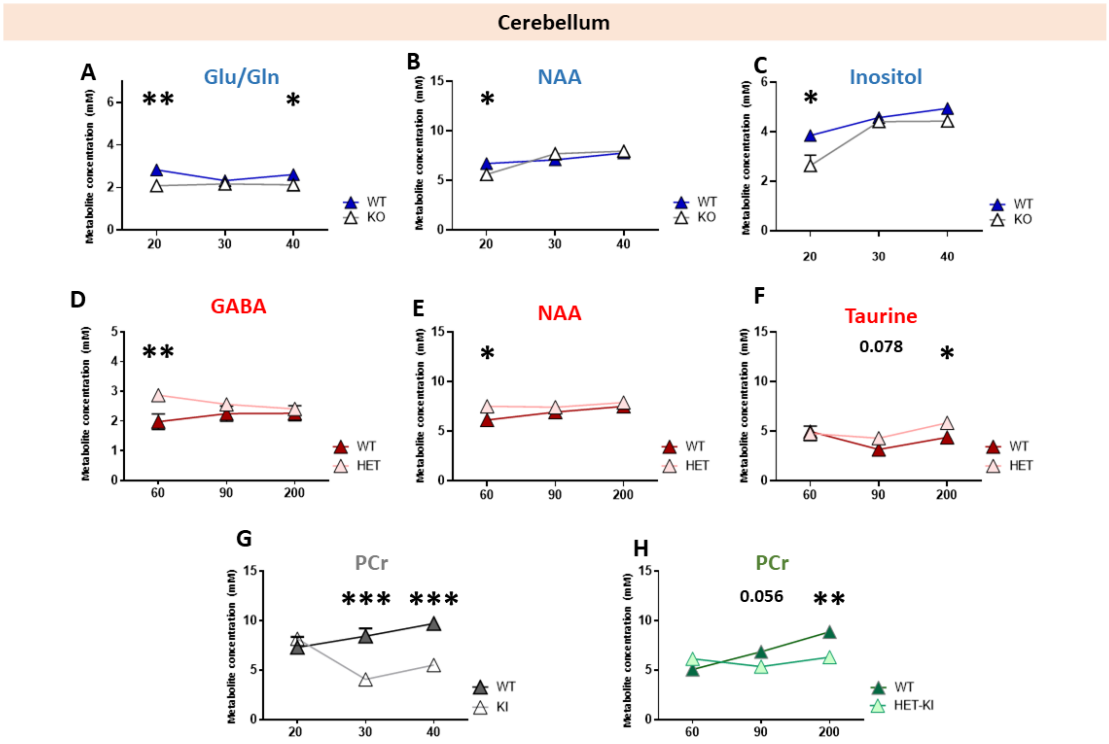

Figure 39. ***Mecp2*** **deficiency in the cerebellum leads to altered levels of metabolites having a role in energy homeostasis.** Graphs show the most significantly deregulated metabolites (mM) in the cerebellum. **(A-C)** Graphs depict a deregulated concentration of Glu/Gln ratio, NAA and inositol in KO mice; **(D-F)** Graph shows altered levels of GABA, NAA and taurine in HET females. **(G)** Graph displays a strong PCr reduction in KI animals. **(H)** Graph shows reduced levels of PCr in HET-KI mice. Gln: glutamine; Glu: glutamate; PCr: phosphocreatine; NAA: N-acetyl-aspartate; Each mutant mouse was evaluated in comparison to their WT littermates by Two-way repeated measures ANOVA or Mixed-Model Analysis, Fisher post-hoc; * p value < 0.05; ** p value < 0.01; *** p value < 0.001. All graphs represent mean ± SEM.

Taken together, ^{1}H-MRS results unveil that further studies should be focused on phosphocreatine related pathways, but also on the correct equilibrium of the neurotransmitters amount.

7. Discussion

Although they are recognized as separate disorders, Rett syndrome (RTT) and *CDKL5* Deficiency Disorder (CDD) are both rare X-linked developmental diseases sharing a plethora of symptoms among which global developmental delay appears as the main overlapping feature. Mutations in the transcriptional regulator methyl-CpG-binding protein 2 (*MeCP2*) account for over 95% of classic RTT cases (Amir *et al*, 1999), while CDD is caused by mutations in the Cyclin-Dependent Kinase-Like 5 (*CDKL5*) gene (Fehr *et al*, 2013). Over the years, many studies focused on understanding the molecular consequences of *MeCP2* and *CDKL5* deficiency, however up to date a cure for these pathologies is not available and treatments are basically aimed at the management of secondary symptoms.

One of the main gaps of knowledge in RTT and CDD is the absence of objective biological markers that could track how physiological processes change with the diseases and to what extent a pharmacological treatment has a beneficial effect. Thus, the aim of my project was to identify for both diseases good biomarker(s) that could be helpful in the identification of effective therapeutic approaches. To do this purpose, we elegised Magnetic Resonance Imaging (MRI), a non-invasive method which produces three-dimensional images that could be exploited in structural, functional and metabolic analyses. Of relevance, neuroimaging is an employed technique for the identification of anomalies in brain development in autistic spectrum disorders (Colvert *et al*, 2015; Hisle-Gorman *et al*, 2018).

Of note, results obtained through MRI on *Cdkl5* mouse model and the consequent initial molecular validation have recently been published in a work in which I appear as first author (Carli *et al*, 2021).

7.1 MRI analysis reveals a mitochondrial defect in the *Cdkl5* KO brain

We started by using different approaches of MRI in adult *Cdkl5* knockout (KO) mice and the corresponding WT littermates (Amendola *et al*, 2014). In line with previous studies that described the absence of gross volume shrinkage of CDD patients' brain (Bodian *et al*, 2018; Liang *et al*, 2011; Paine *et al*, 2012), e*x vivo* and *in vivo* MRI images disclosed preserved cerebral volume in *Cdkl5* KO and heterozygous mutant mice compared to controls. Indeed, head circumference of CDD patients appeared normal at

birth in approximately 90% of cases; subsequent volume reduction was not consistently reported (Frullanti *et al*, 2019; Tang *et al*, 2021). When described, the progressive brain structural degeneration generally consisted with the presence of infantile epileptic spasms (Koo & Hwang, 1996; Olson *et al*, 2019; Bahi-Buisson *et al*, 2008; Tang *et al*, 2021). Importantly, despite a predisposition to spontaneous seizures is reported in different mouse models of *Cdkl5*, they do not manifest overt epilepsy (Amendola *et al*, 2014; Okuda *et al*, 2018), thus making it reasonable that the observed human brain changes are a secondary effect of the epileptic encephalopathy.

Then, through MEMRI we disclosed the presence of a hyper stimulated brain activity in several brain regions of *Cdkl5* mutant brain, particularly in the hippocampus and in the visual system, cerebral areas that are respectively associated with learning and memory abilities and visual capacity, which are generally affected in CDD patients (Amendola *et al*, 2014; Lupori *et al*, 2019; Ren *et al*, 2019; Okuda *et al*, 2017). The diverse regional influence of *Cdkl5* well-fits with its ability to shuttle between nucleus and cytoplasm that varies depending on the brain region (Rusconi *et al*, 2008) and was supported by our MEMRI results. In particular, manganese accumulation through voltage-gated Ca^{2+} channels could reflect the described overall disruption of the excitation/inhibition (E/I) balance (Pizzo *et al*, 2016; Tang *et al*, 2017; Negraes *et al*, 2021) and confirmed Cdkl5 relevance for specific brain circuitries. The generation of conditional KO of *Cdkl5* in forebrain glutamatergic neurons was pivotal to reveal the role of the kinase in spontaneous excitatory and inhibitory synaptic activity, which are tightly connected to impaired spatiotemporal dynamics in the CA1 pyramidal neurons. The disruption of these microcircuitry negatively impacts on learning and memory abilities (Tang *et al*, 2017a).

Overall, MEMRI allowed us to select a few predefined cerebral regions in which to focus our next ^{1}H-MRS analyses. Indeed, we performed ^{1}H-MRS in hippocampus, which was strongly reactive in MEMRI, and thalamus, which presented a good but not significant increase in the manganese uptake. *In vivo* Magnetic Resonance Spectroscopy identified a defective neurochemical profile of those metabolites related to neurotransmission, as glutamine, but also in energy homeostasis, such as total creatine, total choline and N-acetyl-aspartate.

It is important to highlight that the metabolites are interconnected by their production and consumption and ^{1}H-MRS gives insight into the whole chemical composition of the

selected brain regions. Interestingly, increased glutamine levels together with creatine and choline drop have already been associated with deficits in memory and cognitive functions (Jadavji *et al*, 2017; Maurer & Williams, 2017). In addition, ^{1}H-MRS suggested the existence of an energy metabolism defect. In fact, it exists a connection between glutamine cycle and Nrf2 activation, a downstream gene of AMP-activated protein kinase (AMPK) pathway involved in antioxidant production that can influence intermediary metabolism and mitochondrial function (Mitsuishi *et al*, 2012). Mitochondrial involvement was also suggested by low levels of N-acetyl-aspartate.

Mitochondria are crucial organelles finely regulated to ensure ATP production and antioxidant defence and their dysfunctions have already been demonstrated in neurodevelopmental disorders, including Rett syndrome and, very recently, CDD (Castora, 2019; Siddiqui *et al*, 2016; Shulyakova *et al*, 2017; Van Bergen *et al*, 2021; Jagtap *et al*, 2019). I corroborated these results by demonstrating, in the adult *Cdkl5* KO hippocampus (P70), a profound drop in the ATP amount, that seemed to be mostly related to a failure in the OXPHOS activity since no alteration was noticed in the mtDNA/nDNA ratio (Carli *et al*, 2021). Accordingly, we measured impaired levels of Complex IV subunits, both at the transcriptional (nuclear gene *Cox7b*) and protein (mitochondrial encoded protein Mtco1) levels. These results were subsequently confirmed by a study on human patient-derived iPSC with a pathogenic truncating mutation (p.Arg59*)(Van Bergen *et al*, 2021). Of relevance, to support our hypothesis that Cdkl5 might exert a prominent effect in hippocampus, and since it is commonly recognised that mitochondrial homeostasis could be variable across different cerebral regions (Burtscher *et al*, 2015; Petersen *et al*, 2019), we extended our investigation to cerebral cortex and thalamus. While no impairment was found in the cerebral cortex, we reported a consistent decrease in Complex IV subunit expression in thalamus, thus implying the relevance in future studies to further explore this brain area.

To investigate whether the observed dysregulated expression of Mtco1 was associated with a defective Complex IV activity, we performed High Resolution Respirometer assay, confirming a profound failure in Complex IV respiratory capacity in the hippocampus of KO animals. Importantly, Complex IV activity is coordinated by the ATP/ADP ratio and it can adapt ATP synthesis to the energetic cellular necessities (Ludwig *et al*, 2001). Although supported from other recent findings that reported altered levels and function

of Complex IV in both human CDD iPSC and in another *Cdkl5* mouse model (Van Bergen *et al*, 2021; Vigli *et al*, 2019), we are aware that further investigations directly measuring the single complex activity are required.

Importantly, mitochondria provide 90% of the ATP that the brain mostly uses to support synaptic transmission, a very energy-demanding process (Harris *et al*, 2012). Affected ATP levels led us to focus on the AMPK, which represents the crucial sensor hub of the cell. Indeed, when ADP/ATP ratio increases, AMPK gets phosphorylated to respond with increased ATP generation at the expense of ATP consumption (Herzig & Shaw, 2018). A previous work already demonstrated that AMPK phosphorylation was altered in a different mouse model of *Cdkl5*; the authors speculated that Cdkl5 has a pivotal role in coordinating multiple signalling cascades (Wang *et al*, 2012b). Remarkably, we uncovered that at P70 AMPK phosphorylation is specifically faulty also in the *Cdkl5* KO hippocampus of the herein used mouse model of CDD, thus suggesting its inability to sense ATP decreased levels and face energy demand.

A longitudinal study, from an early age (P10) to adulthood (P70), confirmed that P70 is the time point at which the mitochondrial defect is mostly preponderant. Thus, we decided to perform a pharmacological treatment before the onset of the mitochondrial impairment. We chose a drug able to target AMPK and, given its relevance in many crucial pathways including the transcriptional coactivator peroxisome proliferator-activated receptor-λ coactivator 1-α (PGC-1α) and fatty acid oxidation (β-oxidation)(Garcia & Shaw, 2017), we searched for a treatment able to indirectly stimulate its activation by increasing intracellular AMP:ATP ratios. Based on the therapeutic efficacy proved in different neurodevelopmental disorders, including a female mouse model of Rett syndrome (Peralta *et al*, 2020; Yuen *et al*, 2021; Zuliani *et al*, 2020), we elegised the dimethylbiguanide Metformin, that was proved not only to enhance mitochondrial function though AMPK, but also through pathways related to mitochondrial biogenesis (e.g. PGC-1α/Nrf2)(Hardie *et al*, 2012; Zuliani *et al*, 2020). We reasoned that Metformin might thus represent an innovative and repurposable therapeutic strategy.

Although its actual mechanism of action is currently under investigation, the inhibition of Complex I of the ETC is believed to be a fundamental step in its action (Foretz *et al*, 2014; Vial *et al*, 2019), as the inhibition of rapamycin complex 1 (mTORC1), via AMPK-

dependent as well as AMPK-independent pathways (Mehrabi *et al*, 2018). Importantly, we proved that a 20 days long treatment (daily i.p., 100mg/kg) rescued in *Cdkl5* KO mice different behavioural defects. In fact, treated mice spent more time in digging marbles in Marble test, reverting their low interest in general environment, already recapitulated in other studies (Gennaccaro *et al*, 2021; Terzic *et al*, 2021). On the same line, Metformin treatment attenuated the locomotor hyperactivity observed in KO untreated animals in the Open field test while no consistent effect was found in the Novel Object Recognition test.

At the molecular level, we found that metformin reached the hippocampus and acted on its target, thus abolishing the defective phosphorylation of AMPK. Remarkably, by investigating whether Metformin could modulate cytoplasmic or mitochondrial AMPK, we noticed that only cytoplasmic AMPK levels were deregulated and rescued. Importantly, Metformin effect was barely maintained 10 days after the end of the treatment, thus suggesting the need of a chronic administration of the drug. In the next future it will be crucial to optimize the time window of the treatment, including the best time point in which to start the pharmacological administration.

Further, we will measure ATP levels of treated mice, together with other effectors of the AMPK pathway, such as PGC-1α and their downstream Nrf2 and Nrf1, which are fundamental in the expression of antioxidants and mitochondrial homeostasis maintenance. We are also aware that different drugs might give a stronger beneficial effect and we are considering the use of direct activators of AMPK, as the 5-aminoimidazole-4-carboxamide ribonucleotide (AICAR), an AMPK agonist and activator of PGC-1α (Habib *et al*, 2016). Likewise, it was reported that AICAR has a beneficial effect on defective cytochrome C oxidase (Complex IV)(Viscomi *et al*, 2011).

7.2 MRI unveils relevant differences in brain growth and development of different mouse models of Rett syndrome

MeCP2 is a multifunctional protein having a pivotal role as transcriptional regulator (Skene *et al*, 2010; Lagger *et al*, 2017; Shah & Bird, 2017) and our laboratory contributed to link its expression to brain development. Indeed, the lack of Mecp2 in the early stages of neuronal maturation deeply affects the morphology of neurons and their responsiveness to external stimuli (Bedogni *et al*, 2016; Scaramuzza *et al*, 2021). As a

consequence, we considered it relevant to investigate whether brain morphology and anatomical development could be influenced by *Mecp2* deficiency.

Animal models are a powerful instrument to understand the molecular consequences of *Mecp2* deficiency, and full knockout mice represent the mostly used model for Rett studies so far. Although they well mirror the principal characteristics of the disorder (Guy *et al*, 2001), over 600 distinct pathogenic mutations have been described in patients which do not involve the complete deletion of the gene. Accordingly, the type of *MECP2* mutation is one of the main causes of the high phenotypic variability of RTT patients, that manifest symptoms with a diverse degree of severity (Neul *et al*, 2010; Cuddapah *et al*, 2014; Vashi & Justice, 2019). Hence, we consider it of high relevance to also use mouse models harbouring human pathogenic mutations in addition to *Mecp2* null animals. Indeed, it is well-recognized that compensatory mechanisms might emerge from the absence of Mecp2, thus masking the actual consequences of its loss (Skene *et al*, 2010). In addition, since *Mecp2* is located on the X chromosome, female patients are subjected to X-chromosome inactivation (XCI), a random process in which cells within RTT females are mosaic for the expression of the *MECP2* mutation (Ishii *et al*, 2001; Knudsen *et al*, 2006). The absence of XCI in males made hemizygous mice more advantageous to be employed in RTT studies, since they present a more consistent and earlier phenotype. Nonetheless, it is highly debated to use males to model a neurodevelopmental disorder that primarily affects females.

To overcome those limitations and identify common and different features that could be useful as measurable outcomes of a complex disease, we used and compared both genders of two different mouse models of Rett syndrome. By improving the experimental MRI set up used in the *Cdkl5* mouse, we longitudinally analysed a full knockout, the *Mecp2*$^{tm1.1Bird}$ (Guy *et al*, 2001), and a knockin mouse developed in our laboratory, the *Mecp2*-Y120D, who carried a pathogenic mutation of a Chinese RTT patient (Inui *et al*, 2001; Gandaglia *et al*, 2019). We recently compared these two mouse lines in a work in which I appeared as co-author, unveiling a comparable phenotype in behavioural tests; however, at the molecular level opposite phenotypes were observed. Indeed, the Y120D mutation reduces Mecp2 binding to chromatin and its capacity to recruit corepressors on heterochromatin, while in the full KO the chromatin structure appears more condensed

and less prone to transcription, possibly because of compensatory mechanisms (Gandaglia *et al*, 2019).

We started by exploring the natural history of structural brain changes through morphological MRI. Imaging studies on RTT girls reported an overall reduction in brain volume with respect to healthy controls (Reiss *et al*, 1993; Armstrong *et al*, 1995; Carter *et al*, 2008; Chahrour & Zoghbi, 2007), that was corroborated also in mouse models (Chen *et al*, 2001; Guy *et al*, 2001; Williamson *et al*, 2012; Shahbazian *et al*, 2002). Microscopically, neuroanatomic investigations explained the decreased volume reporting smaller and more densely packed neurons and impaired dendritic growth in RTT samples compared to those of controls (Armstrong *et al*, 1995).

Our results well-fit with these reports and unveil that brain size is reduced from early time points in mutant animals of both genotypes. Morphological MRI on males showed that WT, KO and KI mice share a similar growth trajectory of the overall brain, even if mutant animals never reach the cerebral size of the WT counterparts. Female mice, whose longitudinal study was performed in a delayed time window, demonstrated that WT brain stopped its overall growth during adulthood; Y120D females reproduced this trend, while P200 *Mecp2*$^{+/-}$ heterozygous females from the null line displayed a volume reduction that could be related to degeneration/atrophy or, alternatively, to a premature senescence.

If brain shrinkage is consistently described in mouse models of Rett syndrome, regional size measurement reported divergent results. An investigation by Saywell and colleagues showed a shrinkage in motor cortex and corpus callosum and a tendency to reduction in the cerebellum of *Mecp2* KO mice (Saywell *et al*, 2006); a few years later, cerebellar and motor cortex decreased size of P20 KO mouse was reported to disappear at P40, speculating the presence of a temporary delay in the development of selected brain portions, that has a long-lasting effect on the growth of others (Ward *et al*, 2008); another complex *ex vivo* MRI study performed on both genders of two types of full knockout *Mecp2* mice and the knockin *Mecp2*^{308} unveiled a consistent decrease of motor, somatosensory and cingulate cortices, corpus callosum, striatum, hippocampus, pons and medulla at P60 and P200 (Allemang-Grand *et al*, 2017).

To obtain a more solid indication of the anatomical defect, MRI in combination with a novel semi-automated atlas-based registration (ANTx2) was used to segmentate and measure more than 800 brain structures and better understand how cerebral regions may

evolve *in vivo*, in early and mature animals. Importantly, our MRI analysis has advantages with respect to previous studies. In fact, Saywell et al. used KO mice spanning between 5 and 8 weeks of life, thus masking possible differences due to a large time window of analysis, while Allemang-Grand performed MRI on *ex vivo* brains, a procedure in which PFA fixation could affect the precision of the results (Saywell *et al*, 2006; Allemang-Grand *et al*, 2017).

We found an overall volume reduction of several anatomical structures. In particular, cerebral cortex, hippocampus and brainstem appeared consistently smaller in all mutant mice, independently from the *Mecp2* mutation. Remarkably, behavioural and morphological defects associated with those brain structures have been already reported in the RTT field. In detail, memory and cognitive deficits related to cerebral cortex and hippocampus are frequently observed in both patients and mice (Moretti *et al*, 2006; Sceniak *et al*, 2016; Hao *et al*, 2015), whereas brainstem impairment is responsible for autonomic disturbances such as breathing difficulties, one of the principal causes of death in RTT (MacKay *et al*, 2017; Kida *et al*, 2017). Of note, immaturity of the brainstem of Rett girls was already reported and associated with sympatho-vagal imbalance that led to wide pupils, chronic constipation and cold extremities (Julu *et al*, 1997; Julu & Witt Engerström, 2005). Noticeably, in the next future it will be interesting to parallel those atrophic regions to molecular and functional impairment in our mouse models.

Apart from common features, crucial genotype-related differences in regional absolute size were found, thus reflecting a diverse development of single brain structures in relation to the *Mecp2* mutation. For example, entorhinal and somatosensorial portions of the cerebral cortex are mainly responsible for the cerebral cortex atrophy in KO males, while in the KI brain prefrontal, visual, somatomotor and somatosensorial cortices are the most affected ones. On the other hand, female mutant mice displayed shrinkage of all the sub-structures of the cerebral cortex. However, while the defects were evident since P90 in HET-KI, HET from the null line manifested the same defects only at P200. Our results added novel insight about how the presence of a missense mutation diversely affects the brain development with respect to the complete loss of the gene. In support to our data, a very recent study from our laboratory provided evidence of the temporal effect of *Mecp2* loss on cortical thickness in both genders of *Mecp2*$^{tm1.1Bird}$ mice and suggested that

atrophy of astrocytes could contribute to the observed defect, opening new avenues for future studies (Albizzati *et al*, 2022).

The representation of relative brain volumes gave additional indications of how diverse cerebral structures contribute to brain atrophy. We mostly focused on the cerebral cortex, hippocampus and cerebellum, brain regions found to be deeply affected by *Mecp2* deficiency. In detail, we found that the cerebral cortex and the hippocampus are significantly smaller than controls at later time points of analysis, while cerebellum has a relative volume comparable to those of WT. When we focused on the growth trajectory of these brain regions, different trends having genotype-dependency were noticed. By following cerebral cortex development of WT and mutant males starting from P20, we unveiled that it reached its plateau at P30. Nonetheless, although having the same trend, KO males remained underdeveloped with respect to controls. Interestingly, a similar pattern was noticed in KI animals, that however showed a significant atrophy in the visual cortex at P40. By analysing the secondary structures of the hippocampus, KO showed developmental stagnation in the CA3 field, while KI presented a negative slope of the curves in all the observed portions, highlighting again a stronger atrophy than in the KO line. In females, the growth trajectory of the cerebral cortex and hippocampus maintained a plateau state from P60 to P200 in WT controls, while mutant females showed a decrease in brain volume at the last point of analysis, which strengthened the hypothesis of premature ageing. On the contrary, growth trajectory of the cerebellum in all animals perfectly matched at any time point of analysis, thus supporting that *Mecp2* deficiency has a specific regional influence. In support of our results, Kauffman and colleagues already discussed about brain development stagnation in *Mecp2* samples, by demonstrating an increased MAP2 staining in different layers of the cerebral cortex in WT controls but not in 6 years old RTT post-mortem samples and in a rat model of the disease (Kaufmann *et al*, 2005; Kaufmann & Moser, 2000; Colantuoni *et al*, 2001; Naidu, 1997). In addition, given its role in chromatin compaction, it was proposed that the decreased expression of *Mecp2* triggers senescence, together with an impairment in proliferation capacity, a reduction of the autophagy flux and an accumulation of DNA damage foci (Squillaro *et al*, 2012; Alessio *et al*, 2018). In the next future, we will use different approaches of molecular biology to compare the level of expression of several

markers of senescence and neurodegeneration in WT and RTT mice, with a special interest in female animals and mainly focusing on hippocampus and cortex.

Neuroanatomical results prompted us to select hippocampus and cerebellum for subsequent ^{1}H-MRS analysis, as an example of a strongly and a slightly affected brain region, respectively. Magnetic spectroscopy failed to identify a common deregulated metabolite, although phosphocreatine (PCr) was more consistently impaired among the diverse experimental groups. As already discussed, PCr is tightly related to the brain ATP metabolism and its loss well-fit with several reports of mitochondrial deficit in Rett syndrome (Shulyakova *et al*, 2017; Dave *et al*, 2019; Zuliani *et al*, 2020). A general overview of ^{1}H-MRS data underlined that the hippocampus of mutant animals also displays a deregulation of metabolites related to neurotransmission, such as glutamine, GABA and glutamate-to-glutamine ratio. Our results are in line with those found by Viola and colleagues in NMR spectroscopy, in which emerged an overlapped increase in glutamine levels together with a drop in GABA concentration (Viola *et al*, 2007; El-Khoury *et al*, 2014). Remarkably, the balance between glutamate, glutamine and GABA needs to be finely regulated to ensure a correct E/I equilibrium and the consequent control of learning, memory and cognitive functions (Rubin *et al*, 2017). Otherwise, glutamine is a necessary metabolic fuel for ATP production (Newsholme *et al*, 2003; Großer *et al*, 2012). In concert with that, high glutamate levels measured in the cerebrospinal fluid of RTT girls are often interpreted as boosted glucose utilization, thus creating a link between neurotransmission and energy homeostasis (Colantuoni *et al*, 2001).

Consistently with the study of Saywell and colleagues in full knockout mice (Saywell *et al*, 2006), in the cerebellum we also found a consistent reduction of NAA levels at the pre-symptomatic stage of the disease in both genders of null animals, together with impaired inositol levels selectively in the KO mouse.

Altogether our results added important evidence of the brain development of diverse mouse models of Rett syndrome. Although we are aware that this is only a starting point for further analysis and that modification in regional or total brain size can be due to a combination of numerous factors, we think that the identification of which *Mecp2* deficient brain regions mainly suffer from atrophy could be a useful biomarker with a high translational value. With the addition of biochemical, histological and behavioural information we might also reveal novel important findings useful to explain the molecular

consequence of *Mecp2* deficiency and/or to obtain biomarkers. Furthermore, the similar but not overlapping phenotype observed in the different mouse models depending on gender and *Mecp2* mutation strengthen the importance of including in Rett studies female mice together with different mouse models of *Mecp2*. As previously proposed by us (Gandaglia *et al*, 2019) this approach will permit to reveal whether therapy might have to be selected also considering the specific *Mecp2* lesion.

Considering all my results together, I confirmed MRI as a sensitive method for studying Rett syndrome and related disorders, capable of detecting overall changes both at the anatomical and metabolic levels. This approach permitted us to identify a promising and translational therapeutic approach for CDD and to obtain new insights of the anatomical development of RTT mice.

8. Material and Methods

The procedures employed for the results obtained in chapters *6.1.1, 6.1.2, 6.1.3, 6.2.1* (MRI approaches, ATP measurement, qPCR and Western Blots) have been published in a work of which I appeared as first author (Carli *et al*, 2021).

8.1 Animals

All procedures were accomplished in accordance with the European Community Council Directive 2010/63/UE for care and use of experimental animals with protocols approved by the Italian Government (decrees No. 210/2017-PR and 175/2015-PR) and the San Raffaele Scientific Institutional Animal Care and Use Committee.

The mouse lines were housed in the animal facility of the San Raffaele Scientific Institute. For the experiments on *Cdkl5*, mice derived from the *Cdkl5* null mouse strain described in Amendola et al. (Amendola *et al*, 2014), a conventional knock-out lacking exon 4. For the experiments on *Mecp2*, mice derived from the *Mecp2* null mouse strain described in Guy et al. (Guy *et al*, 2001), while the *Mecp2* knockin Y120D mouse line was generated in our laboratory as described in Gandaglia et al. (Gandaglia *et al*, 2019). The animals' strains were generated on a C57BL/6J background. However, in accordance with our recent work that described the advantages of using CD1 background (Gigli *et al*, 2016), mutant males, heterozygous females and wild-type (WT) controls of this study were obtained by crossing C57BL/6J heterozygous females with CD1 WT male mice purchased from Jackson Laboratories and then backcrossed and maintained on a clean CD1 background. This backcrossing strategy occurred for more than 10 generations. The generated lines recapitulate the behavioural phenotypes exhibited by the same lines maintained on an inbred background. These animals have already been cited in a few recent publications (Gandaglia *et al*, 2019; Balestra *et al*, 2019; Scaramuzza *et al*, 2021; Carli *et al*, 2021). Mice were housed in groups of five in Tecniplast cages, on a 12 h light/dark cycle in a temperature-controlled environment (21 ± 2 °C) with food and water provided *ad libitum*.

8.1.1 Genotyping

Mice genotypes were analysed by Polymerase Chain Reaction (PCR) on genomic DNA purified from ears. Each sample was dissociated in Tail Lysis Buffer (Tris 100 mM, EDTA 10 mM, SDS 0.5%, NaCl 100 M) + Proteinase K (25 mg/mL, Genespin, #STS-OK500) at 55°C O/N. The day after 400 µL of 100% isopropanol were added to the supernatants and DNA was precipitated (13,000 rpm, 10 min). Supernatants were carefully eliminated, pellets were washed with 500 µL of 70% EtOH and then centrifuged at 13,000 rpm for 5 min. EtOH was discarded, pellets were dried at RT and resuspended in 200 µl of TE (10 mM Tris, 1 mM EDTA; pH 8) for DNA quantification with a spectrophotometer (NanoDrop 1000, ThermoFisher).

Table 8. PCR reaction mix for *Mecp2*-null and -Y120D mice genotyping

Reagents	**Concentration**	**Final volume *Mecp2*-null**
H_2O	-	12.6 µL
Xtra RTL GL Reaction Buffer (Genespin, #XSTS-T5XRTL)	5 X	4 µL
dNTPs (Promega, #U120A;U121A; U122A;U123A)	10 µM	0.4 µL
Reverse primer	10 µM	0.5 µL
Forward primer (WT allele)	10 µM	0.5 µL
Forward primer (null allele)	10 µM	0.5 µL
XtraTaq Pol RTL (EUROCLONE, #EME010001)	5 U/µL	0.5 µL
DNA	100 ng	1 µL

Reagents	**Concentration**	**Final volume *Mecp2*-Y120D**
H_2O	-	12.6 µL
Xtra RTL GL Reaction Buffer (Genespin, #XSTS-T5XRTL)	5 X	4 µL
dNTPs (Promega, #U120A;U121A; U122A;U123A)	10 µM	0.4 µL
Common forward primer	10 µM	0.5 µL
Common reverse primer	10 µM	0.5 µL
Reverse primer (KI allele)	10 µM	0.5 µL
XtraTaq Pol RTL (EUROCLONE, #EME010001)	5 U/µL	0.5 µL
DNA	100 ng	2 µL

Table 9. PCR reaction mix for *Cdkl5* mutant mice genotyping

Reagents	Concentration	Final volume *Cdkl5*
H_2O	-	13.84 µL
Xtra RTL GL Reaction Buffer (Genespin, #XSTS-T5XRTL)	5 X	4 µL
dNTPs (Promega, #U120A;U121A; U122A;U123A)	10 µM	0.5 µL
Reverse primer	100 µM	0.04 µL
Forward primer (WT allele)	100 µM	0.04 µL
Forward primer (KO allele)	100 µM	0.08 µL
XtraTaq Pol RTL (EUROCLONE, #EME010001)	5 U/µL	0.5 µL
DNA	100 ng	1 µL

Primers:

- For *Mecp2* KO:

common reverse primer: 5'- CCACCCTCCAGTTTGGTTTA–3′;

forward primer for the KO allele: 5'-ACCTAGCCTGCCTGTACTTT–3′;

forward primer for the WT allele: 5'-GACTGAAGTTACAGATGGTTGTG–3′;

- For *Mecp2* KI:

common forward primer: 5′–CAGGGCCTCAGAGACAAGC–3′;

common reverse primer: 5′–GCAGATCGGCCAGACTTCC–3′;

reverse primer for the KI allele: 5′–GGGTTAATTGATATCCAATTGGGATCC–3′.

- For *Cdkl5*:

common reverse primer: 5'-CTGTGACTAGGGGCTAGAGA-3';

forward primer for the KO allele: 5'-ACGATAGAAATAGACGATCAACCC-3';

forward primer for the WT allele: 5'-CCCAAGTATACCCCTTTCCA-3'.

Table 10. PCR cycles for genotyping

Step	*Cdkl5*	*Mecp2*-null	*Mecp2*-Y120D
Heat lid	110°C	110°C	110°C
Denaturation	94.0° C (4 min)	95.0° C (2 min)	95.0° C (2 min)
Start loop	33 X	35 X	35 X
denaturation	94.0 °C (40 sec)	95.0 °C (30 sec)	95.0 °C (30 sec)
annealing	59.0 °C (30 sec)	59.0 °C (30 sec)	60.0 °C (30 sec)
extension	72.0 °C (40 sec)	72.0 °C (30 sec)	72.0 °C (45 sec)
Close loop			
Final extension	72.0 °C (5 min)	72.0 °C (5 min)	72.0 °C (5 min)
Hold	8°C ∞	8°C ∞	8°C ∞

PCR samples were resolved by electrophoresis run in 2% agarose gel and the obtained PCR products are:

- For *Mecp2* KO: a single band of 458 base pairs (bp) for the *Mecp2*-KO mice and a single band of 411 bp for the WT animals. The presence of both fragments indicates the heterozygous genotype.
- For *Mecp2* KI: a 300 bp common fragment for WT and KI animals and an additional 550 bp fragment for the mutated one.
- For *Cdkl5*: a single band of 240 bp for WT animals and a single band of 344 bp for the KO. The presence of both fragments indicates the heterozygous genotype.

8.2 Magnetic Resonance Imaging

MRI experiments were conducted on a 7-Tesla scanner for rodents, fully equipped for brain MRI/MRS (Biospec, Paravision 6.0 Software Bruker-Biospin). A dedicated mouse head coil (4-channels) was used as receiver together with a volume coil as transmitter. For *in vivo* MRI, a mixture of IsoVet (isoflurane 1-2%; Zootecnica, #104331020) with oxygen was used to anaesthetize animals and breath rate was constantly monitored to regulate the level of anaesthesia. IsoVet is an inhalation anaesthetic frequently used for general anaesthesia in animals and, as a consequence, induction and recovery from anaesthesia are rapid. Body temperature of mice was maintained through warm water circulating inside the bed. For *ex vivo* MRI, fixed brains were placed over a support of agar gel (2%) and positioned under the mouse brain coil.

For cerebral anatomy analysis, T2 weighted MR images were acquired with coronal sections of 0.7 mm and an in-plane resolution of 83 µm (FOV = 16 mm) using a fast-spin-echo sequence (TR/TE = 3500/45 ms, rare factor = 8, average = 8, 11 minutes of acquisition). For *in vivo* MRI, T2-weighted images were acquired with a fast-spin-echo sequence (TR/TE= 3350-3500/44-45 ms, resolution of 73-76 µm, thickness of 0.65-0.7 mm, 9 averages, 9-12 minutes of acquisition).

As a first analysis, total brain volume was obtained from brain area segmentation using the image analysis tools from Paravision. A total of 10 (*ex vivo*) and 23 (*in vivo*) MR sections acquired along the brain were used. In *ex vivo* studies, olfactory bulbs and cerebellum were excluded from the analyses as they were partially damaged during brain

extraction procedures, while ventricles areas were subtracted from the total brain volume in *in vivo* MRI but not *ex vivo* analysis since ventricles were collapsed post-fixation. In addition, for all data obtained *in vivo*, we also performed a second analysis on T2-weighted images using a MATLAB toolbox, the Atlas Normalization Toolbox using elasti X (ANTX, https://github.com/ChariteExpMri/antx2) which allows to extract the cerebral volume of the different brain areas following the Allen Mouse Brain Atlas (http://mouse.brain-map.org/). The whole procedure was completed following the guidelines described in Koch et al. (Koch *et al*, 2019). Animals whose fitting in the segmentation was not optimal were excluded from this analysis (n = 1 KO P20; n = 1 HET-BIRD P90; n= 1 HET-KI P200). Because of technical issues during the acquisition some animals of the *Mecp2*-Y120D female lines were not analysed (n = 1 WT P60; n= 2 KI P60; n = 2 WT P200; n = 1 KI P200). Single brain region volume was then compared to the total brain volume of each mouse and multivariate statistical analyses on volumetric data sets were performed using the web-based platform MetaboAnalyst (www.metaboanalyst.ca) with "Statistical Analysis [one factor]" as module of analysis. Autoscaling was applied to the data set prior to performing Partial Least Squares Discriminant Analysis (PLS-DA). Successively, cerebral regions contributing most to group separation were defined from the VIP (variable importance for the projection) scores >1.2 (Xia & Wishart, 2011).

8.2.1 Manganese Enhanced MRI

$MnCl_2$ was administered as an intraperitoneal injection (60 mg/kg; pH 7.4, Sigma-Merk, #7773-01-5) 24 h before the sacrifice. Manganese ion (Mn^{2+}) is a paramagnetic agent able to produce MR contrast by causing a reduction in the T_1 relaxation times of water (Duong *et al*, 2000; Itoh *et al*, 2008; Silva & Bock, 2008). For all the experimental groups, a control mouse of the corresponding gender (blank) was treated with an equal dose of sodium chloride (0.9% NaCl) and used as reference for manganese uptake quantification. *Mecp2* mice were imaged at P40 and P150 (for males and females, respectively), while *Cdkl5* mice were imaged at P70 and P150 (for males and females, respectively). The day after manganese treatment, animals were deeply anesthetized by a single intraperitoneal injection of Avertin (250 mg/Kg, Sigma-Aldrich, #T48402) and transcardially perfused with 100 mM PBS pH 7.4, followed by 4% paraformaldehyde

(PFA). The brains were carefully removed from the skull, kept in 4% PFA for 24 h and then conserved in 100 mM PBS supplemented with 0.02% sodium azide for one week before MRI acquisition. The use of Avertin followed approval of the experimental protocols by the Italian Government (decrees No. 210/2017-PR, 175/2015-PR and 1172/2020-PR).

To quantify manganese uptake, a map of the longitudinal relaxation time T1 was acquired using a spin-echo sequence with different recovery times (n = 6, 290 to 4000 ms, TE= 6.65 ms, 49 minutes of acquisition) and a resolution of 103 μm with sections similar to T2 weighted images (0.7 mm of thickness). The complete MRI exam lasted 80 minutes for each sample. Maps of T1 were calculated using the mono exponential fitting tool of Paravision. The contrast enhancement of manganese was calculated as the percentage of relaxivity (R1 = 1/T1) differences versus blank mice. Manganese uptake was measured in the cerebral regions of interest (ROIs) identified through the reference atlas from Allen Institute for Brain Science (http://atlas.brain-map.org/).

8.2.2 Magnetic Resonance Spectroscopy (^{1}H-MRS)

Cerebral metabolites were measured *in vivo* using ^{1}H-MRS on *Mecp2* mice at different ages and on *Cdkl5* mice at P70. A PRESS sequence (TR/TE = 2000/16.1 ms) was used with the selection of a voxel in different cerebral areas: the hippocampus (3.96 - 4.96 mm^3), the cerebellum (9.72 mm^3), the thalamus (5.13 mm^3) and the prefrontal cortex (3.2 - 4.56 mm^3) with water-suppression (VAPOR). The signal was accumulated 200-400 times according to the brain region (7 -13 minutes of acquisition). For each area, magnetic field homogeneity was optimized through the use of automatic map-shim calculation from a B0 map initially acquired. A spectrum without water suppression was also acquired and used as internal reference for metabolites concentration calculation using the LCModel program (http://s-provencher.com/lcmodel.shtml)(Provencher, 2001).

All acquired spectra were obtained with a suitable signal to noise ratio allowing the quantification of more than 12 metabolites. Metabolites with an estimated standard deviation (Cramer-Rao lower bounds, %SD) higher than 27% were excluded.

8.3 RNA Purification, cDNA Synthesis and quantitative RT-PCR

Cdkl5 mutant mice and WT littermates (P70) were sacrificed by dislocation and brains were rapidly removed. Hippocampus was dissected out and immediately frozen on dry-ice and conserved at -80°C until analysis. Total RNA was extracted using Purezol (Bio-Rad, #7326890) and mechanical trituration of the tissue was performed using a Potter-ELV glass grinder. Samples were incubated for 5 minutes at RT and 100% chloroform (Sigma-Merk, #372978) was added 1:5 (200 µL/1 mL PureZOL). Then, samples were manually inverted to gently mix the phenol:chloroform mixture and following 2 minutes of incubation at RT they were centrifuged (12,000 g, 15 min, 4°C) to separate aqueous and organic phases. The upper aqueous phase was collected and RNA was precipitated with 100% isopropanol 1:2 (500 µL/1 mL PureZOL) O/N at -20°C. The next day, samples were centrifuged for 10 min at 12,000 g (4 °C); supernatant was discarded and the RNA pellets obtained were washed in 500 µL of 70% EtOH and re-precipitated for 10 min of centrifugation at 7,500 g (4 °C). After the removal of the supernatant, pellets were air dry for 5 min before resuspension in 15 µL of RNAse-free H_2O and stored at – 80°C.

RNA was quantified using a NanoDrop 1000 spectrophotometer and integrity verified by agarose electrophoresis. First strand cDNA was synthesized using the RT^2 First Strand Kit (Qiagen, #330404) as instructed by the manufacturer and used as a template for quantitative RT-PCR with SYBR Green Master Mix (Applied Biosystems, #4472908).

Table 11. Primers used for quantitative RT-PCR

Atp5a1	5'- GCCATCGTGGATGTCCCCGTTG-3'; 5'- CTTTCAGGCCCACTCGTCTGCG-3'	Nuclear encoded gene	ETC nuclear subunit (Complex V)
Cox-7b	5'-TTGCCCTTAGCCAAAAACGC-3'; 5'- TCATGGAAACTAGGTGCCCTC-3';	Nuclear encoded gene	ETC nuclear subunit (Complex IV)
Fis-1	5'- CGTGGGCAACTACCGGCTCAAG -3' 5'- CTGGGGCTCAGTCTGCAACAGC -3'	Nuclear encoded gene	Mitochondrial Fission Protein 1
Ndufv2	5'-GCAAGGAATTTGCATAAGACAGC-3'; 5'-TAGCCATCCATTCTGCCTTTG-3';	Nuclear encoded gene	ETC nuclear subunit (Complex I)
Opa-1	5'- TGGAAAATGGTTCGAGAGTCAG -3'; 5'- CATTCCGTCTCTAGGTTAAAGCG -3';	Nuclear encoded gene	Optic Atrophy 1
Pgc-1α	5'- CATGCCTGACGGCACCCCTC -3'; 5'- AGCAGGGACGTCTTTGTGGCT -3';	Nuclear encoded gene	Peroxisome proliferator-activated receptor-γ coactivator
Sdha	5'- AGCAAGCTCCTGCCTCTGTGGT -3'; 5'- GCTCTGTCCACCAAATGCACGCT-3'	Nuclear encoded gene	ETC nuclear subunit (Complex II)

Timm23	5'-TTACTCGAACGCTGATTTGGC -3'; 5'- CTCGGGTTTTATTAGCTCCAG -3';	Nuclear encoded gene	Translocase Of Inner Mitochondrial Membrane 23
Tomm40	5'- TCCAGTTCAGATGGAAGGTGTCA -3'; 5'- TCGTCCCCACGTATGTGACCCC -3';	Nuclear encoded gene	Translocase of Outer Mitochondrial Membrane 40
Uqrc1	5'-AGACCCAGGTCAGCATCTTG-3'; 5'-GCCGATTCTTTGTTCCCTTGA-3'	Nuclear encoded gene	ETC nuclear subunit (Complex III)

All samples were analysed in triplicate and mRNA levels were normalized to *Hprt* (forward primer 5'- ACAGGCCAGACTTTGTTGGAT-3'; reverse primer 5'-TGCAGATTCAACTTGCGCTC-3') as internal standard. Fold change in gene expression was calculated using the 2(-ΔCt) method (Livak & Schmittgen, 2001).

8.4 Mitochondrial DNA analysis

For mitochondrial DNA (mtDNA) analysis, total genomic DNA was isolated from hippocampi of *Cdkl5* KO and corresponding WT controls. The tissues were digested in 200 µl of Digestion Buffer (50 mM Tris-HCl pH 8, 100 mM EDTA pH 8, 100 mM NaCl, 1% SDS) and Proteinase K (Genespin, #STS-OK500) O/N at 55°C. The next day, 200 µl of Phenol/Chloroform/Isoamyl alcohol (25:24:1, Sigma-Merck, #P3803) was added and samples were centrifuged at 13,000 g for 10 min (RT). The aqueous phase was drawn and 1:10 Vol of Sodium Acetate 3 M + 2.5 Vol µl of 100% EtOH was added. After 10 minutes of centrifugation at 13,000 g (RT), the supernatant was discarded. Pellets were resuspended in 100 µl of milliQ H_2O and let O/N at 55°C. Subsequently, mtDNA and nuclear DNA were measured by qPCR using primers for *CytB* (forward primer 5'-ACGCCATTCTACGCTCTATC-3'; reverse primer 5'-GCTTCGTTGCTTTGAGGTGT-3') and *Rnase P* (forward primer 5'-GAAGGCTCTGCGCGGACTCG-3'; reverse primer 5'-CGAGAGACCGGAATGGGGCCT-3'), respectively. DNA (20 ng/well) was mixed with SYBR Green Master Mix (Applied Biosystems, #4472908) and primers. The following formula: ΔCt = mean value of Ct(mDNA)/mean value of Ct(nDNA) was used in each sample and results are presented as a percentage of WT.

8.5 Protein extraction and Western Blot

8.5.1 Protein extraction

Cdkl5 mutant mice and WT littermates (P10, P40 and P70) were sacrificed by dislocation and brains were rapidly removed. Cerebral tissues (hippocampus, thalamus and cerebral cortex) were dissected out and immediately frozen on dry-ice and conserved at -80°C until analysis. Collected tissues were then homogenized in 300 (hippocampus and thalamus) or 500 (cerebral cortex) µl of RIPA buffer (100 mM Tris HCl pH 7.5, 300 mM NaCl, 10 mM EDTA, 2% NP-40, 0.2% SDS, 1% sodium deoxycholate) containing Protein Inhibitor Complex 1X (Sigma Merck, #P8340) and PhosSTOP (Sigma Merck, #4906845001). After 30 min on ice, samples were centrifuged at 12,000 g for 30 min (4°C), supernatants were collected and sonicated on ice for 10 s at 30 amplitudes. Proteins were then stored at -80°.

8.5.2 Mitochondrial isolation

After the Metformin treatment, we used an approach to separate mitochondrial and cytoplasmic fractions through a series of centrifugation. Frozen *Cdkl5* KO and WT hippocampi were homogenized in 300 µl of ice-cold Mito Buffer (70 mM Sucrose, 220 mM Mannitol, 5 mM KH_2PO_4, 5Mm $MgCl_2$, 1 mM EGTA, 2mM HEPES; pH 7.4) and then centrifuged at 1,000 g for 5 min to pellet nuclei (4°C). Supernatants were collected and centrifuged again (380 g for 5 min at 4°C) to remove contaminating nuclei. After a centrifugation at 10,000 g for 10 min (4°C), supernatants, that contain the cytosolic fraction, were collected and stored at −80°C. Pellets, which contain the mitochondrial fraction, were gently resuspended in 300 µl of Mito Buffer and centrifuged at 10,000 g for 5 min (4°C). This step was repeated twice before to resuspend mitochondrial proteins in 80 µl of RIPA buffer. Finally, mitochondrial fractions were stored at −80°C.

8.5.3 Western Blot

Protein concentrations were calculated using bicinchoninic acid (BCA) assay kit (Thermo Scientific, #23228); 30 µg of protein lysates were loaded onto TGX Stain-Free gel prepared by FastCast Acrylamide Kit (Bio-Rad, 10%: #1610183; 12%: #1610185) or using pre-cast gradient gels (Biorad, 4-15%, #5678084). Before transfer, a Stain-Free gel image was acquired by ChemiDoc Touch Imaging System (Bio-Rad) and used to quantify

results. Proteins were blotted on a nitrocellulose membrane (Trans-blot Turbo Nitrocellulose Transfer Packs, Bio-Rad Mini #1704159 and Bio-Rad Midi #1704158) using the Trans-blot SD (Bio-Rad) semidry apparatus. Membranes were incubated at RT for 1 h in blocking solution (Tris-buffered saline containing 0.1% Tween-20 (TBS-T) and 5% nonfat milk or 5% BSA [Sigma Merck, #A30659]) and then incubated O/N with the primary antibody diluted in the proper blocking solution (4°C). The following primary antibodies were used: anti-total OXPHOS (Abcam, #ab110413; 1:1000 in 5% BSA in TBS-T); anti-AMPK-alpha2 (Cell Signaling, #2532; 1:1000 in 5% milk in TBS-T); anti-phospho-AMPK-alpha2 (Thr172) (Cell Signaling, #2535; 1:1000 in 5% milk in TBS-T). After 3 washes in TBS-T, blots were incubated with the appropriate HRP-conjugated secondary antibody (Peroxidase-conjugated AffiniPure Goat anti-mouse or rabbit IgG (H+L), mouse #115-035-003, rabbit #111-035-144, Jackson ImmunoResearch) diluted in blocking solution. Immunocomplexes were visualized using the ECL substrates kits from Cyanagen and the Bio-Rad ChemiDoc^{TM} System. Quantification of bands was performed using the Image Lab 5.2.1 Software.

8.6 ATP measurement

A luminescence assay (CellTiter-Glo Luminescent Cell Viability Assay, Promega, #G7570) was used to measure the ATP content (Chida *et al*, 2012) in *Cdkl5* KO mice and WT littermates. Frozen tissues (hippocampus, thalamus and cerebral cortex) were mechanically homogenized with a Potter-ELV glass grinder in 300 µl of cold Lysis Buffer (0.25 M sucrose, 10mM HEPES-NaOH pH 7.4), and then cleared by centrifugation at 1,000 g for 10 min (4°C). Then, 250 µl of supernatant were collected and added to an equal volume of ice-cold 10% trichloroacetic acid (TCA). Samples were manually inverted for 20 sec and then centrifuged at 10,000 g for 10 min (4°C). Afterwards, 400 µl of supernatant was collected and neutralized by adding 200 µl of Tris-acetate buffer (1M; pH 8). Following a 10-fold dilution with deionized H_2O, the extracts were used for the luciferase-luciferin assay. The reaction mix, containing luciferase and substrate, was added and the light emission was calculated through a GloMax luminometer (Promega). ATP content was quantified in accord with an ATP standard curve.

8.7 High Resolution Respirometry (HRR)

8.7.1 Cryopreservation

Cdkl5 mutant mice and WT littermates (P70) were sacrificed by dislocation and brains were quickly removed. Hippocampi were washed in ice-cold modified MIR05 medium (0.5mM EGTA, 3mM $MgCl_2$•$6H_2O$, 60mM MOPS, 20mM taurine, 10mM KH_2PO_4, 20mM HEPES, 110mM sucrose, 1 g/L BSA; pH 7.0) to wash out excess blood. Then, hippocampi were immersed in cryotubes containing 1 mL of ice-cold modified University of Wisconsin solution (Sakata *et al*, 1997)(20mM histidine, 20mM succinate, 3mM glutathione, 1 μM leupeptin, 2mM glutamate, 2mM malate, 2mM ATP, 0.5mM EGTA, 3mM $MgCl_2$•$6H_2O$, 60mM MOPS, 20mM taurine, 10mM KH_2PO_4, 20mM HEPES, 110mM sucrose, 1 g/L BSA and 10% (v/v) DMSO). Afterwards, following the protocol of García-Roche (2018), a sequential freezing method of cryopreservation was performed to preserve cellular function. Before cryopreservation 10% (v/v) DMSO (Sigma-Merk, #D8418) was added to each cryovial. Samples were left 6 min on ice and then moved to a canister and placed at the neck tube of a liquid nitrogen tank for 10 min, where they were exposed to nitrogen vapors at −110 °C. In the last step of the protocol, samples were submerged in liquid nitrogen (approximately −196 °C) for 10 min. Hippocampi were stored at -80°C.

8.7.2 High Resolution Respirometry

High Resolution Respirometry on *Cdkl5* KO and WT hippocampi was performed to measure cellular oxygen consumption. The respiration rates of hippocampi were measured into the O_2K oxygraph chambers (Oroboros, Instruments Oroboros, Innsbruck, Austria) at 37°C in the respiration medium MiR06 (0.5 mM EGTA, 3 mM $MgCl_2$, 60 mM K-lactobionate, 20 mM taurine, 10 mM KH_2PO_4, 20 mM HEPES, 110 mM sucrose and 1 g/l bovine serum albumin fatty acid-free, 280 U/ml catalase; pH 7.1). Substrates, uncouplers and inhibitors were injected in the chambers to assess the mitochondrial respiration. In detail, Pyruvate (5 mM) and Malate (2 mM) are injected to obtain state 2 of the respiration. Then saturating concentrations of ADP were added (2.5 mM) to induce the complex I maximal OXPHOS capacity (state 3). To test the integrity of the outer mitochondrial membrane Cytochrome C (10 μM) was injected. Subsequent titration of Succinate (10 mM) allows to obtain state 3 by convergent electron flow from complexes

I and II and gives information about the CI and CII maximal OXPHOS capacity (state 3+S). Uncoupled complex-II-linked respiration was achieved by the addition of Rotenone (0.5 μM) (state3 + Succ + Rot). Subsequently, the respiratory chain was inhibited by Antimycin A (2.5 μM) and Malonate (5mM) to measure the residual oxygen flux. CIV activity was promoted by TMPD (0.5 mM) and Ascorbate (2 mM) addition. Oxygen fluxes were corrected by subtracting residual oxygen consumption from each steady state. For data acquisition and analysis DatLab software (Oroboros, Instruments Oroboros, Innsbruck, Austria) was used.

8.8 Pharmacological treatment

Metformin (met-1,1-Dimethylbiguanide; Sigma-Aldrich #150959) was dissolved in saline (0.9% NaCl) and daily administered to *Cdkl5* KO and WT littermates, according to the mouse weight (intraperitoneal injection; 100 mg/kg). Animals were randomly assigned to receive Metformin or saline and a 20-day long treatment (from P55 to P75) regimen was carried out by an operator blind to genotype and treatment. To evaluate Metformin effects on typical behavioural phenotypes of *Cdkl5* null mice, experimental mice underwent a battery of tests after 10 and 20 days of treatment. To assess persistence of drug effects, in a small cohort of mice tests were also performed 10 days after the last administration of Metformin. At the end of behavioural tests, mice were sacrificed by dislocation and cerebral regions were collected and stored at -80°C for subsequent molecular analyses.

8.8.1 Open field

Exploratory behaviour and general locomotor activity were assessed through Open field test. Each animal was removed from its home cage by the tail and individually placed directly into the centre of the open field. Tests lasted 10 minutes. Total distance travelled (cm) was used as a measure of locomotor activity with the EthoVision 14 (Noldus) software, while unsupported rears were measured as anxiety-specific behaviour.

8.8.2 Marble-burying test

The Marble-burying test evaluates autistic features and general environment interest. Each mouse was individually placed in a cage with 5 cm of standard bedding material.

Twelve glass marbles (19 mm) were uniformly distributed on the top of the bedding in a matrix of 4 rows of 3 marbles. Animals were allowed to explore for 30 min and at the end of the test the number of marbles that were at least two-thirds buried were counted.

8.8.3 Novel Object Recognition (NOR)

The Novel Object Recognition test investigates learning and memory. Trial is divided into 2 steps. For the training session each animal was placed into the arena with two identical objects for 5 min. After 4 h, during the test session, one of the training objects was replaced with a novel object. Since mice have an innate preference for novelty, they should spend most of the time at the novel object rather than the familial one. Time spent exploring each object was scored by an experimenter and subsequent the discrimination index (DI) was calculated as follows: (time exploring the novel object – time exploring familiar object)/total object exploration time.

8.9 Statistical analysis

Before any statistical analysis, normal distribution of data was assessed by applying the D'Agostino-Pearson normality test. In accordance with data distribution, statistical significance for multiple group comparisons was determined by One- or Two-Way Analysis of Variance (ANOVA), followed by post hoc tests. Unpaired Student's t-test or Mann–Whitney test were used for two group comparisons. ROUT test (Q=1%) was applied to establish the presence of outliers. Statistically significance was expressed as: *p < 0.05; **p 0.01; ***p 0.001; ****p < 0.0001 and all the reported data were expressed as mean ± SEM. Statistical analyses were performed using Prism 9 (GraphPad Software, CA).

9. References

Achilly NP, He LJ, Kim OA, Ohmae S, Wojaczynski GJ, Lin T, Sillitoe R V., Medina JF & Zoghbi HY (2021) Deleting mecp2 from the cerebellum rather than its neuronal subtypes causes a delay in motor learning in mice. *Elife*

Alessio N, Riccitiello F, Squillaro T, Capasso S, Del Gaudio S, Di Bernardo G, Cipollaro M, Melone MAB, Peluso G & Galderisi U (2018) Neural stem cells from a mouse model of Rett syndrome are prone to senescence, show reduced capacity to cope with genotoxic stress, and are impaired in the differentiation process. *Exp Mol Med*

Allemang-Grand R, Ellegood J, Spencer Noakes L, Ruston J, Justice M, Nieman BJ & Lerch JP (2017) Neuroanatomy in mouse models of Rett syndrome is related to the severity of Mecp2 mutation and behavioral phenotypes. *Mol Autism*

Amendola E, Zhan Y, Mattucci C, Castroflorio E, Calcagno E, Fuchs C, Lonetti G, Silingardi D, Vyssotski AL, Farley D, *et al* (2014) Mapping pathological phenotypes in a mouse model of CDKL5 disorder. *PLoS One*

Amir RE, Van den Veyver IB, Wan M, Tran CQ, Francke U & Zoghbi HY (1999) Rett syndrome is caused by mutations in X-linked MECP2, encoding methyl-CpG-binding protein 2. *Nat Genet* 23: 185–188

Ariani F, Hayek G, Rondinella D, Artuso R, Mencarelli MA, Spanhol-Rosseto A, Pollazzon M, Buoni S, Spiga O, Ricciardi S, *et al* (2008) FOXG1 Is Responsible for the Congenital Variant of Rett Syndrome. *Am J Hum Genet*

Armstrong D, Dunn JK, Antalffy B & Trivedi R (1995) Selective dendritic alterations in the cortex of rett syndrome. *J Neuropathol Exp Neurol*

Artoni P, Piffer A, Vinci V, LeBlanc J, Nelson CA, Hensch TK & Fagiolini M (2020) Deep learning of spontaneous arousal fluctuations detects early cholinergic defects across neurodevelopmental mouse models and patients. *Proc Natl Acad Sci U S A*

Artuso R, Mencarelli MA, Polli R, Sartori S, Ariani F, Pollazzon M, Marozza A, Cilio MR, Specchio N, Vigevano F, *et al* (2010) Early-onset seizure variant of Rett syndrome: Definition of the clinical diagnostic criteria. *Brain Dev*

Aylward EH, Minshew NJ, Field K, Sparks BF & Singh N (2002) Effects of age on brain volume and head circumference in autism. *Neurology*

Bahi-Buisson N, Nectoux J, Rosas-Vargas H, Milh M, Boddaert N, Girard B, Cances C,

Ville D, Afenjar A, Rio M, *et al* (2008) Key clinical features to identify girls with CDKL5 mutations. *Brain*

Balestra D, Giorgio D, Bizzotto M, Fazzari M, Zeev B Ben, Pinotti M, Landsberger N & Frasca A (2019) Splicing mutations impairing CDKL5 expression and activity can be efficiently rescued by U1snRNA-based therapy. *Int J Mol Sci*

Ballas N, Lioy DT, Grunseich C & Mandel G (2009) Non-cell autonomous influence of MeCP2-deficient glia on neuronal dendritic morphology. *Nat Neurosci*

Barbiero I, De Rosa R & Kilstrup-Nielsen C (2019) Microtubules: A key to understand and correct neuronal defects in CDKL5 deficiency disorder? *Int J Mol Sci*

Barbiero I, Valente D, Chandola C, Magi F, Bergo A, Monteonofrio L, Tramarin M, Fazzari M, Soddu S, Landsberger N, *et al* (2017) CDKL5 localizes at the centrosome and midbody and is required for faithful cell division. *Sci Rep*

Bedogni F, Gigli CC, Pozzi D, Rossi RL, Scaramuzza L, Rossetti G, Pagani M, Kilstrup-Nielsen C, Matteoli M & Landsberger N (2016) Defects during Mecp2 Null Embryonic Cortex Development Precede the Onset of Overt Neurological Symptoms. *Cereb Cortex*

Bedogni F, Rossi RL, Galli F, Cobolli Gigli C, Gandaglia A, Kilstrup-Nielsen C & Landsberger N (2014) Rett syndrome and the urge of novel approaches to study MeCP2 functions and mechanisms of action. *Neurosci Biobehav Rev*

Bellini E, Pavesi G, Barbiero I, Bergo A, Chandola C, Nawaz MS, Rusconi L, Stefanelli G, Strollo M, Valente MM, *et al* (2014) MeCP2 post-translational modifications: a mechanism to control its involvement in synaptic plasticity and homeostasis? *Front Cell Neurosci* 8: 236

Ben-Shachar S, Chahrour M, Thaller C, Shaw CA & Zoghbi HY (2009) Mouse models of MeCP2 disorders share gene expression changes in the cerebellum and hypothalamus. *Hum Mol Genet*

Van Bergen NJ, Massey S, Stait T, Ellery M, Reljić B, Formosa LE, Quigley A, Dottori M, Thorburn D, Stroud DA, *et al* (2021) Abnormalities of mitochondrial dynamics and bioenergetics in neuronal cells from CDKL5 deficiency disorder. *Neurobiol Dis*

Bergo A, Strollo M, Gai M, Barbiero I, Stefanelli G, Sertic S, Gigli CC, Di Cunto F, Kilstrup-Nielsen C & Landsberger N (2015) Methyl-CpG binding protein 2 (MeCP2) localizes at the centrosome and is required for proper mitotic spindle

organization. *J Biol Chem*

Bertani I, Rusconi L, Bolognese F, Forlani G, Conca B, De Monte L, Badaracco G, Landsberger N & Kilstrup-Nielsen C (2006) Functional consequences of mutations in CDKL5, an X-linked gene involved in infantile spasms and mental retardation. *J Biol Chem*

Bodian DL, Schreiber JM, Vilboux T, Khromykh A & Hauser NS (2018) Mutation in an alternative transcript of CDKL5 in a boy with early-onset seizures. *Cold Spring Harb Mol Case Stud*

Brown K, Selfridge J, Lagger S, Connelly J, De Sousa D, Kerr A, Webb S, Guy J, Merusi C, Koerner M V., *et al* (2016) The molecular basis of variable phenotypic severity among common missense mutations causing Rett syndrome. *Hum Mol Genet*

Brown RA & Nunez PL (1983) Electric Fields of the Brain. *Biometrics*

Burtscher J, Zangrandi L, Schwarzer C & Gnaiger E (2015) Differences in mitochondrial function in homogenated samples from healthy and epileptic specific brain tissues revealed by high-resolution respirometry. *Mitochondrion*

Carli S, Chaabane L, Butti C, De Palma C, Aimar P, Salio C, Vignoli A, Giustetto M, Landsberger N & Frasca A (2021) In vivo magnetic resonance spectroscopy in the brain of Cdkl5 null mice reveals a metabolic profile indicative of mitochondrial dysfunctions. *J Neurochem*

Carter JC, Lanham DC, Pham D, Bibat G, Naidu S & Kaufmann WE (2008) Selective cerebral volume reduction in Rett syndrome: A multiple-approach MR imaging study. *Am J Neuroradiol*

Casanova MF, Naidu S, Goldberg TE, Moser HW, Khoromi S, Kumar A, Kleinman JE & Weinberger DR (1991) Quantitative magnetic resonance imaging in Rett syndrome. *J Neuropsychiatry Clin Neurosci*

Castora FJ (2019) Mitochondrial function and abnormalities implicated in the pathogenesis of ASD. *Prog Neuro-Psychopharmacology Biol Psychiatry*

Castrén M, Gaily E, Tengström C, Lähdetie J, Archer H & Ala-Mello S (2011) Epilepsy caused by CDKL5 mutations. *Eur J Paediatr Neurol*

Chahrour M, Sung YJ, Shaw C, Zhou X, Wong STC, Qin J & Zoghbi HY (2008) MeCP2, a key contributor to neurological disease, activates and represses transcription. *Science (80-)*

Chahrour M & Zoghbi HY (2007) The Story of Rett Syndrome: From Clinic to Neurobiology. *Neuron* 56: 422–437

Chao HT, Zoghbi HY & Rosenmund C (2007) MeCP2 Controls Excitatory Synaptic Strength by Regulating Glutamatergic Synapse Number. *Neuron*

Chawla S, Vanhoutte P, Arnold FJL, Huang CLH & Bading H (2003) Neuronal activity-dependent nucleocytoplasmic shuttling of HDAC4 and HDAC5. *J Neurochem*

Chen L, Chen K, Lavery LA, Baker SA, Shaw CA, Li W & Zoghbi HY (2015) MeCP2 binds to non-CG methylated DNA as neurons mature, influencing transcription and the timing of onset for Rett syndrome. *Proc Natl Acad Sci U S A*

Chen Q, Zhu YC, Yu J, Miao S, Zheng J, Xu L, Zhou Y, Li D, Zhang C, Tao J, *et al* (2010) CDKL5, a protein associated with Rett syndrome, regulates neuronal morphogenesis via Rac1 signaling. *J Neurosci*

Chen RZ, Akbarian S, Tudor M & Jaenisch R (2001) Deficiency of methyl-CpG binding protein-2 in CNS neurons results in a Rett-like phenotype in mice. *Nat Genet* 27: 327–331

Chen Y, Wang Y, Modrusan Z, Sheng M & Kaminker JS (2014) Regulation of neuronal gene expression and survival by basal NMDA receptor activity: A role for histone deacetylase 4. *J Neurosci*

Cheng TL, Wang Z, Liao Q, Zhu Y, Zhou WH, Xu W & Qiu Z (2014) MeCP2 Suppresses Nuclear MicroRNA Processing and Dendritic Growth by Regulating the DGCR8/Drosha Complex. *Dev Cell*

Cheval H, Guy J, Merusi C, De Sousa D, Selfridge J & Bird A (2012) Postnatal inactivation reveals enhanced requirement for MeCP2 at distinct age windows. *Hum Mol Genet*

Chida J, Yamane K, Takei T & Kido H (2012) An efficient extraction method for quantitation of adenosine triphosphate in mammalian tissues and cells. *Anal Chim Acta* 727: 8–12

Cohen S, Gabel HW, Hemberg M, Hutchinson AN, Sadacca LA, Ebert DH, Harmin DA, Greenberg RS, Verdine VK, Zhou Z, *et al* (2011) Genome-Wide Activity-Dependent MeCP2 Phosphorylation Regulates Nervous System Development and Function. *Neuron*

Colantuoni C, Jeon OH, Hyder K, Chenchik A, Khimani AH, Narayanan V, Hoffman EP,

Kaufmann WE, Naidu SB & Pevsner J (2001) Gene expression profiling in postmortem Rett Syndrome brain: Differential gene expression and patient classification. *Neurobiol Dis*

Colvert E, Tick B, McEwen F, Stewart C, Curran SR, Woodhouse E, Gillan N, Hallett V, Lietz S, Garnett T, *et al* (2015) Heritability of autism spectrum disorder in a UK population-based twin sample. *JAMA Psychiatry*

Cuddapah VA, Pillai RB, Shekar K V., Lane JB, Motil KJ, Skinner SA, Tarquinio DC, Glaze DG, McGwin G, Kaufmann WE, *et al* (2014) Methyl-CpG-binding protein 2 (MECP2) mutation type is associated with disease severity in rett syndrome. *J Med Genet*

Dash PK, Orsi SA & Moore AN (2006) Spatial memory formation and memory-enhancing effect of glucose involves activation of the tuberous sclerosis complex-mammalian target of rapamycin pathway. *J Neurosci*

Dave A, Shukla F, Wala H & Pillai P (2019) Mitochondrial Electron Transport Chain Complex Dysfunction in MeCP2 Knock-Down Astrocytes: Protective Effects of Quercetin Hydrate. *J Mol Neurosci*

Demarest ST, Olson HE, Moss A, Pestana-Knight E, Zhang X, Parikh S, Swanson LC, Riley KD, Bazin GA, Angione K, *et al* (2019) CDKL5 deficiency disorder: Relationship between genotype, epilepsy, cortical visual impairment, and development. *Epilepsia*

Denic A, Johnson AJ, Bieber AJ, Warrington AE, Rodriguez M & Pirko I (2011) The relevance of animal models in multiple sclerosis research. *Pathophysiology*

DeYoe EA, Bandettini P, Neitz J, Miller D & Winans P (1994) Functional magnetic resonance imaging (FMRI) of the human brain. *J Neurosci Methods*

Drake JC, Wilson RJ, Laker RC, Guan Y, Spaulding HR, Nichenko AS, Shen W, Shang H, Dorn M V., Huang K, *et al* (2021) Mitochondria-localized AMPK responds to local energetics and contributes to exercise and energetic stress-induced mitophagy. *Proc Natl Acad Sci U S A*

Duong TQ (2011) Magnetic resonance imaging of the retina: A brief historical and future perspective. *Saudi J Ophthalmol*

Duong TQ, Silva AC, Lee SP & Kim SG (2000) Functional MRI of calcium-dependent synaptic activity: Cross correlation with CBF and BOLD measurements. *Magn*

Reson Med

Ebert DH, Gabel HW, Robinson ND, Kastan NR, Hu LS, Cohen S, Navarro AJ, Lyst MJ, Ekiert R, Bird AP, *et al* (2013) Activity-dependent phosphorylation of MeCP2 threonine 308 regulates interaction with NCoR. *Nature*

El-Khoury R, Panayotis N, Matagne V, Ghata A, Villard L & Roux JC (2014) GABA and glutamate pathways are spatially and developmentally affected in the brain of Mecp2-deficient mice. *PLoS One*

Elia M, Falco M, Ferri R, Spalletta A, Bottitta M, Calabrese G, Carotenuto M, Musumeci SA, Lo Giudice M & Fichera M (2008) CDKL5 mutations in boys with severe encephalopathy and early-onset intractable epilepsy. *Neurology*

Ellegood J, Henkelman RM & Lerch JP (2012) Neuroanatomical assessment of the integrin β3 mouse model related to autism and the serotonin system using high resolution MRI. *Front Psychiatry*

Ellegood J, Lerch JP & Henkelman RM (2011) Brain abnormalities in a Neuroligin3 R451C knockin mouse model associated with autism. *Autism Res*

Ellegood J, Pacey LK, Hampson DR, Lerch JP & Henkelman RM (2010) Anatomical phenotyping in a mouse model of fragile X syndrome with magnetic resonance imaging. *Neuroimage*

Emerson RW, Adams C, Nishino T, Hazlett HC, Wolff JJ, Zwaigenbaum L, Constantino JN, Shen MD, Swanson MR, Elison JT, *et al* (2017) Functional neuroimaging of high-risk 6-month-old infants predicts a diagnosis of autism at 24 months of age. *Sci Transl Med*

Fehr S, Downs J, Ho G, de Klerk N, Forbes D, Christodoulou J, Williams S & Leonard H (2016) Functional abilities in children and adults with the CDKL5 disorder. *Am J Med Genet Part A*

Fehr S, Leonard H, Ho G, Williams S, De Klerk N, Forbes D, Christodoulou J & Downs J (2015) There is variability in the attainment of developmental milestones in the CDKL5 disorder. *J Neurodev Disord*

Fehr S, Wilson M, Downs J, Williams S, Murgia A, Sartori S, Vecchi M, Ho G, Polli R, Psoni S, *et al* (2013) The CDKL5 disorder is an independent clinical entity associated with early-onset encephalopathy. *Eur J Hum Genet*

Fichou Y, Nectoux J, Bahi-Buisson N, Chelly J & Bienvenu T (2011) An isoform of the

severe encephalopathy-related CDKL5 gene, including a novel exon with extremely high sequence conservation, is specifically expressed in brain. *J Hum Genet*

Foretz M, Guigas B, Bertrand L, Pollak M & Viollet B (2014) Metformin: From mechanisms of action to therapies. *Cell Metab*

Foxe JJ, Burke KM, Andrade GN, Djukic A, Frey HP & Molholm S (2016) Automatic cortical representation of auditory pitch changes in Rett syndrome. *J Neurodev Disord*

Frasca A, Spiombi E, Palmieri M, Albizzati E, Valente MM, Bergo A, Leva B, Kilstrup-Nielsen C, Bianchi F, Di Carlo V, *et al* (2020) MECP2 mutations affect ciliogenesis: a novel perspective for Rett syndrome and related disorders . *EMBO Mol Med*

Frullanti E, Papa FT, Grillo E, Clarke A, Ben-Zeev B, Pineda M, Bahi-Buisson N, Bienvenu T, Armstrong J, Roche Martinez A, *et al* (2019) Analysis of the Phenotypes in the Rett Networked Database. *Int J Genomics*

Fuchs C, Gennaccaro L, Trazzi S, Bastianini S, Bettini S, Martire V Lo, Ren E, Medici G, Zoccoli G, Rimondini R, *et al* (2018) Heterozygous CDKL5 Knockout Female Mice Are a Valuable Animal Model for CDKL5 Disorder. *Neural Plast*

Fuchs C, Rimondini R, Viggiano R, Trazzi S, De Franceschi M, Bartesaghi R & Ciani E (2015) Inhibition of GSK3β rescues hippocampal development and learning in a mouse model of CDKL5 disorder. *Neurobiol Dis*

Fuchs C, Trazzi S, Torricella R, Viggiano R, De Franceschi M, Amendola E, Gross C, Calzà L, Bartesaghi R & Ciani E (2014a) Neurobiology of Disease Loss of CDKL5 impairs survival and dendritic growth of newborn neurons by altering AKT / GSK-3 β signaling. *Neurobiol Dis* 70: 53–68

Fuchs C, Trazzi S, Torricella R, Viggiano R, De Franceschi M, Amendola E, Gross C, Calzà L, Bartesaghi R & Ciani E (2014b) Loss of CDKL5 impairs survival and dendritic growth of newborn neurons by altering AKT/GSK-3β signaling. *Neurobiol Dis*

Fyffe SL, Neul JL, Samaco RC, Chao HT, Ben-Shachar S, Moretti P, McGill BE, Goulding EH, Sullivan E, Tecott LH, *et al* (2008) Deletion of Mecp2 in Sim1-Expressing Neurons Reveals a Critical Role for MeCP2 in Feeding Behavior, Aggression, and the Response to Stress. *Neuron*

Gabel HW, Kinde B, Stroud H, Gilbert CS, Harmin DA, Kastan NR, Hemberg M, Ebert

DH & Greenberg ME (2015) Disruption of DNA-methylation-dependent long gene repression in Rett syndrome. *Nature*

Gandaglia A, Brivio E, Carli S, Palmieri M, Bedogni F, Stefanelli G, Bergo A, Leva B, Cattaneo C, Pizzamiglio L, *et al* (2019) A Novel Mecp2 Y120D Knock-in Model Displays Similar Behavioral Traits But Distinct Molecular Features Compared to the Mecp2-Null Mouse Implying Precision Medicine for the Treatment of Rett Syndrome. *Mol Neurobiol*

Garcia D & Shaw RJ (2017) AMPK: Mechanisms of Cellular Energy Sensing and Restoration of Metabolic Balance. *Mol Cell*

Garofalo EA, Drury I & Goldstein GW (1988) EEG abnormalities aid diagnosis of Rett syndrome. *Pediatr Neurol*

Gemelli T, Berton O, Nelson ED, Perrotti LI, Jaenisch R & Monteggia LM (2006) Postnatal loss of methyl-CpG binding protein 2 in the forebrain is sufficient to mediate behavioral aspects of Rett syndrome in mice. *Biol Psychiatry*

Gennaccaro L, Fuchs C, Loi M, Pizzo R, Alvente S, Berteotti C, Lupori L, Sagona G, Galvani G, Gurgone A, *et al* (2021) Age-related cognitive and motor decline in a mouse model of CDKL5 deficiency disorder is associated with increased neuronal senescence and death. *Aging Dis*

Gigli CC, Scaramuzza L, Gandaglia A, Bellini E, Gabaglio M, Parolaro D, Kilstrup-Nielsen C, Landsberger N & Bedogni F (2016) MeCP2 related studies benefit from the use of CD1 as genetic background. *PLoS One*

Glaze DG (2005) Neurophysiology of Rett syndrome. *J Child Neurol*

Gogliotti RG, Fisher NM, Stansley BJ, Jones CK, Lindsley CW, Conn PJ & Niswender CM (2018) Total RNA sequencing of rett syndrome autopsy samples identifies the M 4 muscarinic receptor as a novel therapeutic target. *J Pharmacol Exp Ther*

Goutieres F & Aicardi J (1986) Atypical forms of Rett syndrome. *Am J Med Genet*

Graser S, Stierhof YD, Lavoie SB, Gassner OS, Lamla S, Le Clech M & Nigg EA (2007) Cep164, a novel centriole appendage protein required for primary cilium formation. *J Cell Biol*

Großer E, Hirt U, Janc OA, Menzfeld C, Fischer M, Kempkes B, Vogelgesang S, Manzke TU, Opitz L, Salinas-Riester G, *et al* (2012) Oxidative burden and mitochondrial dysfunction in a mouse model of Rett syndrome. *Neurobiol Dis*

Grover VPB, Tognarelli JM, Crossey MME, Cox IJ, Taylor-Robinson SD & McPhail MJW (2015) Magnetic Resonance Imaging: Principles and Techniques: Lessons for Clinicians. *J Clin Exp Hepatol*

Gulmez Karaca K, Brito DVC, Zeuch B & Oliveira AMM (2018) Adult hippocampal MeCP2 preserves the genomic responsiveness to learning required for long-term memory formation. *Neurobiol Learn Mem*

Guo JU, Su Y, Shin JH, Shin J, Li H, Xie B, Zhong C, Hu S, Le T, Fan G, *et al* (2014) Distribution, recognition and regulation of non-CpG methylation in the adult mammalian brain. *Nat Neurosci*

Guy J, Gan J, Selfridge J, Cobb S & Bird A (2007) Reversal of neurological defects in a mouse model of Rett syndrome. *Science (80-)*

Guy J, Hendrich B, Holmes M, Martin JE & Bird A (2001) A mouse Mecp2-null mutation causes neurological symptoms that mimic rett syndrome. *Nat Genet*

Ha S, Sohn I-J, Kim N, Sim HJ & Cheon K-A (2015) Characteristics of Brains in Autism Spectrum Disorder: Structure, Function and Connectivity across the Lifespan. *Exp Neurobiol*

Habib SL, Yadav A, Kidane D, Weiss RH & Liang S (2016) Novel protective mechanism of reducing renal cell damage in diabetes: Activation AMPK by AICAR increased NRF2/OGG1 proteins and reduced oxidative DNA damage. *Cell Cycle*

Hagberg B (1995) Clinical delineation of Rett syndrome variants. *Neuropediatrics*

Hagberg B (2005) Rett Syndrome: Long-Term Clinical Follow-Up Experiences Over Four Decades. *J Child Neurol*

Hagberg B, Aicardi J, Dias K & Ramos O (1983) A progressive syndrome of autism, dementia, ataxia, and loss of purposeful hand use in girls: Rett's syndrome: Report of 35 cases. *Ann Neurol*

Hagberg BA & Skjeldal OH (1994) Rett variants: A suggested model for inclusion criteria. *Pediatr Neurol*

Hansen G, Crooks LE, Davis P, De Groot J, Herfkens R, Margulis AR, Gooding C, Kaufman L, Hoenninger J, Arakawa M, *et al* (1980) In vivo imaging of the rat anatomy with nulear magnetic resonance. *Radiology*

Hao S, Tang B, Wu Z, Ure K, Sun Y, Tao H, Gao Y, Patel AJ, Curry DJ, Samaco RC, *et al* (2015) Forniceal deep brain stimulation rescues hippocampal memory in Rett

syndrome mice. *Nature*

Hardan AY, Minshew NJ, Mallikarjuhn M & Keshavan MS (2001) Brain volume in autism. *J Child Neurol*

Hardie DG, Ross FA & Hawley SA (2012) AMPK: A nutrient and energy sensor that maintains energy homeostasis. *Nat Rev Mol Cell Biol*

Harris JJ, Jolivet R & Attwell D (2012) Synaptic Energy Use and Supply. *Neuron*

Hector RD, Dando O, Landsberger N, Kilstrup-Nielsen C, Kind PC, Bailey MES & Cobb SRC (2016) Characterisation of CDKL5 Transcript Isoforms in Human and Mouse. *PLoS One*

Hernandez LM, Rudie JD, Green SA, Bookheimer S & Dapretto M (2015) Neural signatures of autism spectrum disorders: Insights into brain network dynamics. *Neuropsychopharmacology*

Herzig S & Shaw RJ (2018) AMPK: Guardian of metabolism and mitochondrial homeostasis. *Nat Rev Mol Cell Biol*

Hiremath GK & Najm IM (2007) Magnetic resonance spectroscopy in animal models of epilepsy. *Epilepsia*

Hisle-Gorman E, Susi A, Stokes T, Gorman G, Erdie-Lalena C & Nylund CM (2018) Prenatal, perinatal, and neonatal risk factors of autism spectrum disorder. *Pediatr Res*

Hotta N (2019) A new perspective on the biguanide, metformin therapy in type 2 diabetes and lactic acidosis. *J Diabetes Investig*

Howell JJ, Hellberg K, Turner M, Talbott G, Kolar MJ, Ross DS, Hoxhaj G, Saghatelian A, Shaw RJ & Manning BD (2017) Metformin Inhibits Hepatic mTORC1 Signaling via Dose-Dependent Mechanisms Involving AMPK and the TSC Complex. *Cell Metab*

Hoyer C, Gass N, Weber-Fahr W & Sartorius A (2014) Advantages and challenges of small animal magnetic resonance imaging as a translational tool. *Neuropsychobiology*

Hubesch B, Marinier DS, Hetherington HP, Twieg DB & Weiner MW (1989) Clinical mrs studies of the brain. *Invest Radiol*

Hundal RS, Krssak M, Dufour S, Laurent D, Lebon V, Chandramouli V, Inzucchi SE, Schumann WC, Petersen KF, Landau BR, *et al* (2000) Mechanism by which

metformin reduces glucose production in type 2 diabetes. *Diabetes*

Inui K, Akagi M, Ono J, Tsukamoto H, Shimono K, Mano T, Imai K, Yamada M, Muramatsu T, Sakai N, *et al* (2001) Mutational analysis of MECP2 in Japanese patients with atypical Rett syndrome. *Brain Dev* 23: 212–215

Ishii T, Makita Y, Ogawa A, Amamiya S, Yamamoto M, Miyamoto A & Oki J (2001) The role of different X-inactivation pattern on the variable clinical phenotype with Rett syndrome. In *Brain and Development*

Ito H, Mori K, Harada M, Hisaoka S, Toda Y, Mori T, Goji A, Abe Y, Miyazaki M & Kagami S (2017) A Proton Magnetic Resonance Spectroscopic Study in Autism Spectrum Disorder Using a 3-Tesla Clinical Magnetic Resonance Imaging (MRI) System: The Anterior Cingulate Cortex and the Left Cerebellum. *J Child Neurol*

Itoh K, Sakata M, Watanabe M, Aikawa Y & Fujii H (2008) The entry of manganese ions into the brain is accelerated by the activation of N-methyl-d-aspartate receptors. *Neuroscience*

Itoh M, Tahimic CGT, Ide S, Otsuki A, Sasaoka T, Noguchi S, Oshimura M, Goto YI & Kurimasa A (2012) Methyl CpG-binding protein isoform MeCP2-e2 is dispensable for rett syndrome phenotypes but essential for embryo viability and placenta development. *J Biol Chem*

Jadavji NM, Emmerson JT, MacFarlane AJ, Willmore WG & Smith PD (2017) B-vitamin and choline supplementation increases neuroplasticity and recovery after stroke. *Neurobiol Dis*

Jagtap S, Thanos JM, Fu T, Wang J, Lalonde J, Dial TO, Feiglin A, Chen J, Kohane I, Lee JT, *et al* (2019) Aberrant mitochondrial function in patient-derived neural cells from CDKL5 deficiency disorder and Rett syndrome. *Hum Mol Genet*

Jhang CL, Lee HY, Chen JC & Liao W (2020) Dopaminergic loss of cyclin-dependent kinase-like 5 recapitulates methylphenidate-remediable hyperlocomotion in mouse model of CDKL5 deficiency disorder. *Hum Mol Genet*

Jian L, Nagarajan L, de Klerk N, Ravine D, Bower C, Anderson A, Williamson S, Christodoulou J & Leonard H (2006) Predictors of seizure onset in Rett syndrome. *J Pediatr*

Julu POO, Kerr AM, Hansen S, Apartopoulos F & Jamal GA (1997) Functional evidence of brain stem immaturity in Rett syndrome. *Eur Child Adolesc Psychiatry*

Julu POO & Witt Engerström I (2005) Assessment of the maturity-related brainstem functions reveals the heterogeneous phenotypes and facilitates clinical management of Rett syndrome. In *Brain and Development*

Kalscheuer VM, Tao J, Donnelly A, Hollway G, Schwinger E, Kübart S, Menzel C, Hoeltzenbein M, Tommerup N, Eyre H, *et al* (2003) Disruption of the serine/threonine kinase 9 gene causes severe X-linked infantile spasms and mental retardation. *Am J Hum Genet*

Kameshita I, Sekiguchi M, Hamasaki D, Sugiyama Y, Hatano N, Suetake I, Tajima S & Sueyoshi N (2008) Cyclin-dependent kinase-like 5 binds and phosphorylates DNA methyltransferase 1. *Biochem Biophys Res Commun*

Katayama S, Sueyoshi N, Inazu T & Kameshita I (2020) Cyclin-Dependent Kinase-Like 5 (CDKL5): Possible Cellular Signalling Targets and Involvement in CDKL5 Deficiency Disorder. *Neural Plast*

Kaufmann WE, Johnston M V. & Blue ME (2005) MeCP2 expression and function during brain development: Implications for Rett syndrome's pathogenesis and clinical evolution. In *Brain and Development*

Kaufmann WE & Moser HW (2000) Dendritic anomalies in disorders associated with mental retardation. *Cereb Cortex*

Kida H, Takahashi T, Nakamura Y, Kinoshita T, Hara M, Okamoto M, Okayama S, Nakamura K, Kosai KI, Taniwaki T, *et al* (2017) Pathogenesis of Lethal Aspiration Pneumonia in Mecp2-null Mouse Model for Rett Syndrome. *Sci Rep*

Kilstrup-Nielsen C, Rusconi L, La Montanara P, Ciceri D, Bergo A, Bedogni F & Landsberger N (2012) What we know and would like to know about CDKL5 and its involvement in epileptic encephalopathy. *Neural Plast*

Kim MS, Akhtar MW, Adachi M, Mahgoub M, Bassel-Duby R, Kavalali ET, Olson EN & Monteggia LM (2012) An essential role for histone deacetylase 4 in synaptic plasticity and memory formation. *J Neurosci*

Kinde B, Gabel HW, Gilbert CS, Griffith EC & Greenberg ME (2015) Reading the unique DNA methylation landscape of the brain: Non-CpG methylation, hydroxymethylation, and MeCP2. *Proc Natl Acad Sci U S A*

Kishi N & Macklis JD (2004) MECP2 is progressively expressed in post-migratory neurons and is involved in neuronal maturation rather than cell fate decisions. *Mol*

Cell Neurosci

Knudsen GPS, Neilson TCS, Pedersen J, Kerr A, Schwartz M, Hulten M, Bailey MES & Ørstavik KH (2006) Increased skewing of X chromosome inactivation in Rett syndrome patients and their mothers. *Eur J Hum Genet*

Kobayashi Y, Tohyama J, Takahashi Y, Goto T, Haginoya K, Inoue T, Kubota M, Fujita H, Honda R, Ito M, *et al* (2021) Clinical manifestations and epilepsy treatment in Japanese patients with pathogenic CDKL5 variants. *Brain Dev*

Koch S, Mueller S, Foddis M, Bienert T, von Elverfeldt D, Knab F, Farr TD, Bernard R, Dopatka M, Rex A, *et al* (2019) Atlas registration for edema-corrected MRI lesion volume in mouse stroke models. *J Cereb Blood Flow Metab*

Kokura K, Kaul SC, Wadhwa R, Nomura T, Khan MM, Shinagawa T, Yasukawa T, Colmenares C & Ishii S (2001) The Ski Protein Family Is Required for MeCP2-mediated Transcriptional Repression. *J Biol Chem*

Koo B & Hwang P (1996) Localization of focal cortical lesions influences age of onset of infantile spasms. *Epilepsia*

Kriaucionis S & Bird A (2004) The major form of MeCP2 has a novel N-terminus generated by alternative splicing. *Nucleic Acids Res*

Kruusvee V, Lyst MJ, Taylor C, Tarnauskaitė Ž, Bird AP & Cook AG (2017) Structure of the MeCP2–TBLR1 complex reveals a molecular basis for Rett syndrome and related disorders. *Proc Natl Acad Sci* 114: E3243–E3250

Lagger S, Connelly JC, Schweikert G, Webb S, Selfridge J, Ramsahoye BH, Yu M, He C, Sanguinetti G, Sowers LC, *et al* (2017) MeCP2 recognizes cytosine methylated tri-nucleotide and di-nucleotide sequences to tune transcription in the mammalian brain. *PLoS Genet*

Lau JC, Lerch JP, Sled JG, Henkelman RM, Evans AC & Bedell BJ (2008) Longitudinal neuroanatomical changes determined by deformation-based morphometry in a mouse model of Alzheimer's disease. *Neuroimage*

LeBlanc JJ, DeGregorio G, Centofante E, Vogel-Farley VK, Barnes K, Kaufmann WE, Fagiolini M & Nelson CA (2015) Visual evoked potentials detect cortical processing deficits in Rett syndrome. *Ann Neurol*

Lefebvre A, Beggiato A, Bourgeron T & Toro R (2015) Neuroanatomical Diversity of Corpus Callosum and Brain Volume in Autism: Meta-analysis, Analysis of the

Autism Brain Imaging Data Exchange Project, and Simulation. *Biol Psychiatry*

Lenroot RK & Yeung PK (2013) Heterogeneity within autism spectrum disorders: What have we learned from neuroimaging studies? *Front Hum Neurosci*

Lewis JD, Meehan RR, Henzel WJ, Maurer-Fogy I, Jeppesen P, Klein F & Bird A (1992) Purification, sequence, and cellular localization of a novel chromosomal protein that binds to Methylated DNA. *Cell*

Li W, Xu X & Pozzo-Miller L (2016) Excitatory synapses are stronger in the hippocampus of Rett syndrome mice due to altered synaptic trafficking of AMPA-type glutamate receptors. *Proc Natl Acad Sci*

Liang JS, Huang H, Wang JS & Lu JF (2019) Phenotypic manifestations between male and female children with CDKL5 mutations. *Brain Dev*

Liang JS, Shimojima K, Takayama R, Natsume J, Shichiji M, Hirasawa K, Imai K, Okanishi T, Mizuno S, Okumura A, *et al* (2011) CDKL5 alterations lead to early epileptic encephalopathy in both genders. *Epilepsia*

Lilles S, Talvik I, Noormets K, Vaher U, Õunap K, Reimand T, Sander V, Ilves P & Talvik T (2016) CDKL5 gene - Related epileptic encephalopathy in Estonia: Four cases, one novel mutation causing severe phenotype in a boy, and overview of the literature. *Neuropediatrics*

Lin J, Handschin C & Spiegelman BM (2005) Metabolic control through the PGC-1 family of transcription coactivators. *Cell Metab*

Livak KJ & Schmittgen TD (2001) Analysis of relative gene expression data using real-time quantitative PCR and the 2-ΔΔCT method. *Methods* 25: 402–408

Lohret TA, Jensen RE & Kinnally KW (1997) Tim23, a protein import component of the mitochondrial inner membrane, is required for normal activity of the multiple conductance channel, MCC. *J Cell Biol*

Long Q, Huang L, Huang K & Yang Q (2019) Assessing mitochondrial bioenergetics in isolated mitochondria from mouse heart tissues using oroboros 2k-oxygraph. In *Methods in Molecular Biology*

Lu H, Ash RT, He L, Kee SE, Wang W, Yu D, Hao S, Meng X, Ure K, Ito-Ishida A, *et al* (2016) Loss and Gain of MeCP2 Cause Similar Hippocampal Circuit Dysfunction that Is Rescued by Deep Brain Stimulation in a Rett Syndrome Mouse Model. *Neuron*

Ludwig B, Bender E, Arnold S, Hüttemann M, Lee I & Kadenbach B (2001) Cytochrome c oxidase and the regulation of oxidative phosphorylation. *ChemBioChem*

Lupori L, Sagona G, Fuchs C, Mazziotti R, Stefanov A, Putignano E, Napoli D, Strettoi E, Ciani E & Pizzorusso T (2019) Site-specific abnormalities in the visual system of a mouse model of CDKL5 deficiency disorder. *Hum Mol Genet*

Lyst MJ, Ekiert R, Ebert DH, Merusi C, Nowak J, Selfridge J, Guy J, Kastan NR, Robinson ND, De Lima Alves F, *et al* (2013) Rett syndrome mutations abolish the interaction of MeCP2 with the NCoR/SMRT co-repressor. *Nat Neurosci*

Lyst MJ, Ekiert R, Guy J, Selfridge J, Koerner M V., Merusi C, De Sousa D & Bird A (2018) Affinity for DNA Contributes to NLS Independent Nuclear Localization of MeCP2. *Cell Rep*

MacKay CI, Wong K, Demarest ST, Benke TA, Downs J & Leonard H (2021) Exploring genotype-phenotype relationships in the CDKL5 deficiency disorder using an international dataset. *Clin Genet*

MacKay J, Downs J, Wong K, Heyworth J, Epstein A & Leonard H (2017) Autonomic breathing abnormalities in Rett syndrome: Caregiver perspectives in an international database study. *J Neurodev Disord*

Maezawa I & Jin LW (2010) Rett syndrome microglia damage dendrites and synapses by the elevated release of glutamate. *J Neurosci*

Maezawa I, Swanberg S, Harvey D, LaSalle JM & Jin LW (2009) Rett syndrome astrocytes are abnormal and spread MeCP2 deficiency through gap junctions. *J Neurosci*

Magistretti PJ & Allaman I (2015) A Cellular Perspective on Brain Energy Metabolism and Functional Imaging. *Neuron*

Mahajan R & Mostofsky SH (2015) Neuroimaging endophenotypes in autism spectrum disorder. *CNS Spectr*

Mahmood A, Bibat G, Zhan AL, Izbudak I, Farage L, Horska A, Mori S & Naidu S (2010) White matter impairment in rett syndrome: Diffusion tensor imaging study with clinical correlations. *Am J Neuroradiol*

Manning G, Whyte DB, Martinez R, Hunter T & Sudarsanam S (2002) The protein kinase complement of the human genome. *Science (80-)*

Mari F, Azimonti S, Bertani I, Bolognese F, Colombo E, Caselli R, Scala E, Longo I,

Grosso S, Pescucci C, *et al* (2005) CDKL5 belongs to the same molecular pathway of MeCP2 and it is responsible for the early-onset seizure variant of Rett syndrome. *Hum Mol Genet*

Marinangeli C, Didier S, Ahmed T, Caillerez R, Domise M, Laloux C, Bégard S, Carrier S, Colin M, Marchetti P, *et al* (2018) AMP-Activated Protein Kinase Is Essential for the Maintenance of Energy Levels during Synaptic Activation. *iScience*

Martin-Montalvo A, Mercken EM, Mitchell SJ, Palacios HH, Mote PL, Scheibye-Knudsen M, Gomes AP, Ward TM, Minor RK, Blouin MJ, *et al* (2013) Metformin improves healthspan and lifespan in mice. *Nat Commun*

Martínez De Paz A, Khajavi L, Martin H, Claveria-Gimeno R, Tom Dieck S, Cheema MS, Sanchez-Mut J V., Moksa MM, Carles A, Brodie NI, *et al* (2019) MeCP2-E1 isoform is a dynamically expressed, weakly DNA-bound protein with different protein and DNA interactions compared to MeCP2-E2. *Epigenetics and Chromatin*

Maurer S V. & Williams CL (2017) The cholinergic system modulates memory and hippocampal plasticity via its interactions with non-neuronal cells. *Front Immunol*

Mazziotti R, Lupori L, Sagona G, Gennaro M, Della Sala G, Putignano E & Pizzorusso T (2017) Searching for biomarkers of CDKL5 disorder: Early-onset visual impairment in CDKL5 mutant mice. *Hum Mol Genet*

McGraw CM, Samaco RC & Zoghbi HY (2011) Adult neural function requires MeCP2. *Science (80-)*

McKnight TR (2004) Proton magnetic resonance spectroscopic evaluation of brain tumor metabolism. *Semin Oncol*

Meehan RR, Lewis JD, McKay S, Kleiner EL & Bird AP (1989) Identification of a mammalian protein that binds specifically to DNA containing methylated CpGs. *Cell*

Mehrabi S, Sanadgol N, Barati M, Shahbazi A, Vahabzadeh G, Barzroudi M, Seifi M, Gholipourmalekabadi M & Golab F (2018) Evaluation of metformin effects in the chronic phase of spontaneous seizures in pilocarpine model of temporal lobe epilepsy. *Metab Brain Dis*

Melani F, Mei D, Pisano T, Savasta S, Franzoni E, Ferrari AR, Marini C & Guerrini R (2011) CDKL5 gene-related epileptic encephalopathy: Electroclinical findings in the first year of life. *Dev Med Child Neurol*

Mellén M, Ayata P, Dewell S, Kriaucionis S & Heintz N (2012) MeCP2 binds to 5hmC enriched within active genes and accessible chromatin in the nervous system. *Cell*

Menzies KJ & Hood DA (2012) The role of SirT1 in muscle mitochondrial turnover. *Mitochondrion*

Mitsuishi Y, Taguchi K, Kawatani Y, Shibata T, Nukiwa T, Aburatani H, Yamamoto M & Motohashi H (2012) Nrf2 Redirects Glucose and Glutamine into Anabolic Pathways in Metabolic Reprogramming. *Cancer Cell*

Mnatzakanian GN, Lohi H, Munteanu I, Alfred SE, Yamada T, MacLeod PJM, Jones JR, Scherer SW, Schanen NC, Friez MJ, *et al* (2004) A previously unidentified MECP2 open reading frame defines a new protein isoform relevant to Rett syndrome. *Nat Genet*

Mokranjac D & Neupert W (2015) Cell biology: Architecture of a protein entry gate. *Nature*

Montini E, Andolfi G, Caruso A, Buchner G, Walpole SM, Mariani M, Consalez GG, Trump D, Ballabio A & Franco B (1998) Identification and characterization of a novel serine-threonine kinase gene from the Xp22 region. *Genomics*

Moretti P, Levenson JM, Battaglia F, Atkinson R, Teague R, Antalffy B, Armstrong D, Arancio O, Sweatt JD & Zoghbi HY (2006) Learning and memory and synaptic plasticity are impaired in a mouse model of Rett syndrome. *J Neurosci*

Mulcahey PJ, Tang S, Takano H, White A, Davila Portillo DR, Kane OM, Marsh ED, Zhou Z & Coulter DA (2020) Aged heterozygous Cdkl5 mutant mice exhibit spontaneous epileptic spasms. *Exp Neurol*

Muñoz IM, Morgan ME, Peltier J, Weiland F, Gregorczyk M, Brown FC, Macartney T, Toth R, Trost M & Rouse J (2018) Phosphoproteomic screening identifies physiological substrates of the CDKL 5 kinase . *EMBO J*

Murakami JW, Courchesne E, Haas RH, Press GA & Yeung-Courchesne R (1992) Cerebellar and cerebral abnormalities in Rett syndrome: A quantitative MR analysis. *Am J Roentgenol*

Naaijen J, Zwiers MP, Amiri H, Williams SCR, Durston S, Oranje B, Brandeis D, Boecker-Schlier R, Ruf M, Wolf I, *et al* (2017) Fronto-striatal glutamate in autism spectrum disorder and obsessive compulsive disorder. *Neuropsychopharmacology*

Naidu S (1997) Rett syndrome: A disorder affecting early brain growth. *Ann Neurol*

Nan X, Campoy FJ & Bird A (1997) MeCP2 is a transcriptional repressor with abundant binding sites in genomic chromatin. *Cell*

Nan X, Meehan RR & Bird A (1993) Dissection of the methyl-CpG binding domain from the chromosomal protein MeCP2. *Nucleic Acids Res*

Nan X, Tate P, Li E & Bird A (1996) DNA methylation specifies chromosomal localization of MeCP2. *Mol Cell Biol*

Di Nardo A, Rühmkorf A, Award P, Brennecke A, Fagiolini M & Sahin M (2021) Phenotypic characterization of Cdkl5-knockdown neurons establishes elongated cilia as a functional assay for CDKL5 Deficiency Disorder. *Neurosci Res*

Nawaz MS, Giarda E, Bedogni F, Montanara P La, Ricciardi S, Ciceri D, Alberio T, Landsberger N, Rusconi L & Kilstrup-Nielsen C (2016) CDKL5 and shootin1 interact and concur in regulating neuronal polarization. *PLoS One*

Neul JL, Kaufmann WE, Glaze DG, Christodoulou J, Clarke AJ, Bahi-Buisson N, Leonard H, Bailey MES, Schanen NC, Zappella M, *et al* (2010) Rett syndrome: Revised diagnostic criteria and nomenclature. *Ann Neurol*

Newsholme P, Procopio J, Ramos Lima MM, Pithon-Curi TC & Curi R (2003) Glutamine and glutamate - Their central role in cell metabolism and function. *Cell Biochem Funct*

Nguyen CT, Gonzales FA & Jones PA (2001) Altered chromatin structure associated with methylation-induced gene silencing in cancer cells: Correlation of accessibility, methylation, MeCP2 binding and acetylation. *Nucleic Acids Res*

Nguyen MVC, Du F, Felice CA, Shan X, Nigam A, Mandel G, Robinson JK & Ballas N (2012) MeCP2 is critical for maintaining mature neuronal networks and global brain anatomy during late stages of postnatal brain development and in the mature adult brain. *J Neurosci*

Nguyen MVC, Felice CA, Du F, Covey M V., Robinson JK, Mandel G & Ballas N (2013) Oligodendrocyte lineage cells contribute unique features to rett syndrome neuropathology. *J Neurosci*

Niedermeyer E, Rett A & Renner H (1986) Rett syndrome and the electroencephalogram. *Am J Med Genet*

Nomura Y (2005) Early behavior characteristics and sleep disturbance in Rett syndrome. In *Brain and Development*

Oi A, Katayama S, Hatano N, Sugiyama Y, Kameshita I & Sueyoshi N (2017) Subcellular distribution of cyclin-dependent kinase-like 5 (CDKL5) is regulated through phosphorylation by dual specificity tyrosine-phosphorylation-regulated kinase 1A (DYRK1A). *Biochem Biophys Res Commun*

Okabe Y, Takahashi T, Mitsumasu C, Kosai K ichiro, Tanaka E & Matsuishi T (2012) Alterations of gene expression and glutamate clearance in astrocytes derived from an mecp2-null mouse model of rett syndrome. *PLoS One*

Okuda K, Kobayashi S, Fukaya M, Watanabe A, Murakami T, Hagiwara M, Sato T, Ueno H, Ogonuki N, Komano-Inoue S, *et al* (2017) CDKL5 controls postsynaptic localization of GluN2B-containing NMDA receptors in the hippocampus and regulates seizure susceptibility. *Neurobiol Dis*

Okuda K, Takao K, Watanabe A, Miyakawa T, Mizuguchi M & Tanaka T (2018) Comprehensive behavioral analysis of the Cdkl5 knockout mice revealed significant enhancement in anxiety- and fear-related behaviors and impairment in both acquisition and long-term retention of spatial reference memory. *PLoS One*

Olson HE, Costantini JG, Swanson LC, Kaufmann WE, Benke TA, Fulton AB, Hansen R, Poduri A & Heidary G (2021) Cerebral visual impairment in CDKL5 deficiency disorder: vision as an outcome measure. *Dev Med Child Neurol*

Olson HE, Demarest ST, Pestana-Knight EM, Swanson LC, Iqbal S, Lal D, Leonard H, Cross JH, Devinsky O & Benke TA (2019) Cyclin-Dependent Kinase-Like 5 Deficiency Disorder: Clinical Review. *Pediatr Neurol*

Olson HE, Tambunan D, Lacoursiere C, Goldenberg M, Pinsky R, Martin E, Ho E, Khwaja O, Kaufmann WE & Poduri A (2015) Mutations in epilepsy and intellectual disability genes in patients with features of Rett syndrome. *Am J Med Genet Part A*

Paine SML, Munot P, Carmichael J, Das K, Weber MA, Prabhakar P & Jacques TS (2012) The neuropathological consequences of CDKL5 mutation. *Neuropathol Appl Neurobiol*

Pecorelli A, Belmonte G, Meloni I, Cervellati F, Gardi C, Sticozzi C, De Felice C, Signorini C, Cortelazzo A, Leoncini S, *et al* (2015) Alteration of serum lipid profile, SRB1 loss, and impaired Nrf2 activation in CDKL5 disorder. *Free Radic Biol Med*

Pejhan S & Rastegar M (2021) Role of dna methyl-cpg-binding protein mecp2 in rett syndrome pathobiology and mechanism of disease. *Biomolecules*

Peralta S, Pinto M, Arguello T, Garcia S, Diaz F & Moraes CT (2020) Metformin delays neurological symptom onset in a mouse model of neuronal complex I deficiency. *JCI Insight*

Percy AK & Lane JB (2005) Rett syndrome: Model of neurodevelopmental disorders. *J Child Neurol*

Petersen MH, Willert CW, Andersen JV, Waagepetersen HS, Skotte NH & Nørremølle A (2019) Functional Differences between Synaptic Mitochondria from the Striatum and the Cerebral Cortex. *Neuroscience*

Picker JD, Yang R, Ricceri L & Berger-Sweeney J (2006) An altered neonatal behavioral phenotype in Mecp2 mutant mice. *Neuroreport*

Piven J, Bailey J, Ranson BJ & Arndt S (1997) An MRI study of the corpus callosum in autism. *Am J Psychiatry*

Pizzo R, Gurgone A, Castroflorio E, Amendola E, Gross C, Sassoè-Pognetto M & Giustetto M (2016) Lack of Cdkl5 disrupts the organization of excitatory and inhibitory synapses and parvalbumin interneurons in the primary visual cortex. *Front Cell Neurosci*

Provencher SW (2001) Automatic quantitation of localized in vivo 1H spectra with LCModel. *NMR Biomed*

Reiss AL, Faruque F, Naidu S, Abrams M, Beaty T, Bryan RN & Moser H (1993) Neuroanatomy of Rett syndrome: A volumetric imaging study. *Ann Neurol*

Ren E, Roncacé V, Trazzi S, Fuchs C, Medici G, Gennaccaro L, Loi M, Galvani G, Ye K, Rimondini R, *et al* (2019) Functional and structural impairments in the perirhinal cortex of a mouse model of CDKL5 deficiency disorder are rescued by a TrkB agonist. *Front Cell Neurosci*

Renieri A, Mari F, Mencarelli MA, Scala E, Ariani F, Longo I, Meloni I, Cevenini G, Pini G, Hayek G, *et al* (2009) Diagnostic criteria for the Zappella variant of Rett syndrome (the preserved speech variant). *Brain Dev*

Ricciardi S, Boggio EM, Grosso S, Lonetti G, Forlani G, Stefanelli G, Calcagno E, Morello N, Landsberger N, Biffo S, *et al* (2011) Reduced AKT/mTOR signaling and protein synthesis dysregulation in a Rett syndrome animal model. *Hum Mol Genet* 20: 1182–1196

Ricciardi S, Ungaro F, Hambrock M, Rademacher N, Stefanelli G, Brambilla D, Sessa A,

Magagnotti C, Bachi A, Giarda E, *et al* (2012) CDKL5 ensures excitatory synapse stability by reinforcing NGL-1-PSD95 interaction in the postsynaptic compartment and is impaired in patient iPSC-derived neurons. *Nat Cell Biol*

Ronnett G V., Ramamurthy S, Kleman AM, Landree LE & Aja S (2009) AMPK in the brain: Its roles in energy balance and neuroprotection. In *Journal of Neurochemistry*

Roux PP & Blenis J (2004) ERK and p38 MAPK-Activated Protein Kinases: a Family of Protein Kinases with Diverse Biological Functions. *Microbiol Mol Biol Rev*

Rubin R, Abbott LF & Sompolinsky H (2017) Balanced excitation and inhibition are required for high-capacity, noise-robust neuronal selectivity. *Proc Natl Acad Sci U S A*

Rusconi L, Kilstrup-Nielsen C & Landsbergers N (2011) Extrasynaptic N-Methyl-D-aspartate (NMDA) receptor stimulation induces cytoplasmic translocation of the CDKL5 kinase and its proteasomal degradation. *J Biol Chem*

Rusconi L, Salvatoni L, Giudici L, Bertani I, Kilstrup-Nielsen C, Broccoli V & Landsberger N (2008) CDKL5 expression is modulated during neuronal development and its subcellular distribution is tightly regulated by the C-terminal tail. *J Biol Chem*

Saby JN, Benke TA, Peters SU, Standridge SM, Matsuzaki J, Cutri-French C, Swanson LC, Lieberman DN, Key AP, Percy AK, *et al* (2021) Multisite Study of Evoked Potentials in Rett Syndrome. *Ann Neurol*

Sakata K, Kawashima Y, Ichikawa H, Oya T, Takahashi T, Otaki A, Ishikawa S & Morishita Y (1997) University of Wisconsin solution versus modified Collins solution for canine heart preservation: An experimental study. *Int J Angiol*

Samaco RC, Mandel-Brehm C, Chao HT, Ward CS, Fyffe-Maricich SL, Ren J, Hyland K, Thaller C, Maricich SM, Humphreys P, *et al* (2009) Loss of MeCP2 in aminergic neurons causes cell-autonomous defects in neurotransmitter synthesis and specific behavioral abnormalities. *Proc Natl Acad Sci U S A*

Sando R, Gounko N, Pieraut S, Liao L, Yates J & Maximov A (2012) HDAC4 governs a transcriptional program essential for synaptic plasticity and memory. *Cell*

Santos M, Silva-Fernandes A, Oliveira P, Sousa N & Maciel P (2007) Evidence for abnormal early development in a mouse model of Rett syndrome. *Genes, Brain Behav*

Sato C, Sawada K, Wright D, Higashi T & Aoki I (2018) Isotropic 25-micron 3D neuroimaging using ex vivo microstructural manganese-enhanced MRI (MEMRI). *Front Neural Circuits*

Saywell V, Viola A, Confort-Gouny S, Le Fur Y, Villard L & Cozzone PJ (2006) Brain magnetic resonance study of Mecp2 deletion effects on anatomy and metabolism. *Biochem Biophys Res Commun* 340: 776–783

Scala E, Ariani F, Mari F, Caselli R, Pescucci C, Longo I, Meloni I, Giachino D, Bruttini M, Hayek G, *et al* (2005) CDKL5/STK9 is mutated in Rett syndrome variant with infantile spasms. *J Med Genet*

Scaramuzza L, De Rocco G, Desiato G, Cobolli Gigli C, Chiacchiaretta M, Mirabella F, Pozzi D, De Simone M, Conforti P, Pagani M, *et al* (2021) The enhancement of activity rescues the establishment of Mecp2 null neuronal phenotypes . *EMBO Mol Med*

Scarpulla RC (2008) Transcriptional paradigms in mammalian mitochondrial biogenesis and function. *Physiol Rev*

Sceniak MP, Lang M, Enomoto AC, James Howell C, Hermes DJ & Katz DM (2016) Mechanisms of Functional Hypoconnectivity in the Medial Prefrontal Cortex of Mecp2 Null Mice. *Cereb Cortex*

Schroeder E, Yuan L, Seong E, Ligon C, DeKorver N, Gurumurthy CB & Arikkath J (2019) Neuron-Type Specific Loss of CDKL5 Leads to Alterations in mTOR Signaling and Synaptic Markers. *Mol Neurobiol*

Schüle B, Armstrong DD, Vogel H, Oviedo A & Francke U (2008) Severe congenital encephalopathy caused by MECP2 null mutations in males: Central hypoxia and reduced neuronal dendritic structure. *Clin Genet*

Shah RR & Bird AP (2017) MeCP2 mutations: Progress towards understanding and treating Rett syndrome. *Genome Med*

Shahbazian MD, Young JI, Yuva-Paylor LA, Spencer CM, Antalffy BA, Noebels JL, Armstrong DL, Paylor R & Zoghbi HY (2002) Mice with truncated MeCP2 recapitulate many Rett syndrome features and display hyperacetylation of histone H3. *Neuron* 35: 243–254

Shulyakova N, Andreazza AC, Mills LR & Eubanks JH (2017) Mitochondrial dysfunction in the pathogenesis of rett syndrome: Implications for mitochondria-

targeted therapies. *Front Cell Neurosci*

Siddiqui MF, Elwell C & Johnson MH (2016) Mitochondrial Dysfunction in Autism Spectrum Disorders. *Autism Open Access*

Silva AC & Bock NA (2008) Manganese-enhanced MRI: An exceptional tool in translational neuroimaging. *Schizophr Bull*

Silva AC, Lee JH, Aoki I & Koretsky AP (2004) Manganese-enhanced magnetic resonance imaging (MEMRI): Methodological and practical considerations. *NMR Biomed*

Skene PJ, Illingworth RS, Webb S, Kerr ARW, James KD, Turner DJ, Andrews R & Bird AP (2010) Neuronal MeCP2 Is Expressed at Near Histone-Octamer Levels and Globally Alters the Chromatin State. *Mol Cell* 37: 457–468

Sörnmo L & Laguna P (2005) Bioelectrical Signal Processing in Cardiac and Neurological Applications

Squillaro T, Alessio N, Cipollaro M, Melone MAB, Hayek G, Renieri A, Giordano A & Galderisi U (2012) Reduced expression of MECP2 affects cell commitment and maintenance in neurons by triggering senescence: New perspective for Rett syndrome. *Mol Biol Cell*

Stalpers XL, Spruijt L, Yntema HG & Verrips A (2012) Clinical phenotype of 5 females with a CDKL5 mutation. *J Child Neurol*

Stancheva I, Collins AL, Van Den Veyver IB, Zoghbi H & Meehan RR (2003) A mutant form of MeCP2 protein associated with human Rett syndrome cannot be displaced from methylated DNA by Notch in Xenopus embryos. *Mol Cell*

Stefanelli G, Gandaglia A, Costa M, Cheema MS, Di Marino D, Barbiero I, Kilstrup-Nielsen C, Ausió J & Landsberger N (2016) Brain phosphorylation of MeCP2 at serine 164 is developmentally regulated and globally alters its chromatin association. *Sci Rep* 6: 28295

Tang S, Terzic B, Wang ITJ, Sarmiento N, Sizov K, Cui Y, Takano H, Marsh ED, Zhou Z & Coulter DA (2019) Altered NMDAR signaling underlies autistic-like features in mouse models of CDKL5 deficiency disorder. *Nat Commun*

Tang S, Wang ITJ, Yue C, Takano H, Terzic B, Pance K, Lee JY, Cui Y, Coulter DA & Zhou Z (2017a) Loss of CDKL5 in glutamatergic neurons disrupts hippocampal microcircuitry and leads to memory impairment in mice. *J Neurosci*

Tang S, Wang ITJ, Yue C, Takano H, Terzic B, Pance K, Lee JY, Cui Y, Coulter DA & Zhou Z (2017b) Loss of CDKL5 in glutamatergic neurons disrupts hippocampal microcircuitry and leads to memory impairment in mice. *J Neurosci*

Tang Y, Wang ZI, Sarwar S, Choi JY, Wang S, Zhang X, Parikh S, Moosa AN & Pestana-Knight E (2021) Brain morphological abnormalities in children with cyclin-dependent kinase-like 5 deficiency disorder. *Eur J Paediatr Neurol*

Tao J, Hu K, Chang Q, Wu H, Sherman NE, Martinowich K, Klose RJ, Schanen C, Jaenisch R, Wang W, *et al* (2009) Phosphorylation of MeCP2 at serine 80 regulates its chromatin association and neurological function. *Proc Natl Acad Sci U S A*

Terzic B, Felicia Davatolhagh M, Ho Y, Tang S, Liu YT, Xia Z, Cui Y, Fuccillo M V. & Zhou Z (2021) Temporal manipulation of Cdkl5 reveals essential postdevelopmental functions and reversible CDKL5 deficiency disorder-related deficits. *J Clin Invest*

Thatcher KN & LaSalle JM (2006) Dynamic changes in histone H3 lysine 9 acetylation localization patterns during neuronal maturation require Mecp2. *Epigenetics*

Thomas A, Burant A, Bui N, Graham D, Yuva-Paylor LA & Paylor R (2009) Marble burying reflects a repetitive and perseverative behavior more than novelty-induced anxiety. *Psychopharmacology (Berl)*

Tillotson R, Cholewa-Waclaw J, Chhatbar K, Connelly JC, Kirschner SA, Webb S, Koerner M V., Selfridge J, Kelly DA, De Sousa D, *et al* (2021) Neuronal non-CG methylation is an essential target for MeCP2 function. *Mol Cell*

Tramarin M, Rusconi L, Pizzamiglio L, Barbiero I, Peroni D, Scaramuzza L, Guilliams T, Cavalla D, Antonucci F & Kilstrup-Nielsen C (2018) The antidepressant tianeptine reverts synaptic AMPA receptor defects caused by deficiency of CDKL5. *Hum Mol Genet*

Trazzi S, Fuchs C, Viggiano R, de Franceschi M, Valli E, Jedynak P, Hansen FK, Perini G, Rimondini R, Kurz T, *et al* (2016) HDAC4: A key factor underlying brain developmental alterations in CDKL5 disorder. *Hum Mol Genet*

Tudor M, Akbarian S, Chen RZ & Jaenisch R (2002) Transcriptional profiling of a mouse model for Rett syndrome reveals subtle transcriptional changes in the brain. *Proc Natl Acad Sci U S A*

Ure K, Lu H, Wang W, Ito-Ishida A, Wu Z, He LJ, Sztainberg Y, Chen W, Tang J & Zoghbi HY (2016) Restoration of Mecp2 expression in GABAergic neurons is

sufficient to rescue multiple disease features in a mouse model of Rett syndrome. *Elife*

Vaccarino FM & Smith KM (2009) Increased Brain Size in Autism-What It Will Take to Solve a Mystery. *Biol Psychiatry*

Vagnozzi R, Tavazzi B, Signoretti S, Amorini AM, Belli A, Cimatti M, Delfini R, Di Pietro V, Finocchiaro A & Lazzarino G (2007) Temporal window of metabolic brain vulnerability to concussions: Mitochondrial-related impairment - Part I. *Neurosurgery*

Valli E, Trazzi S, Fuchs C, Erriquez D, Bartesaghi R, Perini G & Ciani E (2012) CDKL5, a novel MYCN-repressed gene, blocks cell cycle and promotes differentiation of neuronal cells. *Biochim Biophys Acta - Gene Regul Mech*

Vashi N & Justice MJ (2019) Treating Rett syndrome: from mouse models to human therapies. *Mamm Genome*

Vial G, Detaille D & Guigas B (2019) Role of mitochondria in the mechanism(s) of action of metformin. *Front Endocrinol (Lausanne)*

Vigli D, Rusconi L, Valenti D, La Montanara P, Cosentino L, Lacivita E, Leopoldo M, Amendola E, Gross C, Landsberger N, *et al* (2019) Rescue of prepulse inhibition deficit and brain mitochondrial dysfunction by pharmacological stimulation of the central serotonin receptor 7 in a mouse model of CDKL5 Deficiency Disorder. *Neuropharmacology*

Viola A, Saywell V, Villard L, Cozzone PJ & Lutz NW (2007) Metabolic fingerprints of altered brain growth, osmoregulation and neurotransmission in a Rett syndrome model. *PLoS One* 2

Viscomi C, Bottani E, Civiletto G, Cerutti R, Moggio M, Fagiolari G, Schon EA, Lamperti C & Zeviani M (2011) In vivo correction of COX deficiency by activation of the AMPK/PGC-1α axis. *Cell Metab*

Wallace DC (2005) A mitochondrial paradigm of metabolic and degenerative diseases, aging, and cancer: A dawn for evolutionary medicine. *Annu Rev Genet*

Wallimann T, Wyss M, Brdiczka D, Nicolay K & Eppenberger HM (1992) Intracellular compartmentation, structure and function of creatine kinase isoenzymes in tissues with high and fluctuating energy demands: The 'phosphocreatine circuit' for cellular energy homeostasis. *Biochem J*

Wang ITJ, Allen M, Goffin D, Zhu X, Fairless AH, Brodkin ES, Siegel SJ, Marsh ED, Blendy JA & Zhou Z (2012a) Loss of CDKL5 disrupts kinome profile and event-related potentials leading to autistic-like phenotypes in mice. *Proc Natl Acad Sci U S A*

Wang ITJ, Allen M, Goffin D, Zhu X, Fairless AH, Brodkin ES, Siegel SJ, Marsh ED, Blendy JA & Zhou Z (2012b) Loss of CDKL5 disrupts kinome profile and event-related potentials leading to autistic-like phenotypes in mice. *Proc Natl Acad Sci U S A*

Ward BC, Agarwal S, Wang K, Berger-Sweeney J & Kolodny NH (2008) Longitudinal brain MRI study in a mouse model of Rett Syndrome and the effects of choline. *Neurobiol Dis*

Weng SM, Bailey MES & Cobb SR (2011) Rett syndrome: From bed to bench. *Pediatr Neonatol*

Williamson SL, Giudici L, Kilstrup-Nielsen C, Gold W, Pelka GJ, Tam PPL, Grimm A, Prodi D, Landsberger N & Christodoulou J (2012) A novel transcript of cyclin-dependent kinase-like 5 (CDKL5) has an alternative C-terminus and is the predominant transcript in brain. *Hum Genet*

Wyss M & Kaddurah-Daouk R (2000) Creatine and creatinine metabolism. *Physiol Rev*

Xia J & Wishart DS (2011) Web-based inference of biological patterns, functions and pathways from metabolomic data using MetaboAnalyst. *Nat Protoc*

Xie R, Nguyen S, McKeehan K, Wang F, McKeehan WL & Liu L (2011) Microtubule-associated protein 1S (MAP1S) bridges autophagic components with microtubules and mitochondria to affect autophagosomal biogenesis and degradation. *J Biol Chem*

Yamamoto T, Shimojima K, Kimura N, Mogami Y, Usui D, Takayama R, Ikeda H & Imai K (2015) Recurrent occurrences of CDKL5 mutations in patients with epileptic encephalopathy. *Hum Genome Var*

Yan Y, He D, Wu J, Hou R, Sun K & Li L (2020) Novel CDKL5 mutations were found in patients in China: Retrospective investigation in cases of CDKL5-related disorders. *Ital J Pediatr*

Yennawar M, White RS & Jensen FE (2019) AMPA receptor dysregulation and therapeutic interventions in a mouse model of CDKL5 deficiency disorder. *J Neurosci*

Young JI, Hong EP, Castle JC, Crespo-Barreto J, Bowman AB, Rose MF, Kang D, Richman R, Johnson JM, Berget S, *et al* (2005) Regulation of RNA splicing by the methylation-dependent transcriptional repressor methyl-CpG binding protein 2. *Proc Natl Acad Sci U S A*

Yuen N, Szulc-Lerch KU, Li YQ, Morshead CM, Mabbott DJ, Wong CS & Nieman BJ (2021) Metformin effects on brain development following cranial irradiation in a mouse model. *Neuro Oncol*

Zerbi V, Pagani M, Markicevic M, Matteoli M, Pozzi D, Fagiolini M, Bozzi Y, Galbusera A, Scattoni ML, Provenzano G, *et al* (2021) Brain mapping across 16 autism mouse models reveals a spectrum of functional connectivity subtypes. *Mol Psychiatry*

Zhang J, Peng Q, Li Q, Jahanshad N, Hou Z, Jiang M, Masuda N, Langbehn DR, Miller MI, Mori S, *et al* (2010) Longitudinal characterization of brain atrophy of a Huntington's disease mouse model by automated morphological analyses of magnetic resonance images. *Neuroimage*

Zhao H, Li T, Wang K, Zhao F, Chen J, Xu G, Zhao J, Li T, Chen L, Li L, *et al* (2019) AMPK-mediated activation of MCU stimulates mitochondrial Ca2+ entry to promote mitotic progression. *Nat Cell Biol*

Zhou W, Kavelaars A & Heijnen CJ (2016) Metformin prevents cisplatin-induced cognitive impairment and brain damage in mice. *PLoS One*

Zhou Z, Hong EJ, Cohen S, Zhao W ning, Ho H yi H, Schmidt L, Chen WG, Lin Y, Savner E, Griffith EC, *et al* (2006) Brain-Specific Phosphorylation of MeCP2 Regulates Activity-Dependent Bdnf Transcription, Dendritic Growth, and Spine Maturation. *Neuron*

Zhu YC, Li D, Wang L, Lu B, Zheng J, Zhao SL, Zeng R & Xiong ZQ (2013) Palmitoylation-dependent CDKL5-PSD-95 interaction regulates synaptic targeting of CDKL5 and dendritic spine development. *Proc Natl Acad Sci U S A*

Zuliani I, Urbinati C, Valenti D, Quattrini MC, Medici V, Cosentino L, Pietraforte D, Di Domenico F, Perluigi M, Vacca RA, *et al* (2020) The anti-diabetic drug metformin rescues aberrant mitochondrial activity and restrains oxidative stress in a female mouse model of rett syndrome. *J Clin Med*